REPORT DOCUMENTATION PAGE

Form Approved
OMB NO. 0704-0188

Public reporting burden for this collection of information is estimated to average 1 hour per response, including the time for reviewing instructions, searching existing data sources, gathering and maintaining the data needed, and completing and reviewing the collection of information. Send comment regarding this burden estimates or any other aspect of this collection of information, including suggestions for reducing this burden, to Washington Headquarters Services, Directorate for information Operations and Reports, 1215 Jefferson Davis Highway, Suite 1204, Arlington, VA 22202-4302, and to the Office of Management and Budget, Paperwork Reduction Project (0704-0188), Washington, DC 20503.

1. AGENCY USE ONLY *(Leave blank)*

2. REPORT DATE
December 3, 1996

3. REPORT TYPE AND DATES COVERED
Technical (8/93 - 5/96)

4. TITLE AND SUBTITLE
Numerical Study of Shear-Induced Heating in High-Speed Nozzle Flow

5. FUNDING NUMBERS
DAA04-93-G-0413

6. AUTHOR(S)
Xiyan Shi (Omar M. Knio, Joseph Katz)

7. PERFORMING ORGANIZATION NAMES(S) AND ADDRESS(ES)
Department of Mechanical Engineering
The Johns Hopkins University
Baltimore, MD 21218-2686

8. PERFORMING ORGANIZATION REPORT NUMBER
JHU-ME-CF1

9. SPONSORING / MONITORING AGENCY NAME(S) AND ADDRESS(ES)
U.S. Army Research Office
P.O. Box 12211
Research Triangle Park, NC 27709-2211

10. SPONSORING / MONITORING AGENCY REPORT NUMBER
ARO 31990.2-EL

11. SUPPLEMENTARY NOTES
The views, opinions and/or findings contained in this report are those of the author(s) and should not be construed as an official Department of the Army position, policy or decision, unless so designated by other documentation.

12a. DISTRIBUTION / AVAILABILITY STATEMENT
Approved for public release; distribution unlimited.

12 b. DISTRIBUTION CODE

13. ABSTRACT *(Maximum 200 words)*

During high-speed injection in small-diameter nozzles, a combustible mixture may experience high enough temperature for premature ignition to occur. Among the various physical mechanisms which may lead to such an undesirable effect, shear-induced heating is believed to play an important role. In this effort, the impact of shear heating is analyzed theoretically and numerically. The first part of the study focuses on short-duration events, for which shear heating remains confined to thin laminar boundary layers. This situation is analyzed using computational codes which numerically integrate the parabolized vorticity transport and energy equations. The codes are applied to predict the peak temperatures, and to analyze the effects of injection speed, inlet mixture temperature, and variable mixture properties . The second part of the study considers continuous injection modes. In these situations, boundary layer transition is expected to occur, and one must characterize the mean flow and temperature field, and fluctuations around the mean. To this end, the mean temperature solutions are constructed using well-established empirical correlations for the mean velocity field. Meanwhile, the impact of temperature fluctuations is evaluated in light of direct simulation of isotropic turbulence and transitional channel flow.

14. SUBJECT TERMS
shear heating; liquid monopropellant

15. NUMBER IF PAGES
xxiii+183

16. PRICE CODE

17. SECURITY CLASSIFICATION OR REPORT
UNCLASSIFIED

18. SECURITY CLASSIFICATION OF THIS PAGE
UNCLASSIFIED

19. SECURITY CLASSIFICATION OF ABSTRACT
UNCLASSIFIED

20. LIMITATION OF ABSTRACT
UL

NSN 7540-01-280-5500

DTIC QUALITY INSPECTED 3

Standard Form 298 (Rev. 2-89)
Prescribed by ANSI Std. 239-18
298-102

Numerical Study of Shear-Induced Heating in High-Speed Nozzle Flow

Xiyan Shi

An essay submitted to The Johns Hopkins University
in conformity with the requirements for the degree
Doctor of Philosophy
in
Mechanical Engineering

Baltimore, Maryland
1996

19970212 068

ABSTRACT

During high-speed injection in small-diameter nozzles, a combustible mixture may experience high enough temperature for premature ignition to occur. Among the various physical mechanisms which may lead to such an undesirable effect, shear-induced heating is believed to play an important role. The objective of this effort is to study, theoretically and numerically, the impact of shear-induced heating on the likelihood of mixture ignition.

The manisfestation of shear-induced heating effects is believed to be considerably dependent on the mode of injection. For the purpose of this study, two injection modes (short-duration injection and continuous injection) are distinguished. For short duration injection, shear-induced heating is expected to be confined to thin laminar boundary layers. This situation is analyzed using computational codes which implement simplified physical models for high-speed injection in a constant-diameter nozzle. The computational codes, which numerically integrate the incompressible vorticity transport and energy equations, are applied to predict the maximum temperatures experienced by the mixture. The impact of injection speed and inlet mixture temperature, and the effect of variable mixture properties were also investigated. For continuous injection, boundary layer transition is expected to occur. In order to characterize the shear heating mechanisms within a transitional or turbulent flow environment, one must characterize the mean flow and temperature field, and fluctuations around the mean. To this end, the mean temperature solutions are constructed using well-established empirical correlations for the mean velocity field. Meanwhile, the impact of temperature fluctuations is evaluated in light of direct simulation of isotropic turbulence and transitional channel flow.

Dedicated to my parents

Acknowledgments

I express my greatest appreciation to my advisor, Dr. O. M. Knio, for his help, guidance, and support throughout this work. His enthusiasm in scientific research and rigorous scholarship has inspired me to become a better researcher. Without his constant encouragement, endless discussions, instructions and constructive comments, I would not have completed this thesis.

I would like to express my gratitude to my dissertation committee, Dr. J. Katz, and Dr. C. Meneveau, for their precious time, efforts and comments.

Also, I would like to acknowledge my fellow graduate students, who have contributed this work through discussions and comments.

Finally, I would like to express my deepest gratitude to my husband, Feng Huang, for the never-ending support, encouragement, and patience he provided over the course of this work.

This work is supported by the Army Research Office under Grant DAAH-93-G-0413. The computer codes are run on CRAY supercomputer.

Contents

Abstract ii

Acknowledgements v

Table of Contents vii

List of Figures xi

1 Introduction 1

I Numerical Study of Laminar Flow 8

2 Numerical approach 9

2.1 General 9

2.2 Formulation 11

2.3 Normalization 14

3 Impulsively-Started Quasi-1d Flow 17

3.1 Solutions of the Energy Equation 19

3.2 Discussion 22

4 Axisymmetric Flow **27**

4.1 Inflow and Initial Conditions 29

4.2 Direct Numerical Simulation 30

4.2.1 Results and Discussion 34

4.3 Parabolized Approximations 40

4.4 Results and Discussion 41

4.4.1 Validity of the parabolized approximation 41

4.4.2 Further Analysis of Modeling approximation 43

4.4.3 Shear Heating of LP 1846 during High-Speed Injection 49

4.4.4 Effect of Wall Heat Transfer 54

5 Variable Mixture Properties **65**

5.1 Formulation 66

5.2 Modeling Strategies 67

5.3 Application of LP-1846 69

5.3.1 Effect of Wall Heat Transfer 71

5.3.2 Effect of injection temperature 72

6 Summary and Conclusions **85**

II Direct Numerical Simulation of Turbulent Flow 89

7 1D Solution of Turbulent Flow between Parallel Plates 90

7.1 The Mean Temperature Distribution 90

7.2 Results and Discussion 96

8 Homogeneous Isotropic Turbulence 102

8.1 Introduction 102

8.2 Formulation 103

8.3 Numerical Schemes 105

8.4 Forcing 112

8.5 Initial Conditions 113

8.6 Results and Discussion 115

9 Turbulent Channel Flow 127

9.1 Introduction 127

9.2 Formulation 127

9.3 Normalization 129

9.4 Numerical Scheme 130

9.5 Initial Conditions 140

9.6 Results and Discussion 141

A 161

A.1 Parabolized Approximation for a Constant Property Mixture . 161

A.2 Stretched Coordinates 162
A.3 Unsteady Simulation 163
A.4 Steady Code 166

B **169**

B.1 Parabolized Approximation for a Variable Property Mixture . 170
B.2 Stretched Coordinates 171
B.3 Unsteady Simulation 171
B.4 Steady Code 176

Bibliography **179**

List of Figures

3.1 Normalized temperature profiles, plotted against the similarity coordinate η, for different Eckert numbers and Prandtl numbers. The value of the Eckert number is indicated. 24

3.2 Normalized temperature profiles, plotted against the similarity coordinate η, for different injection speeds and Prandtl numbers. The value of injection velocity is indicated. 25

3.3 Heating of a mixture impulsively accelerated over a flat plate. The mixture is assumed to have the same heat capacity as water and an initial temperature of $295^o K$. Temperature profiles are plotted against the similarity coordinate η, for different injection speeds and Prandtl numbers. The value of injection velocity is indicated. 26

4.1 Laminar boundary development in an axisymmetric nozzle. Water is injected at $20 m/s$; the nozzle is $20 mm$ long and has $2 mm$ inner radius. The plots show normalized streamwise velocity profiles at different times following injection. In each gragh, profiles at different downstream locations are plotted. 37

4.2 Laminar boundary layer development in an axisymmetric nozzle. Water is injected at $20 m/s$; the nozzle is $20 mm$ long and $2 mm$ inner radius. The plots show normalized streamwise velocity profiles at different streamwise locations. In each gragh, profiles at different times following injection are plotted. . . . 38

4.3 Thermal boundary layer development in an axisymmetric nozzle. Water is injected at $20 m/s$; the nozzle is $20 mm$ long and has $2 mm$ inner radius. The plots show normalized temperature profiles at different streamwise locations. In each graph, profiles at different times following injection are plotted. . . . 39

4.4 Streamwise velocity profiles for the same injection parameters of Fig. 4.1, computed using steady parabolized simulations. The streamwise location is indicated. 44

4.5 Streamwise velocity profiles at $z = 19.925 mm$ for the same injection parameters of Fig. 4.2, computed using steady paravolized simulations, and the unsteady direct simulation at $t = 10 ms$. 45

4.6 Wall temperature distributions during high-speed injection of kerosine with $U = 365 m/s$ and $T_o = 293^o K$. The computations are performed using the steady parabolized approximation on a stretched grid woth $N_r = 401$ points in the radial direction and $N_z = 8001$ points in the streamwise direction. The grid stretching parameter $a = 6.5$, amd a flat inlet temperature profile is imposed. The inlet momentum boundary layer thickness δ_{in} is indicated. 50

4.7 Instantaneous wall temperature distributions during high-speed injection of kerosine with $U = 365 m/s$ and $T_o = 293^o K$. The computations are performed using the unsteady parabolized approximation on a stretched grid with a stretching parameter $a = 6.5$, $N_r = 401$ points in the radial direction and $N_z = 8001$ points in the streamwise direction. A flat inlet temperature profile is imposed, while the inlet viscous layer has $\delta_{in} = 1.29 \mu m$. 51

4.8 Steady state wall temperature distributions for high-speed injection of kerosine with $U = 365m/s$ and $T_o = 293^oK$. The computations are performed using the steady parabolized approximation on a stretched grid with a stretching parameter $a = 6.5$, $N_r = 401$ points in the radial direction and $N_z = 8001$ points in the streamwise direction. The inlet viscous layer has $\delta_{in} = 1.29\mu m$. Results are shown for both flat (dashed line) and non-uniform (solid line) profiles. In the latter case, the inlet temperature profile is adapted from the analysis of section 3. 52

4.9 Steady state wall temperature distributions for high-speed injection of LP 1846 with $T_o = 298^oK$ at four different velocities, $U = 100m/s$, $U = 200m/s$, $U = 300m/s$, and $U = 400m/s$. The computations are performed using the steady parabolized approximation on a stretched grid with a stretching parameter $a = 6.5$, $N_r = 401$ points in the radial direction and $N_z = 8001$ points in the streamwise direction. 58

4.10 Instantaneous wall temperature distribution for high-speed injection of LP 1846 with $T_o = 298^o K$ and $U = 300 m/s$. The computations are performed using the unsteady parabolized approximation on a stretched grid with a stretching parameter $a = 6$, $N_r = 201$ points in the radial direction and $N_z = 801$ points in the streamwise direction. The integration time step $\Delta t = 4 \times 10^{-4}$. 59

4.11 Steady state peak temperature distributions for high-speed injection of LP 1648 with $T_o = 298^o K$, $U = 100 m/s$, and four different Nusselt number $Nu = 0$, $Nu = 0.267$, $Nu = 1.33$, and $Nu = 6.67$. The computations are performed using the steady parabolized approximation on a stretched grid with a stretching parameter $a = 6.5$, $N_r = 401$ points in the radial direction and $N_z = 8001$ points in the streamwise direction. . . 60

4.12 Steady state peak temperature distributions for high-speed injection of LP 1648 with $T_o = 298^o K$, $U = 200 m/s$, and four different Nusselt number $Nu = 0$, $Nu = 0.267$, $Nu = 1.33$, and $Nu = 6.67$. The computations are performed using the steady parabolized approximation on a stretched grid with a stretching parameter $a = 6.5$, $N_r = 401$ points in the radial direction and $N_z = 8001$ points in the streamwise direction. . . 61

4.13 Steady state peak temperature distributions for high-speed injection of LP 1648 with $T_o = 298^oK$, $U = 300m/s$, and four different Nusselt number $Nu = 0$, $Nu = 0.267$, $Nu = 1.33$, and $Nu = 6.67$. The computations are performed using the steady parabolized approximation on a stretched grid with a stretching parameter $a = 6.5$, $N_r = 401$ points in the radial direction and $N_z = 8001$ points in the streamwise direction. . . 62

4.14 Steady state radial temperature profile at the nozzle exit for high-speed injection of LP 1648 with $T_o = 298^oK$, $U = 100m/s$, and four different Nusselt number $Nu = 0$, $Nu = 0.267$, $Nu = 1.33$, and $Nu = 6.67$. The computations are performed using the steady parabolized approximation on a stretched grid with a stretching parameter $a = 6.5$, $N_r = 401$ points in the radial direction and $N_z = 8001$ points in the streamwise direction. 63

4.15 Steady state radial temperature profile at the nozzle exit for high-speed injection of LP 1648 with $T_o = 298^oK$, $U = 300m/s$, and four different Nusselt number $Nu = 0$, $Nu = 0.267$, $Nu = 1.33$, and $Nu = 6.67$. The computations are performed using the steady parabolized approximation on a stretched grid with a stretching parameter $a = 6.5$, $N_r = 401$ points in the radial direction and $N_z = 8001$ points in the streamwise direction. 64

5.1 Steady state wall temperature distribution for high-speed injection of LP 1648 with $T_o = 298^oK$ at four difference velocities, $U = 100m/s$, $U = 200m/s$, $U = 300m/s$, and $U = 400m/s$. The uniform Peclet number model is adopted, and the computations are performed using the steady parabolized approximation on a stretched grid with a stretching parameter $a = 6.5$, $N_r = 401$ points in the radial direction and $N_z = 8001$ points in the streamwise direction. 75

5.2 Steady state wall temperature distribution for high-speed injection of LP 1648 with $T_o = 298^oK$ at four difference velocities, $U = 100m/s$, $U = 200m/s$, $U = 300m/s$, and $U = 400m/s$. The uniform Prandtl number model is adopted, and the computations are performed using the steady parabolized approximation on a stretched grid with a stretching parameter $a = 6.5$, $N_r = 401$ points in the radial direction and $N_z = 8001$ points in the streamwise direction. 76

5.3 Steady state peak temperature distribution for high-speed injection of LP 1648 with $T_o = 298^oK$, $U = 100m/s$, and four different Nusselt number $Nu = 0$, $Nu = 0.267$, $Nu = 1.33$, and $Nu = 6.67$. The uniform Peclet number model is adopted, and the computations are performed using the steady parabolized approximation on a stretched grid with a stretching parameter $a = 6.5$, $N_r = 401$ points in the radial direction and $N_z = 8001$ points in the streamwise direction. 77

5.4 Steady state peak temperature distribution for high-speed injection of LP 1648 with $T_o = 298^oK$, $U = 200m/s$, and four different Nusselt number $Nu = 0$, $Nu = 0.267$, $Nu = 1.33$, and $Nu = 6.67$. The uniform Peclet number model is adopted, and the computations are performed using the steady parabolized approximation on a stretched grid with a stretching parameter $a = 6.5$, $N_r = 401$ points in the radial direction and $N_z = 8001$ points in the streamwise direction. 78

5.5 Steady state peak temperature distribution for high-speed injection of LP 1648 with $T_o = 298^oK$, $U = 300m/s$, and four different Nusselt number $Nu = 0$, $Nu = 0.267$, $Nu = 1.33$, and $Nu = 6.67$. The uniform Peclet number model is adopted, and the computations are performed using the steady parabolized approximation on a stretched grid with a stretching parameter $a = 6.5$, $N_r = 401$ points in the radial direction and $N_z = 8001$ points in the streamwise direction. 79

5.6 Steady state peak temperature distribution for high-speed injection of LP 1648 with $U = 100m/s$, and three different inlet temperatures $T_o = 278^oK$, $T_o = 298^oK$, and $T_o = 318^oK$. The uniform Peclet number model is adopted, and the computations are performed using the steady parabolized approximation on a stretched grid with a stretching parameter $a = 6.5$, $N_r = 401$ points in the radial direction and $N_z = 8001$ points in the streamwise direction. 80

5.7 Steady state peak temperature distribution for high-speed injection of LP 1648 with $U = 200m/s$, and three different inlet temperatures $T_o = 278^oK$, $T_o = 298^oK$, and $T_o = 318^oK$. The uniform Peclet number model is adopted, and the computations are performed using the steady parabolized approximation on a stretched grid with a stretching parameter $a = 6.5$, $N_r = 401$ points in the radial direction and $N_z = 8001$ points in the streamwise direction. 81

5.8 Steady state peak temperature distribution for high-speed injection of LP 1648 with $U = 300m/s$, and three different inlet temperatures $T_o = 278^oK$, $T_o = 298^oK$, and $T_o = 318^oK$. The uniform Peclet number model is adopted, and the computations are performed using the steady parabolized approximation on a stretched grid with a stretching parameter $a = 6.5$, $N_r = 401$ points in the radial direction and $N_z = 8001$ points in the streamwise direction. 82

5.9 Steady state streamwise velocity profiles at different streamwise locations for high-speed injection of LP 1846 with $U = 300m/s$, and two different inlet temperature $T_o = 278^o K$(dashed line), and $T_o = 298^o K$ (solid line). The uniform Peclet number model is adopted, and the computations are performed using the steady parabolized approximation on a stretched grid with a stretching parameter $a = 6.5$, $N_r = 401$ points in the radial direction and $N_z = 8001$ points in the streamwise direction. . . 83

5.10 Steady state temperature profiles at different streamwise locations for high-speed injection of LP 1846 with $U = 300m/s$, and two different inlet temperature $T_o = 278^o K$(dashed line), and $T_o = 298^o K$ (solid line). The uniform Peclet number model is adopted, and the computations are performed using the steady parabolized approximation on a stretched grid with a stretching parameter $a = 6.5$, $N_r = 401$ points in the radial direction and $N_z = 8001$ points in the streamwise direction. . . 84

7.1 Turbulent mean velocity distribution in wall coordinates. The calculation is performed with maximum mean velocity $\overline{u}_{max} = 300m/s$, half channel depth $h = 2mm$, viscosity $\nu = 5.0e^{-6}$. . . 98

7.2 Comparison of turbulent and laminar parabolic profiles for the same mean velocity. The velocities are normalized with the maximum turbulent velocity at the center line. The turbulent velocity profile is computed with maximum mean velocity $\overline{u}_{max} = 300m/s$, half channel depth $h = 2mm$, viscosity $\nu = 5.e^{-6}$. 99

7.3 Turbulent mean temperature profile with four different Prandtl numbers, 7, 25, 64 and 100 in wall coordinates and constant wall temperature condition. The calculations are performed with maximum mean velocity $\overline{u}_{max} = 300m/s$, half channel depth $h = 2mm$, and viscosity $\nu = 5.e^{-6}$. 100

7.4 Dimensional turbulent mean temperature profile (maximum mean velocity $\overline{u}_{max} = 300m/s$) and laminar entrance temperature profile (maximum velocity is $300m/s$) with $Pr = 109$, half channel depth $h = 2mm$, and viscosity $\nu = 5.e^{-6}$. Also, constant wall temperature condition is imposed at both cases. 101

8.1 The variation of the viscous dissipation rate. 118

8.2 The variation of the root-mean=square velocity of turbulent flow. 119

8.3 The evolution of the energy spectrum for case 1. 120

8.4 The evolution of the energy spectrum for case 2. 121

8.5 The evolution of the energy spectrum for case 3. 122

8.6 Temperature spectrum for case 1. 123

8.7 Temperature spectrum for case 2. 124

8.8 Temperature spectrum for case 3. 125

8.9 The evolution of the maximum and mean temperature. 126

9.1 The initial undisturbed streamwise velocity profile. 146

9.2 The initial cross-stream temperature profile with $Pr = 7$. . . 147

9.3 The evolution of the mean streamwise velocity u_x. 148

9.4 The evolution of the mean spanwise vorticity ω_y. 149

9.5 The mean temperature evolution. 150

9.6 The evolution of root mean-square streamwise velocity. 151

9.7 The evolution of root mean-square spanwise velocity. 152

9.8 The evolution of root mean-square cross-stream velocity. . . . 153

9.9 The evolution of root-mean-square streamwise vorticity. 154

9.10 The evolution of root-mean-square spanwise vorticity. 155

9.11 The evolution of root-mean-square cross-stream vorticity. . . . 156

9.12 The contour plot of temperature distribution in y-z plane($x = 2\pi d$) at $t = 2.05\mu s$. 157

9.13 The contour plot of temperature distribution in y-z plane($x = 2\pi d$) at $t = 5.32\mu s$. 158

9.14 The contour plot of temperature distribution in y-z plane($x = 2\pi d$) at $t = 8.59\mu s$. 159

9.15 The comparison between the peak and average temperatures within the each x-y plane at time $t = 8.59\mu s$. 160

Chapter 1

Introduction

One of the concerns in design and operation of nozzles used for the injection of combustible mixtures is prevention or at least minimization of hazards associated with preignition of the mixture inside the nozzle. Such an undesirable event may damage or even cause a complete failure of the entire system. In particular, the behavior of high-speed liquid propellant flow has a direct bearing on safety issues (Knapton et al. 1992). Among the various mechanisms that could lead to this undesirable event, it is believed that viscous heating and compression of entrained gas bubble (Nigmatulin & Khabeev 1974; Bourne & Field 1991; Field 1992; Yuan and Prosperetti 1996) play an important role. Our attention is focused here on shear-induced (or viscous) heating effects.

Shear-induced heating effects arise due to the rapid acceleration of the mixture (or fluid) to sufficiently-high velocities which are required to deliver the necessary charge to a combustion chamber (or mixing device). Thus, high shearing rates are established which may result in high-enough temperatures for spontaneous combustion to occur.

The manifestation of shear induced heating effects are believed to be considerably dependent on the mode of injection. For the purpose of this study, we distinguish between the following two injection modes: (i) short-duration injection, in which the charge is impulsively accelerated through the nozzle, and (ii) continuous injection, where a steady mass flow rate develops within the nozzle.

To illustrate the differences between the two modes, we consider the following typical range of nozzle parameters and operating conditions. For both cases, the characteristic nozzle diameter and length are taken as 2 mm and 20 mm, respectively, while the characteristic mixture velocity is roughly 200 m/s. The mixture properties are roughly the same as those of water, so that its density and kinematic viscosity are respectively approximated by $\rho = 1000 kg/m^3$ and $\nu = 10^{-6} m^2/s$. For short-duration injection, the pulse duration is assumed to be approximately $10 ms$.

For continuous injection, the flow field dynamics - and corresponding shear heating rates - may be appropriately interpreted in terms of the flow Reynolds number. In the targeted range of nozzle applications estimated above, the Reynolds number based on the nozzle diameter is in the order of 10^5. Accordingly, both transitional and laminar boundary layers are expected to develop. In the transitional case, shear-induced heating is a result of "laminar" heating within the boundary layer, and intermittent rollup of "large-scale" vortices. When the boundary layer becomes turbulent, shear-induced heating is determined by the mean turbulent temperature distribution (including the "laminar" heating within the viscous sublayer), and the fluctuating component (which is dominated by the presence of wide spectrum of eddy structures).

In the first part of this study, it is argued that the characterization of the flow field as a fully-developed channel flow (whether laminar, transitional, or turbulent) is not appropriate for short-duration injection. In this case, both the evolution flowfield and shear-induced heating mechanism must be interpreted in terms of the thin, unsteady, developing boundary layers which are generated along the nozzle walls. To verify this claim, we start by estimating the typical thickness of the boundary layers due to the diffusion of the vortex sheets which form due to the impulsive acceleration of the mixture. The scaling of the diffusion zone (or boundary layer) may be conservatively estimated through the following measure of the displacement thickness $d^* \sim (\nu t)^{1/2} = 0.1mm$. Thus, during the injection period, viscous effects remain confined to a small region close to solid boundaries. Most of the flow in the channel is still unaffected by viscous diffusion from the wall and remain potential. Noting that the maximum Reynolds number based on displacement thickness is less than 2×10^4, and considering the stabilizing effects of the acceleration of the potential core, it is highly unlikely that any instability mechanism resulting in a transition to turbulence amplifies significantly during such injection durations. Consequently, shear-induced heating associated with pulsed injection modes must be analyzed using the unsteady, primarily laminar, development of thin boundary layers close to the nozzle walls.

Based on the above scaling arguments, it is obvious that different approaches are necessary while simulating shear-induced heating. For continuous injection, the risk of mixture ignition may be best analyzed by investigating the following two possible scenarios:

- The mean temperature distribution exceeds the ignition threshold in a region of the flow.
- The mean temperature distribution is everywhere below the ignition threshold, but sustained temperature excursions of large-enough amplitude may locally exceed this "critical" value.

In analyzing the latter possibility, we are less concerned with high-frequency, high-amplitude turbulent fluctuations, since these fluctuations are least effective in sustaining high shear rates, and are not considered as a likely precursor to mixture ignition. Thus, the contribution of these fluctuations may be modeled as part of the mean "turbulent" temperature distribution. However, it is conceivable that (intermittent) rollup of large-scale energetic eddies in a transitional boundary layer may sustain large-enough viscous heating rates for the temperature to exceed to the critical value.

However, as noted before, it is believed that the above-mentioned phenomena are highly unlikely during short-duration injection. In this case, the primary concern is the maximum temperature attained at or near the nozzle boundaries. Thus, the physical and numerical modeling efforts must focus on obtaining accurate estimates of the wall and boundary-layer temperature distributions. The likelihood of non-Newtonian behavior should also be explored for this type of flow.

Following the above arguments, we shall first focus on a short-duration acceleration of an incompressible Newtonian fluid in a constant-diameter nozzle. Specifically, we were concerned with a simplified channel geometry which still enables us to observe all of the essential shear heating mechanisms, and aimed at determination of peak temperatures experienced by the liquid under flow conditions where the nozzle wall boundary layer is predominantly laminar.

In order to obtain conservative estimates of peak temperatures, an unsteady one-dimensional analysis of the temperature distribution associated with sudden fluid acceleration over a flat insulated boundary is first conducted (Chapter 3). The analysis yields analytical expressions of the prevailing temperature distribution during the early stages of boundary layer formation. In particular, the obtained expressions relate the peak wall temperature to the prevailing Eckert and Prandtl numbers. Results reveal a quadratic dependence of the normalized wall temperature on impulse velocity, and a complex nonlinear variation with Prandtl number. The latter dependence highlights a concern for mixtures having high Prandtl number.

Next, simulation of high-speed flow in an axisymmetric nozzle are performed (Chapter 4). The numerical schemes are based on a finite-difference discretization of vorticity-based momentum, and energy equations. Variants of the formulation are considered which use one of the following approaches:

1. full, unsteady equations of motion on a rectangular grid
2. unsteady parabolized equations of motion on uniform mesh
3. unsteady parabolized equations on stretched grid
4. steady parabolized equations on stretched grid

A numerical study of all four formulations is performed and used to:

- establish the validity of adopting a parabolized approximation
- validate computational results and refine grid stretching techniques
- numerically analyze the impact of inlet velocity and temperature boundary conditions.

Finally, the effects of wall heat transfer (Chapter 5) and temperature-dependent properties (Chapter 6) are discussed.

In the second part of this study, we are focused on modeling of shear-induced heating mechanisms for continuous injection periods, where a steady mass flow rate develops within the channel. For continuous injection, flow-field dynamics in the entire channel section are important. Accordingly, one must be able to characterize the transitional or turbulent flow dynamics across the channel, i.e the mean flow and fluctuations about the mean flow.

In Chapter 7, we obtain the estimates for the mean flow using simple empirical correlations for the mean velocity and energy dissipation, which yields an analytical expression of mean temperature solution. Next, we have tried to characterize the temperature fluctuations of forced isotropic turbulent flow using direct numerical simulation (in Chapter 8). At last, the direct numerical simulation is performed on turbulent channel flow (Chapter 9), where transitional turbulent boundary layer is observed, and the impact of turbulent fluctuations is examined.

Part I

Numerical Study of Laminar Flow

Chapter 2

Numerical approach

2.1 General

As mentioned in the introduction, we are primarily interested in characterizing shear-induced effects during high-speed injection of a combustible mixture into a small diameter nozzle.

For such applications, shear-induced heating effects are primarily concentrated in the viscous boundary layers which develop close to the nozzle boundaries. Furthermore, since these effects depend strongly on shear rates, they will be primarily manifested in the thin section of the nozzle, where the mixture is accelerated to high velocities. Therefore, a proper resolution of boundary layer development in the thin section of the nozzle is clearly seen to be a crucial step in any analysis aiming at the characterization of peak temperatures experienced by the mixture.

In general, accurate resolution of the temperature within the thin boundary layers developed in the thin nozzle section requires a complex analysis which, in particular, must account for the flowfield dynamics upstream of the nozzle section. This is the case because the flow conditions at the inlet of the nozzle may be strongly dependent on the geometry of the converging section and on the upstream flow profile.

The potential differences in inlet conditions from different nozzle geometries may be illustrated by considering a smoothly tapered nozzle, and a nozzle formed by a sudden contraction. No flowfield separation is expected in the first case, resulting in a smooth and monotonic boundary growth across the contraction. When the contraction is sudden, on the other hand, flowfield separation may occur upstream. In this situation, the boundary layer within the thin nozzle section may develop starting from a minute or vanishingly small thickness. Since the largest shear rates scale according to the ratio of the characteristic velocity in the potential core (U) to the inlet boundary layer thickness (δ_0), shear-induced heating mechanisms are expected to be significantly more pronounced in the latter case.

The potential dependence of shear heating rates on nozzle geometry and upstream flow conditions complicates numerical study of the corresponding heating effects. On one hand, the simulation must tackle the geometric complexity of the contraction section – whether smooth or sudden – and accurately describe inflow conditions. On the other hand, detailed flowfield resolution will necessitate restricting the analysis to a limited class of nozzle geometries and flow conditions.

In order to overcome these limitations, a simplified approach to the problem will be adopted in the first part of this study. The approach, which is motivated by our desire to minimize the likelihood of mixture ignition, calls for conservatively estimating peak temperatures by focusing on worst-case scenarios. To this end, the analysis shall assume that the flow conditions at the inlet of the thin nozzle section correspond to a vanishingly small boundary layer thickness and an essentially flat velocity profile. By doing so, simulation of flow dynamics upstream of the nozzle is avoided, and upper bounds on the mixture temperature can be efficiently obtained as a function of the inlet velocity, the nozzle diameter, and the mixture properties.

2.2 Formulation

The physical formulation used in the present study is based on the following assumptions:

- The combustible mixture is an incompressible Newtonian liquid.
- The flowfield within the nozzle remains axisymmetric.

Until section 6, we shall furthermore assume that the mixture has constant properties, so that its motion is governed by the continuity, momentum and energy conservation equations, respectively written as:

$$\nabla \cdot \vec{v} = 0 \tag{2.1}$$

$$\frac{D\vec{v}}{Dt} = -\frac{1}{\rho}\nabla p + \nu\nabla^2 \vec{v} \tag{2.2}$$

$$\rho c_p \frac{DT}{Dt} = k\nabla^2 T + \mu\Phi \tag{2.3}$$

where $\vec{v}$ is the velocity vector, ρ is density, p is pressure, ν is the kinematic viscosity, c_p is specific heat at constant pressure, k is the thermal con ductivity, Φ is the viscous dissipation function, and $\frac{D}{Dt} \equiv \frac{\partial}{\partial t} + \vec{v} \cdot \Delta$ is the material derivative. For an axisymmetric flowfield, the governing equations are recast as:

$$\frac{\partial v_r}{\partial r} + \frac{v_r}{r} + \frac{\partial v_z}{\partial z} = 0 \tag{2.4}$$

$$\frac{\partial v_r}{\partial t} + v_r\frac{\partial v_r}{\partial r} + v_z\frac{\partial v_r}{\partial z} = -\frac{1}{\rho}\frac{\partial p}{\partial r} + \nu(\frac{\partial^2 v_r}{\partial r^2} + \frac{1}{r}\frac{\partial v_r}{\partial r} - \frac{v_r}{r^2} + \frac{\partial^2 v_r}{\partial z^2}) \tag{2.5}$$

$$\frac{\partial v_z}{\partial t} + v_r\frac{\partial v_z}{\partial r} + v_z\frac{\partial v_z}{\partial z} = -\frac{1}{\rho}\frac{\partial p}{\partial z} + \nu(\frac{\partial^2 v_z}{\partial r^2} + \frac{1}{r}\frac{\partial v_z}{\partial r} + \frac{\partial^2 v_z}{\partial z^2}) \tag{2.6}$$

$$\frac{\partial T}{\partial t} + v_r\frac{\partial T}{\partial r} + v_z\frac{\partial T}{\partial z} = \alpha\nabla^2 T + \frac{\nu}{c_p}\Phi \tag{2.7}$$

and the viscous dissipation function is given by:

$$\Phi \equiv 2[(\frac{\partial v_r}{\partial r})^2 + (\frac{v_r}{r})^2 + (\frac{\partial v_z}{\partial z})^2] + (\frac{\partial v_r}{\partial z} + \frac{\partial v_z}{\partial r})^2 \tag{2.8}$$

In the numerical study of high-speed nozzle flow, we shall also rely on the vorticity form of the momentum equations. This alternative formulation is obtained by taking the curl of the momentum equations and using the continuity equation, to get:

$$\frac{\partial \omega}{\partial t} + \frac{\partial}{\partial r}(\omega v_r) + \frac{\partial}{\partial z}(\omega v_z) = \nu(\frac{\partial^2 \omega}{\partial r^2} + \frac{\partial}{pr}(\frac{\omega}{r}) + \frac{\partial^2 \omega}{\partial z^2}) \tag{2.9}$$

where

$$\omega \equiv \nabla \times \vec{v} = \frac{\partial v_r}{\partial z} - \frac{\partial v_z}{\partial r} \tag{2.10}$$

is the vorticity. The latter is related to the radial and streamwise velocity components through a scalar streamfunction, ψ, such that:

$$\begin{aligned} v_r &= -\frac{1}{r}\frac{\partial \psi}{\partial z} \\ v_z &= \frac{1}{r}\frac{\partial \psi}{\partial r} \end{aligned}$$

Substituting the velocity components from Eq. (2.10) into Eq. (2.9) results in the familiar vorticity streamfunction relationship:

$$\frac{\partial}{\partial r}(\frac{1}{r}\frac{\partial \psi}{\partial r}) + \frac{1}{r}\frac{\partial^2 \psi}{\partial z^2} = -\omega \tag{2.11}$$

The advantage of using a vorticity-streamfunctionn formulation in axisymmetric flow is that the continuity equation is naturally satisfied since the velocity field is expressed as the curl of a vector potential (ψ/r), and the number of "unknown" field variables is reduced from three in the primitive variables formulation $(v_r,\ v_z,\ p)$ to two in the present case $(\psi,\ \omega)$.

2.3 Normalization

The numerical simulations discussed in the following sections solve a normalized form of the governing equations. This normalized form is obtained by nondimensionalizing variables with respect to the appropriate combination of the mixture density, ρ, the nozzle radius, R, the maximum velocity at the nozzle inlet, U, and the mixture inlet temperature, T_o. For the choice of characteristic density, length, velocity and temperature scales, the normalized constant-property governing equations are listed in Table 2.1 below.

Table 2.1

Normalized Model Equations for a Constant property
Mixture in Axisymmetric Coordinates

Governing Equations

Vorticity transport

$$\frac{\partial \omega}{\partial t} + \frac{\partial}{\partial r}(\omega v_r) + \frac{\partial}{\partial z}(\omega v_z) = \frac{1}{Re}(\frac{\partial^2 \omega}{\partial r^2} + \frac{\partial}{\partial r}(\frac{\omega}{r}) + \frac{\partial^2 \omega}{\partial z^2}) \tag{2.12}$$

Streamfunction

$$\frac{\partial}{\partial r}(\frac{1}{r}\frac{\partial \psi}{\partial r}) + \frac{1}{r}\frac{\partial^2 \psi}{\partial z^2} = -\omega \tag{2.13}$$

Energy

$$\frac{\partial T}{\partial t} + v_r\frac{\partial T}{\partial r} + v_z\frac{\partial T}{\partial z} = \frac{1}{RePr}\nabla^2 T + \frac{Ec}{Re}\Phi \tag{2.14}$$

Definitions

Velocity field

$$\begin{cases} v_r = -\frac{1}{r}\frac{\partial \psi}{\partial z} \\ v_z = \frac{1}{r}\frac{\partial \psi}{\partial r} \end{cases} \tag{2.15}$$

Viscous dissipation

$$\Phi \equiv 2\left[(\frac{\partial v_r}{\partial r})^2 + (\frac{v_r}{r})^2 + (\frac{\partial v_z}{\partial z})^2\right] + (\frac{v_r}{\partial z} + \frac{\partial v_z}{\partial r})^2 \tag{2.16}$$

Parameters

Reynolds number

$$Re \equiv \frac{\rho U R}{\mu} \tag{2.17}$$

Prandtl number

$$Pr \equiv \frac{\nu}{\alpha} \tag{2.18}$$

Eckert number

$$Ec \equiv \frac{U^2}{c_p T_o} \tag{2.19}$$

Chapter 3

Impulsively-Started Quasi-1d Flow

The model equations given in the previous section indicate that, in the present formulation, the prevailing flow regime within the nozzle is described in terms of three governing parameters: the Reynolds number Re, the Prandtl number Pr, and the Eckert number Ec. In order to gain an appreciation for the impact of these parameters on shear induced heating mechanisms, we first examine the simplified problem of impulsively started motion over a flat insulated plate.

This physical setting, which closely approximates the early stage of boundary layer formations at the nozzle walls, is specified as follows. The flat plate has infinite extent and coincides with the x-axis in the 2D Cartisian $x - y$ plane. The fluid is at rest for times $t < 0$, and is impulsively accelerated to a velocity U at $t = 0$. The flow is unbounded in the $+y$ direction and remains one-dimensional. Under these conditions, the dimensional constant-property momentum equations reduce to:

$$\frac{\partial u}{\partial t} = \nu \frac{\partial^2 u}{\partial y^2} \tag{3.1}$$

with boundary conditions:

$$\begin{cases} u(y=0,t) = 0 \\ u(y \to +\infty, t) = U \end{cases} \tag{3.2}$$

Here, u denotes the streamwise velocity component, and the initial condition may be simply expressed as: $u(y, t=0) = 0$.

The solution of the above heat equation for the streamwise velocity component is given by the well-known similarity solution[1]:

$$u(\eta) \equiv U erf(\eta) \tag{3.3}$$

where $\eta = y/\sqrt{4\nu t}$ is the similarity variable, and

$$erf(\eta) \equiv \frac{2}{\sqrt{\pi}} \int_0^\eta \exp(-x^2) dx \tag{3.4}$$

denotes the error function.

Meanwhile, the dimensional form of the energy equation takes the form:

$$\frac{\partial T}{\partial t} = \alpha \frac{\partial^2 T}{\partial y^2} + \frac{\nu}{c_p} (\frac{\partial u}{\partial y})^2 \tag{3.5}$$

with boundary and initial conditions respectively given by:

$$\begin{cases} \frac{\partial T}{\partial y}(y=0,t) = 0 \\ T(y \to \infty) = T_o \end{cases} \tag{3.6}$$

$$T(y, t=0) = T_o \tag{3.7}$$

3.1 Solutions of the Energy Equation

Analytical solutions of the energy equation (3.5-3.7) are sought using two different techniques. First, we rely a Green's function approach which is based on:

(i) enlarging the solution domain to the entire plane $-\infty \leq y \leq +\infty$

(ii) defining the following extension to the velocity field:

$$u^*(y,t) = Uerf(\frac{|y|}{2\sqrt{\nu t}}) \tag{3.8}$$

(iii) exploiting the symmetry of the extended velocity field by recasting the energy equation as:

$$\frac{\partial T^*}{\partial t} = \alpha\frac{\partial^2 T^*}{\partial y^2} + \frac{\nu}{c_p}(\frac{\partial u^*}{\partial y})^2 = \alpha\frac{\partial^2 T^*}{\partial y^2} + \frac{U^2}{\pi c_p t}\exp(-\frac{y^2}{2\nu t}) \tag{3.9}$$

with boundary and initial conditions respectively given by:

$$T^*(y \rightarrow \pm\infty, t) = T_o \tag{3.10}$$

$$T^*(y, t=0) = T_o \tag{3.11}$$

An analytical expression for the time-dependent solution to the above equations is readily expressed using the Green's function of the heat equation; we have:

$$\begin{aligned} T^*(y,t) = T_o \quad &+ \quad \frac{U^2}{\pi c_p}\int_0^t \sqrt{\frac{\nu}{\tau(2\alpha(t-\tau)+\nu\tau)}} \\ &\times \quad \exp(-\frac{y^2}{2(2\alpha(t-\tau)+\nu\tau)})d\tau \end{aligned} \tag{3.12}$$

While evaluation the above integral is generally cumbersome, simple expressions for the wall temperature, $T_w \equiv T(y=0) = T^*(y=0)$ may be readily obtained. The analytical results are summarized by:

$$\frac{T_w}{T_o} = \begin{cases} 1 + \frac{Ec}{\pi}\sqrt{\frac{Pr}{2-Pr}}(\sin^{-1}(1-Pr) + \frac{\pi}{2}) & Pr < 2 \\ 1 + \frac{2Ec}{\pi} & Pr = 2 \\ 1 + \frac{Ec}{\pi}\sqrt{\frac{Pr}{Pr-2}}\ln(\sqrt{Pr(Pr-2)} + Pr - 1) & Pr > 2 \end{cases} \tag{3.13}$$

It is interesting to note that the wall temperature is time-independent and the above expressions do not explicitly depend on the Reynolds number,due to the absence of a characteristic flow length scale.

In order to obtain solutions for the temperature profile, and to check on the validity of the above expressions, a similarity variable approach is also implemented. To this end, we introduce a new similarity variable,

$$\beta \equiv \frac{y}{\sqrt{\nu t}} \tag{3.14}$$

and postulate that the temperature distribution is a function of β only, i.e. $T = f(\beta)$. Substituting this into Eq. (3.5) yields:

$$f'' + \frac{\nu}{2\alpha}\beta f' + \frac{U^2\nu}{\pi c_p \alpha}\exp(-\frac{\beta^2}{2}) = 0 \tag{3.15}$$

where primes refer to differentiation with respect to β. Multiplying Eq. (3.15) by the integrating factor $\exp(\nu\beta^2/4\alpha)$ and collecting terms gives:

$$(\exp(\frac{\nu}{4\alpha}\beta^2)f')' + \frac{U^2\nu}{\pi c_p \alpha}\exp(-\beta^2(\frac{1}{2} - \frac{\nu}{4\alpha})) = 0 \tag{3.16}$$

Integrating Eq. (3.16) once with respect to β and enforcing the adiabatic wall constraint $f'(0) = 0$ yields:

$$\exp(\frac{\nu}{4\alpha}\beta^2)f' = -\frac{U^2\nu}{\pi c_p \alpha}\int_0^\beta \exp(-x^2(\frac{1}{2} - \frac{\nu}{4\alpha}))dx \tag{3.17}$$

In general, Eq. (3.17) is integrated numerically. However, for special values of Prandtl number, the integration may be easily performed analytically. Specifically, for $Pr = 1$, we have:

$$f(\beta) = T_o + \frac{U^2}{2c_p}(1 - erf(\frac{\beta}{2})^2) \tag{3.18}$$

and in normalized form:

$$\frac{T(\eta)}{T_o} = 1 + \frac{Ec}{2}(1 - erf(\eta)^2) \tag{3.19}$$

Meanwhile, for $Pr = 2$, we get:

$$f(\beta) = T_o + \frac{2U^2}{\pi c_p}\exp(-\frac{\beta^2}{2}) \tag{3.20}$$

and in normalized form:

$$\frac{T(\eta)}{T_o} = 1 + \frac{2}{\pi}Ec\exp(-\eta^2) \tag{3.21}$$

It is easily verified that the wall temperature predicted using the above expressions coincides with that obtained using the Green's function approach.

3.2 Discussion

Results of the above theoretical analysis are depicted in Figs. (3.1-3.3). Fig. (3.1) shows normalized temperature profiles for mixtures with different Eckert and Prandtl numbers. In Figs. (3.2) and (3.3), a mixture having the same heat capacity as water and initially at $295^o K$ is assumed; normalized and dimensional temperature distributions are plotted for different injection velocities and different Prandtl numbers.

Figs. $3.1 - 3.3$ enable us to clearly visualize the roles of the Eckert and Prandtl numbers on shear heating during the early stages of boundary layer formation. In particular, Fig. 3.1 clearly reflects the linear variation of the normalized wall temperature with Eckert number, while Figs $3.2 - 3.3$ reflect a quadratic dependence of the impulse velocity. In addition, the nonlinear dependence of peak temperature on the Prandtl number is also illustrated. The logarithmic divergence of the wall temperature as $Pr \rightarrow \infty$ underscores a particular concern for mixtures having high Prandtl number.

Finally, it is interesting to note that the shear heating predictions of the present 1D analysis are only dependent on the Eckert and Prandtl numbers. Thus, an explicit dependence on the fluid density is lacking from the present predictions. Accordingly, the manifestation of shear-induced heating mechanisms is expected to be similar for incompressible flow conditions characterized by the same Eckert and Prandtl numbers, even if the corresponding mixtures have significantly different densities.

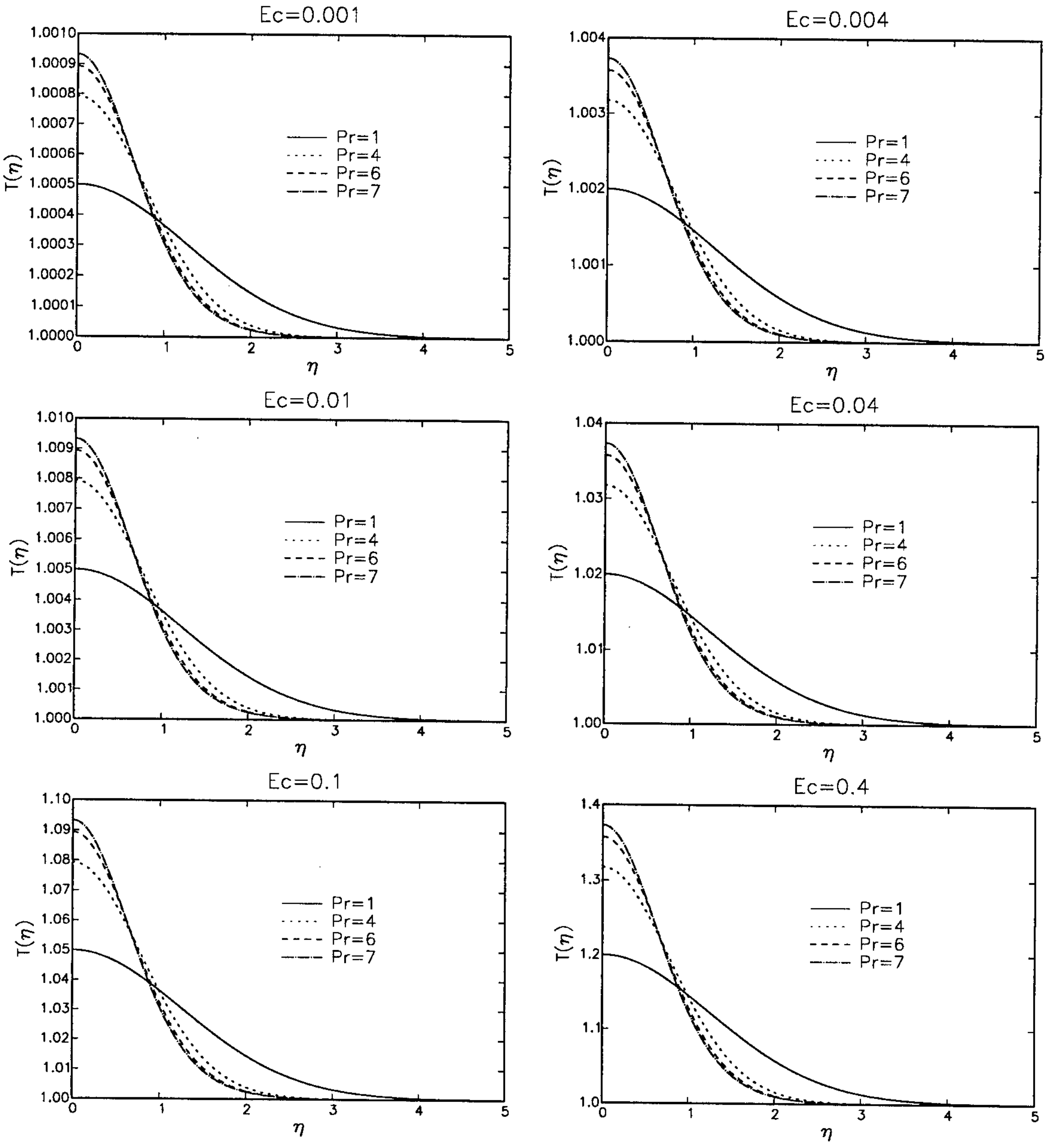

Figure 3.1: Normalized temperature profiles, plotted against the similarity coordinate η, for different Eckert numbers and Prandtl numbers. The value of the Eckert number is indicated.

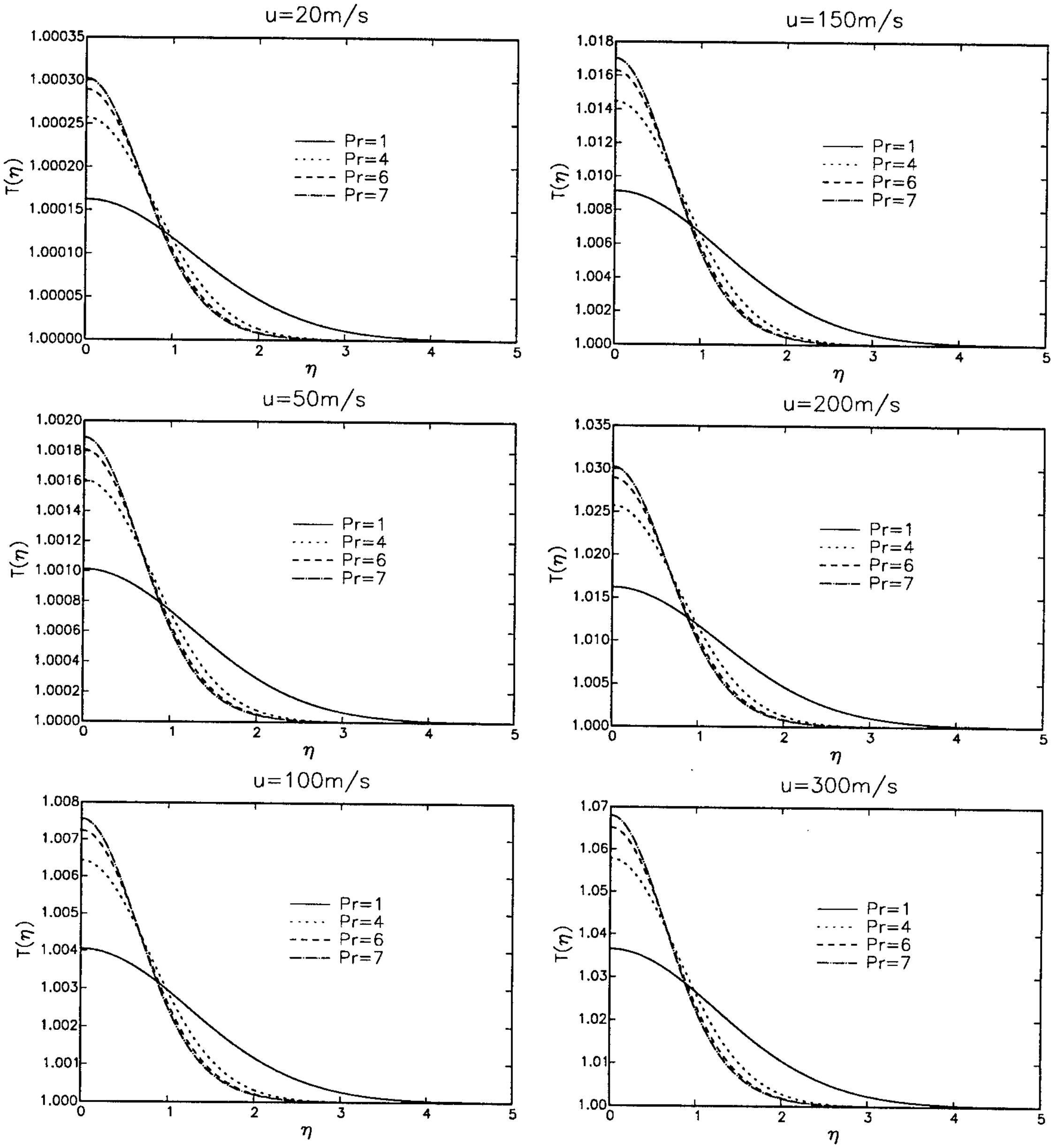

Figure 3.2: Normalized temperature profiles, plotted against the similarity coordinate η, for different injection speeds and Prandtl numbers. The value of injection velocity is indicated.

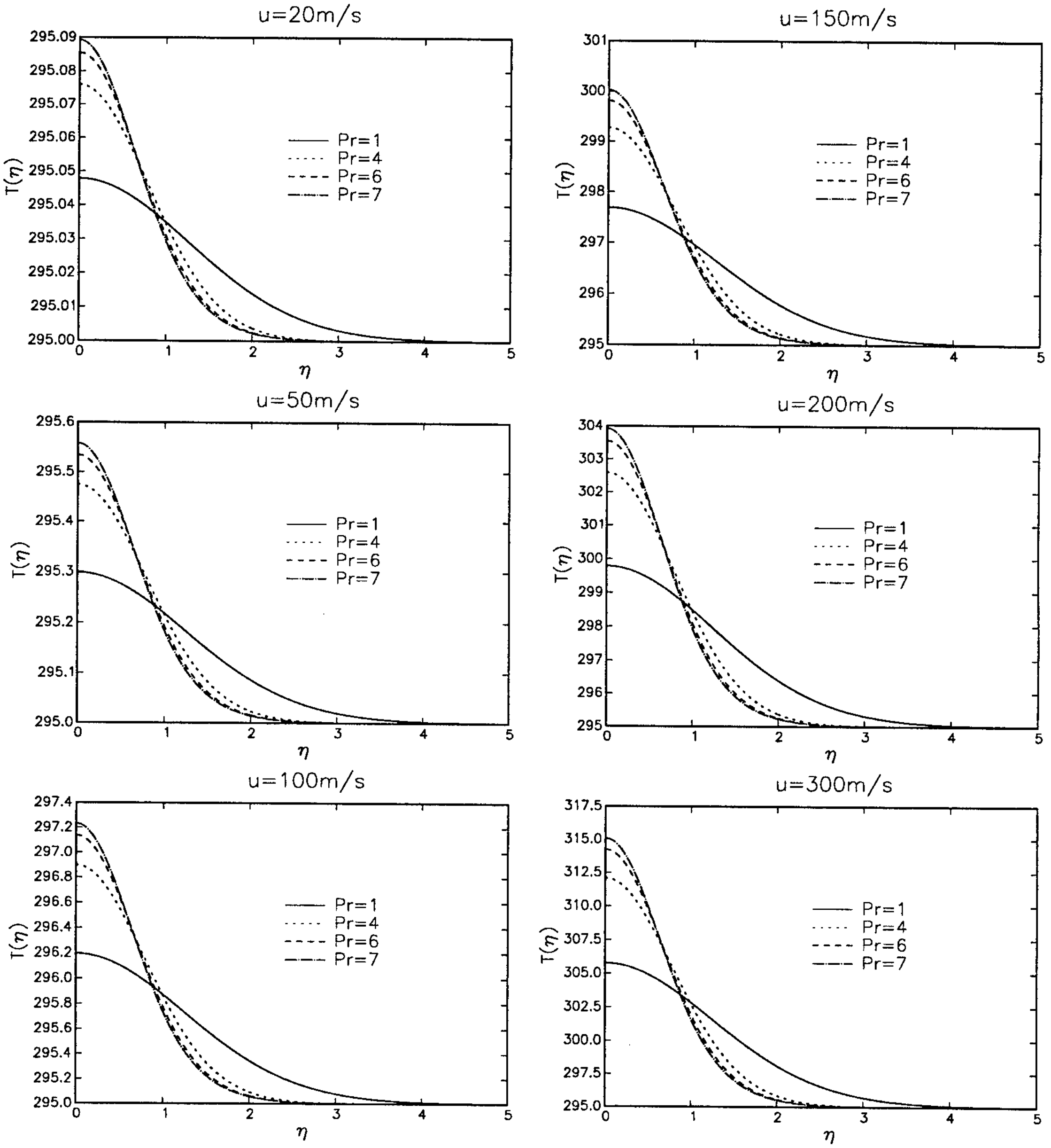

Figure 3.3: Heating of a mixture impulsively accelerated over a flat plate. The mixture is assumed to have the same heat capacity as water and an initial temperature of 295^oK. Temperature profiles are plotted against the similarity coordinate η, for different injection speeds and Prandtl numbers. The value of injection velocity is indicated.

Chapter 4

Axisymmetric Flow

We now turn our attention to the numerical modeling of high-speed injection in an axisymmetric nozzle. Throughout this section, we shall assume:

(i) an incompressible mixture with constant properties,

(ii) that the nozzle has radius $R_o = 2mm$ and length $L = 20mm$, and

(iii) that the nozzle walls are insulated.

Thus, following the discussion of Section 2, we are interested in the simulation of the normalized vorticity transport and energy equation, respectively:

$$\frac{\partial \omega}{\partial t} + \frac{\partial}{\partial r}(\omega v_r) + \frac{\partial}{\partial z}(\omega v_z) = \frac{1}{Re}(\frac{\partial^2 \omega}{\partial r^2} + \frac{\partial}{\partial r}(\frac{\omega}{r}) + \frac{\partial^2 \omega}{\partial z^2}) \tag{4.1}$$

$$\frac{\partial T}{\partial t} + v_r \frac{\partial T}{\partial r} + v_z \frac{\partial T}{\partial z} = \frac{1}{RePr}\nabla^2 T + \frac{Ec}{Re}\Phi \tag{4.2}$$

The boundary conditions associated with the above system of governing equations are summarized as follows:

1. At the nozzle inlet, the velocity and temperature distributions are assumed to be known. Furthermore, we assume that the radial velocity component vanishes at inflow, so that the velocity boundary conditions is given in terms of a streamwise velocity profile, $u_z(r)$. The latter is used to derive streamfunction and vorticity boundary conditions respectively through:

$$\psi_{in}(r) = \int_0^r \zeta u_z(\zeta) d\zeta \tag{4.3}$$

and

$$\omega_{in}(r) = -\frac{\partial u_z}{\partial r}(r) \tag{4.4}$$

Thus, inflow boundary conditions are expressed as:

$$\left\{ \begin{array}{l} \psi(r, z=0) = \psi_{in}(r) \\ \omega(r, z=0) = \omega_{in}(r) \\ T(r, z=0) = T_{in}(r) \end{array} \right. \tag{4.5}$$

2. At the nozzle wall, the potential and no-slip velocity conditions are imposed, as well as the adiabatic surface boundary condition. We thus have:

$$\left\{ \begin{array}{l} \psi(r=1, z) = \int_0^1 r u_z(r) dr \\ \frac{\partial \psi}{\partial r}(r=1, z) = \frac{\partial T}{\partial r}(r=1, z) = 0 \end{array} \right. \tag{4.6}$$

3. At the centerline, axial symmetry conditions are enforced, and the streamfunction value is arbitrarily set to zero. Accordingly, we have:

$$\left\{ \begin{array}{l} \psi(r=0, z) = 0 \\ \frac{\partial T}{\partial r}(r=0, z) = 0 \end{array} \right. \tag{4.7}$$

4. At the downstream computational boundary, derivative outflow conditions are imposed; we have

$$\frac{\partial \psi}{\partial z}(r, z = 20) = \frac{\partial \omega}{\partial z}(r, z = 20) = \frac{\partial T}{\partial z}(r, z = 20) = 0 \qquad (4.8)$$

4.1 Inflow and Initial Conditions

Since the fine details of the mixture injection into the nozzle are generally not known or difficult to determine, impulsively-accelerated flow should be ideally considered. Unfortunately, unlike the 1D theoretical study, this situation is not easily accommodated in the context of a multi-dimensional numerical simulation. First, the early stages of growth of viscous boundary layers, which initially form as infinitely-thin vortex sheets, cannot be adequately captured using finite grid sizes. Second, the imposition of a flat inlet velocity profile would unnecessarily burden the computations, since these cannot handle the associated singular behavior near the nozzle wall.

In order to overcome these difficulties, the initial velocity filed is assumed to admit a small, but finite-thickness boundary layer at the nozzle wall. The velocity profile corresponds to the analytical solution given in the previous section, evaluated at a time significantly smaller than the injection duration. Moreover, the imposed inflow velocity profile is also taken to coincide with the same boundary layer solution. A "brute force" approach is then adopted which calls for decreasing the initial boundary layer until the computed solution is essentially independent of this "free parameter".

Meanwhile, two different approaches are followed in specifying the initial temperature distribution and the inlet temperature boundary condition. The first is analogous to that used for the velocity profile and is based on using the 1D solution to appropriately fit a thermal boundary layer at the nozzle wall. The second approach simply assumes a flat inlet temperature profile. As shown in the computations discussed below, both approaches yield nearly identical peak temperature predictions.

4.2 Direct Numerical Simulation

Direct numerical simulation of the governing equations is first performed. This approach is based on accurate and detailed resolution of all relevant length and time scales using the full equations of motion. To this end, the vorticity transport and energy equations are first discretized in time using the 3rd-order Adams Bashforth scheme, while the viscous dissipation term is treated using the 2nd-order Crank-Nicolson approach. Thus, the time-discretized vorticity and energy equations are expressed as:

$$\frac{\omega^{n+1} - \omega^n}{\Delta t} = -\sum_{k=0}^{2} \gamma_k \left(P^{n-k} + \frac{1}{Re} Q^{n-k}\right) \qquad (4.9)$$

$$\frac{T^{n+1} - T^n}{\Delta t} = -\sum_{k=0}^{2} \gamma_k \left(R^{n-k} + \frac{1}{RePr} S^{n-k}\right) + \frac{Ec}{2Re}\left(\Phi^{n+1} + \Phi^n\right) \qquad (4.10)$$

where

$$P \equiv \frac{\partial(\omega v_r)}{\partial r} + \frac{\partial(\omega v_z)}{\partial z} \tag{4.11}$$

$$Q \equiv \frac{\partial^2 \omega}{\partial r^2} + \frac{\partial}{\partial r}(\frac{\omega}{r}) + \frac{\partial^2 \omega}{\partial z^2} \tag{4.12}$$

$$R \equiv v_r \frac{\partial T}{\partial r} + v_z \frac{\partial T}{\partial z} \tag{4.13}$$

$$S \equiv \nabla^2 T = \frac{1}{r}\frac{\partial}{\partial r}(r\frac{\partial T}{\partial r}) + \frac{\partial^2 T}{\partial z^2} \tag{4.14}$$

respectively denote the convective vorticity, vorticity diffusion convective temperature and thermal diffusion terms, while $(\gamma_0, \gamma_1, \gamma_2) = (23/12, -16/12, 5/12)$ are the integration constants of the 3rd-order Adams-Bashforth scheme.

Spatial discretization of the above equations is performed on regular rectangular grid of mesh size $(\Delta r, \Delta z)$. All "internal" spatial derivatives are treated using second-order centered differences, resulting in the expressions summarized in Table 4.1. Second-order treatment of temperature boundary conditions at the wall is performed, but one-sided first-order differences are used at outflow and the centerline. The standard first-order treatment of the vorticity boundary condition at the wall is also used.

Table 4.1

Discretized Form of Derivative Terms in Standard Notation

Vorticity Convection

$$\begin{aligned} P_{ij} \approx\ & \frac{\omega_{i+1,j}(v_r)_{i+1,j} - \omega_{i-1,j}(v_z)_{i-1,j}}{2\Delta r} \\ & + \frac{\omega_{i,j+1}(v_r)_{i,j+1} - \omega_{i,j-1}(v_z)_{i,j-1}}{2\Delta z} \end{aligned} \tag{4.15}$$

Vorticity Diffusion

$$\begin{aligned} Q_{ij} \approx\ & \frac{\omega_{i+1,j} - 2\omega_{i,j} + \omega_{i-1,j}}{\Delta r^2} + \frac{\omega_{i+1,j} - \omega_{i-1,j}}{2r_i\Delta r} - \frac{\omega_{i,j}}{r_i^2} \\ & + \frac{\omega_{i+1,j} - 2\omega_{i,j} + \omega_{i-1,j}}{\Delta z^2} \end{aligned} \tag{4.16}$$

Temperature Convection

$$R_{ij} \approx (v_r)_{i,j}\frac{T_{i+1,j} - T_{i-1,j}}{2\Delta r} + (v_z)_{i,j}\frac{T_{i,j+1} - T_{i,j-1}}{2\Delta z} \tag{4.17}$$

Thermal Diffusion

$$\begin{aligned} S \approx\ & \frac{T_{i+1,j} - 2T_{i,j} + T_{i-1,j}}{\Delta r^2} + \frac{1}{r_i}\frac{T_{i+1,j} - T_{i-1,j}}{2\Delta r} \\ & + \frac{T_{i,j+1} - 2T_{i,j} + T_{i,j-1}}{\Delta z^2} \end{aligned} \tag{4.18}$$

Viscous Dissipation

$$\begin{aligned} \Phi \approx\ & 2((\frac{(v_r)_{i+1,j} - (v_r)_{i-1,j}}{2\Delta r})^2 + (\frac{(v_r)_{i,j}}{r_i})^2 + (\frac{(v_z)_{i,j+1} - (v_z)_{i,j-1}}{2\Delta z})^2 \\ & + (\frac{(v_r)_{i,j+1} - (v_r)_{i,j-1}}{2\Delta z} + \frac{(v_z)_{i+1,j} - (v_z)_{i-1,j}}{2\Delta r})^2 \end{aligned} \tag{4.19}$$

Vorticity-Streamfunction

$$\frac{\psi_{i+1,j} - 2\psi_{i,j} + \psi_{i-1,j}}{\Delta r^2} - \frac{1}{r_i}\frac{\psi_{i+1,j} - \psi_{i-1,j}}{2\Delta r} + \frac{\psi_{i,j+1} - 2\psi_{i,j} + \psi_{i,j-1}}{\Delta z^2} = -\omega_i r_i \tag{4.20}$$

Velocity Field

$$(v_r)_{i,j} \approx -\frac{1}{r_i}\frac{\psi i, j+1 - \psi i, j-1}{2\Delta z} \tag{4.21}$$

$$(v_z)_{i,j} \approx -\frac{1}{r_i}\frac{\psi_{i+1,j} - \psi_{i-1,j}}{2\Delta r} \tag{4.22}$$

Assuming all quantities known at a given time level, the solution is advanced by one time step as summarized below:

1. Equation (4.9) is first integrated to yield new values of the vorticity everywhere except at solid boundaries.
2. Equation (4.20) is inverted using Gauss-Seidel iterations, thus yielding the streamfunction distribution at the new level.
3. The no-slip boundary condition is imposed using Thom's approximation, giving solid wall vorticity boundary conditions.
4. The velocity distribution is determined using Eqs. $(4.21 - 4.22)$, and the viscous dissipation function at the new time level is computed.
5. The temperature distribution at the new time level is obtained by integrating the energy equation (4.10) and imposing boundary conditions.

4.2.1 Results and Discussion

The direct simulation code is first applied to predict low-speed water injection into the nozzle. The latter is discretized on a rectangular grid with $N_r = 201$ points in the radial direction and $N_z = 801$ in the streamwise direction. A $20m/s$ injection velocity is assumed, corresponding to a Reynolds number $Re = 41,626$. The Prandtl number $Pr = 6.616$, and the Eckert number $Ec = 0.000324$ based on an inlet temperature $T_o = 295^oK$. The inlet and initial velocity and temperature profiles are adapted from 1D analytical expressions of Section 3, assuming an inlet/initial boundary layer thickness $\delta_{in} = 50.8\mu m$. A $10ms$ injection duration is simulated using an integration time step $\Delta t = 0.002\mu s$.

Results of the computations are shown in Figs. 4.1-4.3, which respectively depict streamwise velocity profiles at different injection times, streamwise velocity profiles at different downstream cross-sections, and temperature distributions at different streamwise planes. At early injection times, the figures illustrate the diffusive growth of the viscous and thermal boundary layers. For small downstream locations, $z < 10mm$, the thermal and viscous boundary layers tend rapidly towards a steady-state value, within less than $2ms$ after the start of the injection. Even at large downstream locations, steady state value are reached by the end of the injection period. Examination of the temperature profiles indicates that, for the present injection parameters, shear heating mechanisms are extremely small. Peak temperature values, which are recorded near the nozzle exit, are only 0.18^oK higher than the inlet temperature. It is interesting to note, however, that most of the heating actually occurs during the early stage of injection, during which the boundary layer is thin. Furthermore, comparison of the temperature profiles at different streamwise locations shows that the wall temperature rises rapidly at small downstream locations, where the boundary layer remains thin, and at significantly smaller rates as we move downstream. As discussed in further detail below these trends will also be observed even as the injection speed is considerably increased and shear heating effects become significantly more pronounced.

Unfortunately, one major disadvantage in the application of the direct simulation approach is the high computational overhead associated with the simulation. For the low injection velocity considered above, a $10ms$ injection period required in excess of two weeks to complete on an IBM R6000-350 workstation. For higher injection velocities, which would require significantly finer resolutions, the necessary computational overhead would be prohibitively high. This would be the case even if more efficient versions of the computations were implemented, such as fast solvers, implicit integration schemes, or more accurate spatial discretizations.

In order to overcome this computational difficulty, an alternative approach is adopted which is based on the parabolized approximation of the equations of motion. This results in order-of-magnitude savings in the inversion of the elliptic streamfunction operator, which dominates the overall computational cost. Further reduction of CPU requirements is sought through the implementation of stretched computational grids, which concentrate mesh points in the neighborhood of thin computational boundaries. The construction and implementation of several numerical schemes for the simulation of the parabolized equations of motion are discussed in Section 4.3 below.

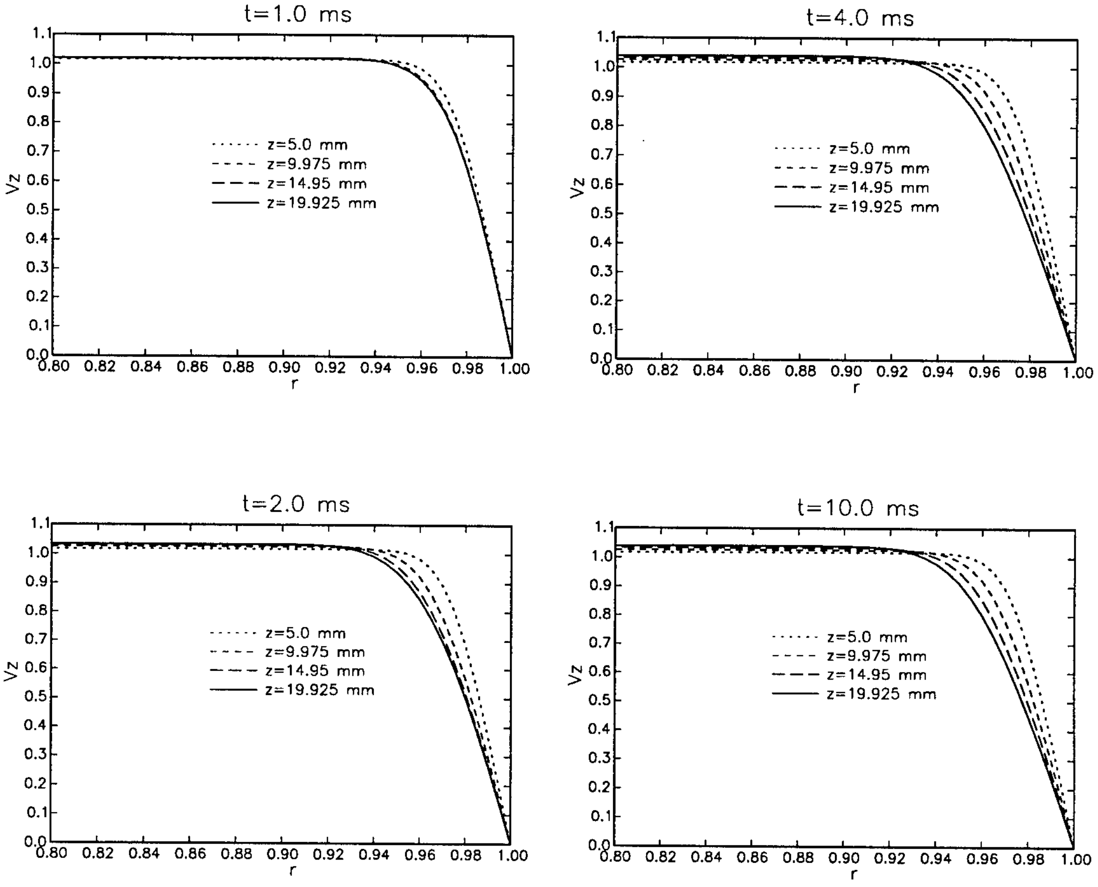

Figure 4.1: Laminar boundary development in an axisymmetric nozzle. Water is injected at $20 m/s$; the nozzle is $20 mm$ long and has $2 mm$ inner radius. The plots show normalized streamwise velocity profiles at different times following injection. In each gragh, profiles at different downstream locations are plotted.

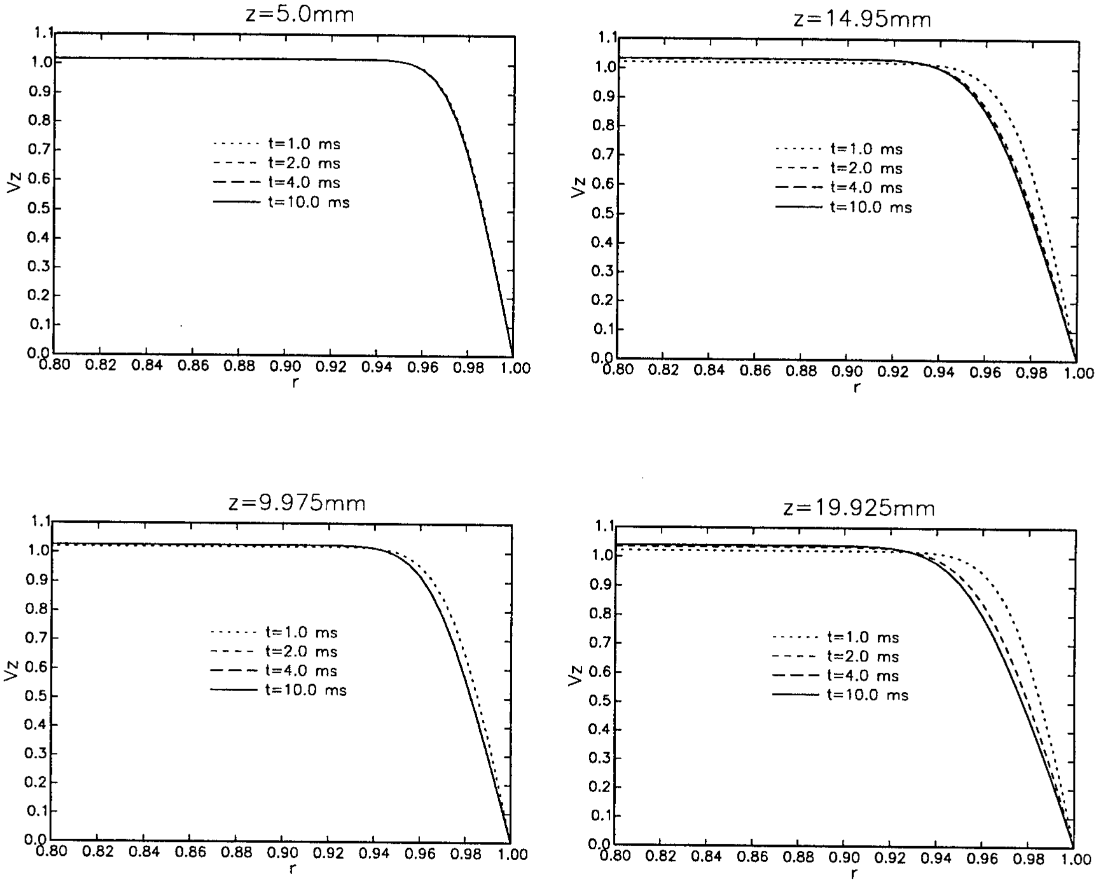

Figure 4.2: Laminar boundary layer development in an axisymmetric nozzle. Water is injected at $20m/s$; the nozzle is $20mm$ long and $2mm$ inner radius. The plots show normalized streamwise velocity profiles at different streamwise locations. In each gragh, profiles at different times following injection are plotted.

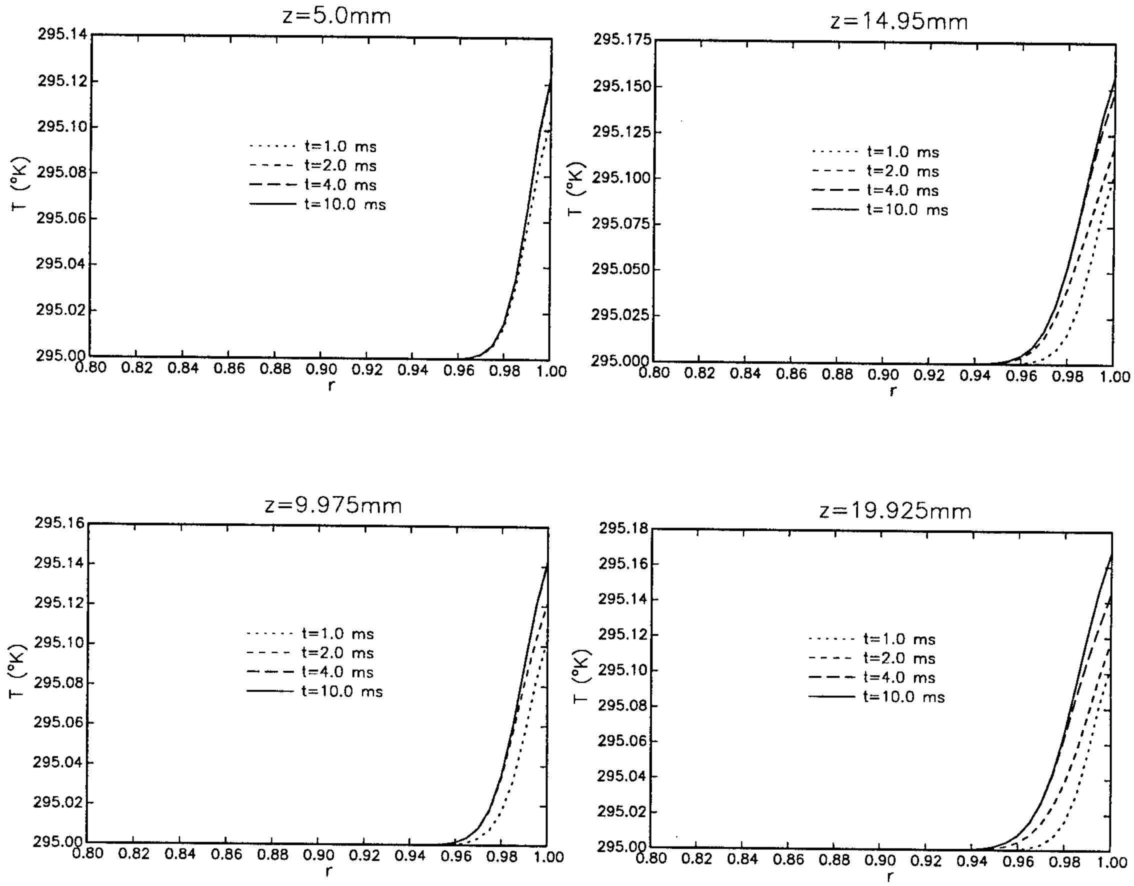

Figure 4.3: Thermal boundary layer development in an axisymmetric nozzle. Water is injected at $20m/s$; the nozzle is $20mm$ long and has $2mm$ inner radius. The plots show normalized temperature profiles at different streamwise locations. In each graph, profiles at different times following injection are plotted.

4.3 Parabolized Approximations

The parabolized approximation is motivated by the fact that in thin boundary layer flows, such as those considered here, radial diffusion fluxes dominate their streamwise counterparts. Thus, the approximation is based on dropping streamwise diffusion terms from the governing equations, resulting in the system summarized in Appendix A.

Numerical simulation of the parabolized equations of motion is performed using a stretched grid technique. To this end, the computational (r, z) plane is stretched in the radial direction only, i.e. using a transformation of the form: $(r, z) \to (\xi, z)$. In all the computations performed in this study, the transformation:

$$r = 1 - \frac{\exp(a(1-\xi)) - 1}{\exp(a) - 1} \tag{4.23}$$

is used. Note that this transformation has a free parameter, a, which may be adjusted depending on the inlet boundary layer thickness and desired numerical resolution. Once a value of a is selected, a standard rectangular finite-difference grid is used in the discretization of the (ξ, z) domain. The equations of motion in the transformed (ξ, z) plane are given in Appendix A, which also discusses the numerical simulation of this equation system.

4.4 Results and Discussion

4.4.1 Validity of the parabolized approximation

Applications of the parabolized simulation codes starts with an examination of the validity of the approximation. To this end, steady and unsteady simulation codes are tested against each other and against the predictions of direct simulations schemes. The same injection parameters selection in Section 4.3 are used.

Comparison of wall temperature and streamwise velocity predictions obtained using the steady parabolized equations and the unsteady parabolized equations at large injection times ($t > 10ms$) reaveal nearly identical results. Thus, we omit discussion of the unsteady parabolized equations, and focus on contrasting predictions of the steady parabolized code and the direct simulation scheme.

Fig. 4.4 shows the streamwise growth of the momentum boundary layer as predicted by the steady parabolized simulation scheme. This simulations are performed on an unstretched square mesh having $N_r = 401$ grid points in the radial direction and $N_z = 8001$ grid points in the streamwise direction. Comparison of these results with those of Figs. 4.1-4.2 reveals a very favorable agreement between both the approaches at large times following the start of injection. This agreement is not surprising since, as mentioned in Section 4.3, the boundary layer thickness has essentially reached its steady value at the late stages of the simulation.

Further comparison between the two prediction schemes is presented in Fig. 4.5, which depicts streamwise velocity profiles at $z = 19.925mm$ downstream of the nozzle inlet. The profiles are drawn using results of the steady parabolized approximation and the unsteady direct simulation at $t = 10ms$ following injection. Again, an excellent agreement between the two approaches is observed, showing only small deviations between the results. It is also interesting to note that the steady parabolized approximation predicts a slightly smaller boundary layer thickness near the nozzle exit. Thus, the parabolized approximation is not expected to overpredict boundary layer growth nor underpredict shear-heating effects.

4.4.2 Further Analysis of Modeling approximation

The efficiency of the parabolized numerical simulation schemes enables detailed study of the free parameters which are part of our modeling approach. As indicated earlier in this section, the initial and inlet conditions used in the simulations assume a quasi 1D flow, so that an inlet momentum boundary layer thickness, and an initial temperature distribution must be provided. thus, it is desirable to first examine the impact of free parameters on the results of the simulations before applying the codes in a predictive manner.

This exercise is conducted for high-speed injection of kerosine. Specifically, an injection velocity $U = 365m/s$ and an inlet temperature $T_o = 293^oK$ are assumed in all the calculations discussed in this section. The physical properties of the liquid are assumed to be constant, and approximated by their value at the inlet temperature; we use $\rho = 806kg/m^3$, $c_p = 2093J/kg.^oK$, $k = 0.1488W/m.^oK$, and $\nu = 2.263 \times 10^{-6}m^2/s$. These injection characteristics are thus characterized by the following values of Reynolds, Prandtl and Eckert numbers: $Re = 322,576$, $Pr = 25.6$, and $Ec = 0.217$.

The effect of the inlet momentum boundary layer thickness, δ_{in}, is first examined. Both steady and unsteady computations are conducted for different values of δ_{in}. Results are summarized in Fig. 4.7, which shows steady-state wall temperature distributions for all cases. A flat inlet temperature profile

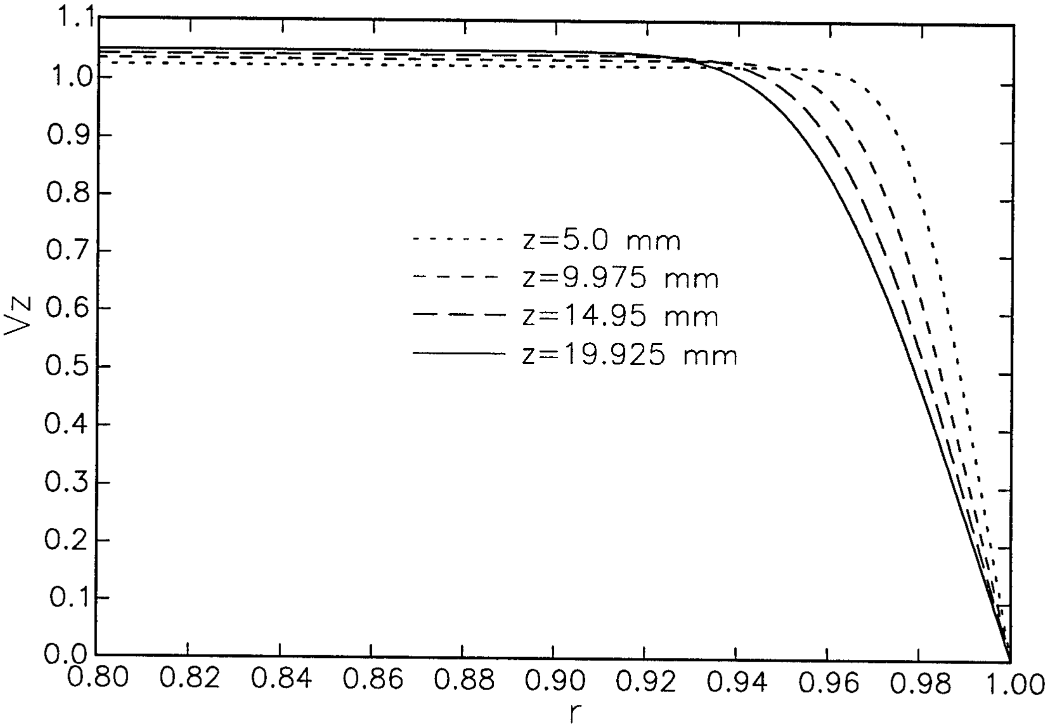

Figure 4.4: Streamwise velocity profiles for the same injection parameters of Fig. 4.1, computed using steady parabolized simulations. The streamwise location is indicated.

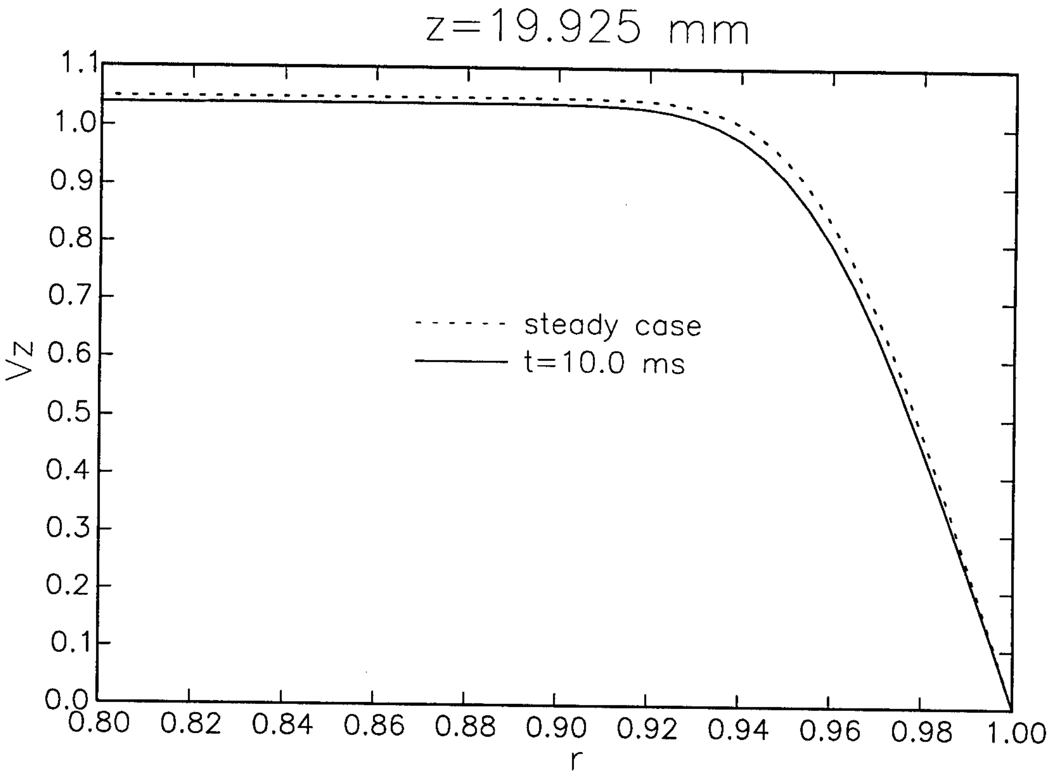

Figure 4.5: Streamwise velocity profiles at $z = 19.925mm$ for the same injection parameters of Fig. 4.2, computed using steady paravolized simulations, and the unsteady direct simulation at $t = 10ms$.

is assumed, and the initial temperature distribution is taken to be uniform. Fig. 4.7 shows that, while the temperature behavior near the nozzle inlet may be strongly affected by the value of δ_{in}, heating characteristics further downstream only show a weak dependence on inlet conditions. In particular, as the inlet momentum boundary layer thickness decreases, the peak wall temperature reached at the nozzle exit exhibits small variation with δ_{in}. Specifically, when the inlet momentum boundary layer thickness becomes of the order of $1\mu m$ or smaller, deviations in the peak temperature within the field are less than 5^oK. This deviation is a very small fraction of the total variation of the wall temperature, which increases by more than 140^oK across the length of the nozzle. Consequently, the effect of the inlet momentum boundary layer thickness may be safely absorbed by consistently decreasing δ_{in} until peak temperature predictions are essentially independent of selected values.

In order to further support this assessment, the predictions of steady and unsteady parabolized approximations are tested against each other. This exercise is summarized in Fig. 4.8 which shows instantaneous wall temperature distributions for the same conditions summarized above, starting with an inlet momentum boundary layer thickness $\delta_{in} = 1.29\mu m$. The computed results indicate that, at early stage, a near-uniform heating of the fluid occurs except near the nozzle inlet where spatial variations of the boundary layer thickness are important. Thus, during early stages of injection, the heating at large downstream locations occurs in a quasi one-dimensional fashion, as assumed in the analysis of section 3.

For larger times, $t > 1.5$ ms, the thermal and viscous boundary layers reach their steady state values in the entire nozzle. Comparison of the wall temperature distribution for $t > 1.5$ ms with corresponding steady state predictions (Fig. 4.7) reveal nearly identical results. An isolated comparison is thus omitted. since the time interval required to reach a steady-state is smaller than the injection duration of interest, the application of a steady analysis to the prediction of peak temperatures proves sufficient. However, the application of unsteady simulation codes is still performed in most applications described in this work, primarily as an additional means of checking the computed predictions. This constitutes a valid approach since, as explained in Appendix A, steady and unsteady simulation codes rely on different discretization and integration methodologies.

Finally, the impact of inlet thermal profile and initial temperature distribution is analyzed. To this end, predictions based on a flat inlet temperature profile and uniform initial temperature distribution are contrasted to those obtained using the quasi-1D results to prescribe the inlet profile and initial distribution. The comparison, performed using steady parabolized approximation with $\delta_{in} = 1.29\mu m$, is shown in Fig 4.9. The figure indicates that, despite significant differences at small downstream locations, steady state predictions of the peak wall temperature near the nozzle exit are weakly sensitive to inlet conditions. When coupled with the results of the above analysis, this enables us to conclude that peak temperature predictions are essentially unsensitive to both thermal and viscous inlet conditions.

4.4.3 Shear Heating of LP 1846 during High-Speed Injection

In this section, the parabolized simulation schemes are applied to characterize shear induced heating during high-speed injection of liquid monopropellant LP 1846. In the computations of this section, an inlet temperature $T_o = 298^oK$ is considered in all cases. Furthermore, the physical properties of LP 1846 are assumed constant and approximated by their value at the injection temperature (see Section 5, below). Specifically, we use $\rho = 1,400 kg/m^3$, $c_p = 2,300 J/kg.^oK$, $k = 0.15 W/m.^oK$, and $\nu = 4.988 \times 10^{-6} m^2/s$.

The impact of injection velocity, is studied by considering four different values: $U = 100 m/s$, $200 m/s$, $300 m/s$, $400 m/s$. The corresponding injection characteristics are respectively characterized by the following Reynolds-Eckert number pairs: $\{Re = 40096, Ec = 0.014\}$, $\{Re = 80191, Ec = 0.058\}$, $\{Re = 120287, Ec = 0.13\}$, and $\{Re = 160384, Ec = 0.23\}$. Since constant property models are applied, all cases are characterized by the same Prandtl number, $Pr = 109.4$.

Results of steady computations are summarized in Fig. 4.10, which shows the wall temperature distribution for all four cases. As in Section 4.4.2, the results are compared to predictions of the unsteady computations in order to check their validity. An illustration of this exercise is given in Fig. 4.11, which shows instantaneous wall temperature distributions for an injection

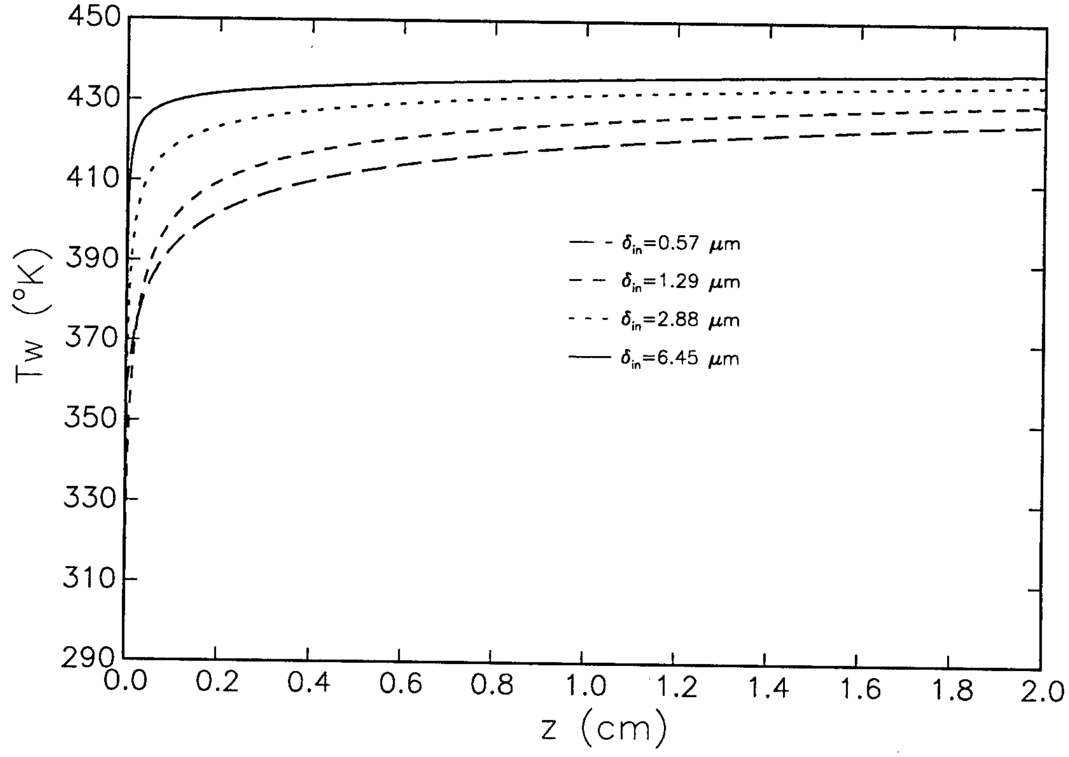

Figure 4.6: Wall temperature distributions during high-speed injection of kerosine with $U = 365m/s$ and $T_o = 293^oK$. The computations are performed using the steady parabolized approximation on a stretched grid woth $N_r = 401$ points in the radial direction and $N_z = 8001$ points in the streamwise direction. The grid stretching parameter $a = 6.5$, amd a flat inlet temperature profile is imposed. The inlet momentum boundary layer thickness δ_{in} is indicated.

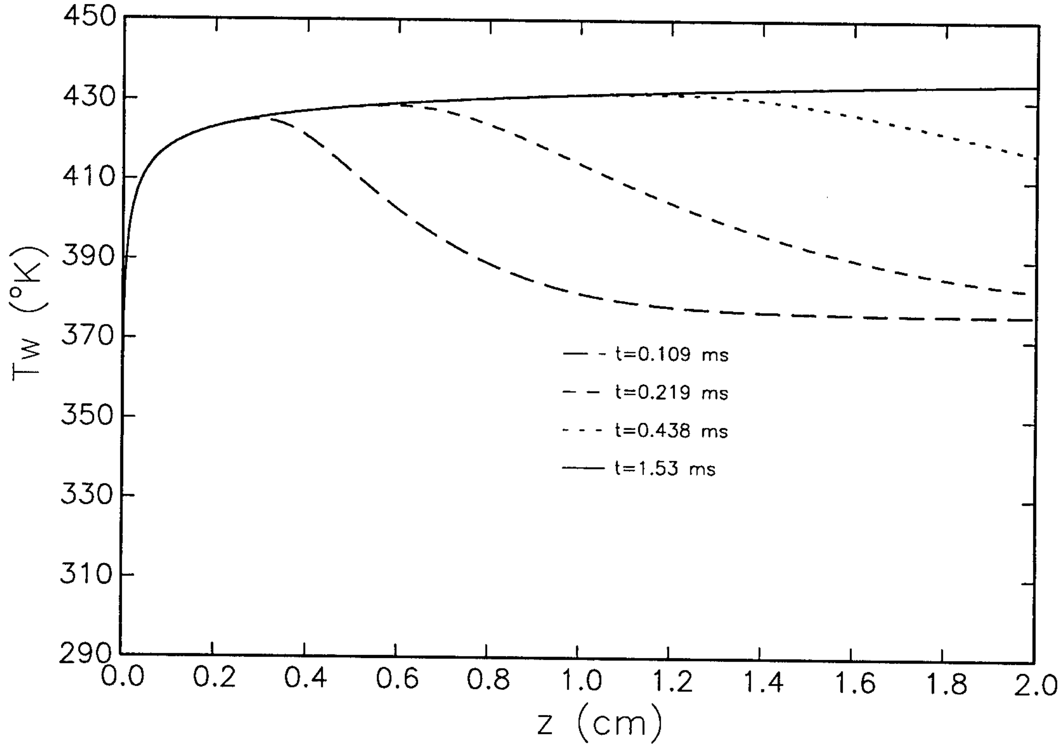

Figure 4.7: Instantaneous wall temperature distributions during high-speed injection of kerosine with $U = 365m/s$ and $T_o = 293^oK$. The computations are performed using the unsteady parabolized approximation on a stretched grid with a stretching parameter $a = 6.5$, $N_r = 401$ points in the radial direction and $N_z = 8001$ points in the streamwise direction. A flat inlet temperature profile is imposed, while the inlet viscous layer has $\delta_{in} = 1.29\mu m$.

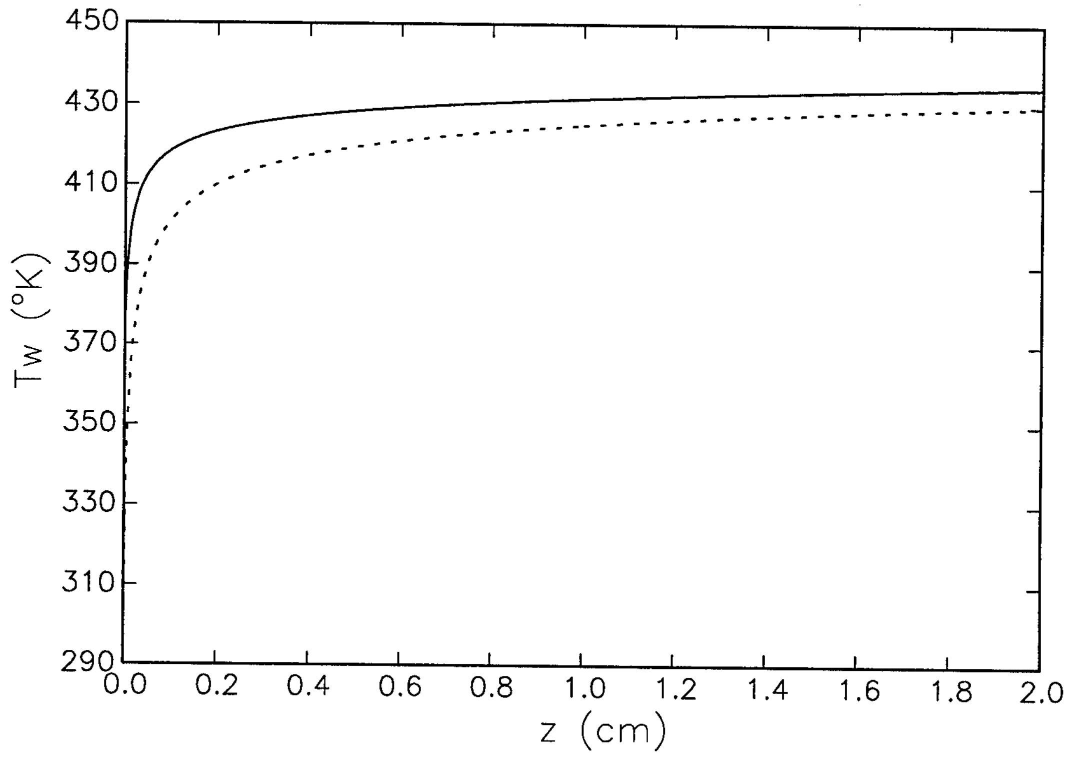

Figure 4.8: Steady state wall temperature distributions for high-speed injection of kerosine with $U = 365m/s$ and $T_o = 293^oK$. The computations are performed using the steady parabolized approximation on a stretched grid with a stretching parameter $a = 6.5$, $N_r = 401$ points in the radial direction and $N_z = 8001$ points in the streamwise direction. The inlet viscous layer has $\delta_{in} = 1.29\mu m$. Results are shown for both flat (dashed line) and non-uniform (solid line) profiles. In the latter case, the inlet temperature profile is adapted from the analysis of section 3.

velocity of $300m/s$. For large times following injection, $t > 1.33ms$, the wall temperature distribution in the unsteady computation coincides with steady state prediction. Thus, a steady field is rapidly reached, well-before the end of injection period.

The computations shown in Fig. 4.10 also reflect the trends of quasi 1D analysis. In particular, the predictions also exhibit a quadratic dependence on the injection velocity. Significant heating of the mixture, with temperature increases greater than a 100^oK, are predicted when the injection velocity exceeds $200m/s$. Thus, for these injection scenarios, premature ignition of the mixture due to severe shear heating is likely to occur.

It is interesting to note that shear heating characteristics for LP 1846 are of the same order as that computed for kerosene. This similarity may be observed by comparing Figs. 4.10 and 4.7. The comparison reveals that the peak wall temperature for a $300m/s$ injection of LP 1846 is close to that achieved for kerosene injection at $365m/s$. Thus, shear heating mechanisms of LP1846 are more pronounced than those of kerosene.

It is also interesting to note that the $300m/s$ injection of LP 1846 is characterized by a smaller Eckert number than kerosene injection at $365m/s$, and that the inlet temperatures in both cases are nearly identical. On the other hand, the Prandtl number of kerosene is significantly smaller than that of LP

1846, which may explain the more pronounced heating effects observed in the latter case. Further discussion of the role of Prandtl, Eckert and Reynolds numbers is provided in Section 5 below.

4.4.4 Effect of Wall Heat Transfer

Finally, the impact of wall heat transfer on peak temperature prediction is investigated. We use a simplified model in which wall heat transfer is taken into account through a convection heat transfer coefficient. Thus, the simplified model ignores the thermal resistance of finite thickness nozzle walls, and also ignores the associated heat storage capacity which may play an important role during the flow transient. Consequently, the model assumes that the nozzle walls are extremely thin and that the limiting heat transfer mechanism from the liquid to its surroundings is due to convection from the nozzle's outer boundaries.

In the computations, convection heat transfer from the nozzle walls is incorporated by modifying thermal boundary condition at the nozzle radius. The modified boundary conditions, which expresses the continuity of the heat flux, is written as:

$$-k\frac{\partial T}{\partial r}|_{r=R_o} = h(T|_{r=R_o} - T_\infty) \tag{4.24}$$

where k is the thermal conductivity of the mixture, h is the heat transfer coefficient and T_∞ is the far-field temperature of the surrounding fluid. In all computations, we assume that the far-field temperature of the surrounding fluid coincides with the inlet mixture temperature, i.e. $T_\infty = T_o$. Substituting this assumption into Eq. (4.24) and normalizing the resulting expression, we get:

$$-\frac{\partial T}{\partial r}(r=1) = Nu(T(r=1)-1) \tag{4.25}$$

where

$$Nu \equiv \frac{hR_o}{k} \tag{4.26}$$

is the Nusselt number based on the mixture's thermal conductivity. Note that insulated wall conditions may also be simulated simply by setting $Nu = 0$, in which case Eq. (4.25) reduces to the homogeneous Neumann Boundary condition.

High speed LP 1846 injection experiments are conducted for different values of the heat transfer coefficient. We select three characteristic values of the heat transfer coefficient, $h = 20W/m^2.^oK$, $h = 100W/m^2.^oK$, and $h = 500W/m^2.^oK$. These values are respectively representative of free convection conditions in air, forced air cooling at low speed, and forced liquid cooling at moderate speed. The corresponding Nusselt numbers defined by Eq. (4.26) are $Nu = 0.267$, $Nu = 1.33$, and $Nu = 6.67$ respectively.

Computed results are shown in Figs. 4.11-4.13, which respectively show peak temperature distributions for LP 1846 injection at $U = 100m/s$, $U =$

$200m/s$,, and $U = 300m/s$. In each plot, curves are drawn for insulated wall conditions ($Nu = 0$) and for three Nusselt number values specified above. Examination of these predictions reveals that:

1. For very high injection speed ($U = 300m/s$) wall heat transfer does not significantly reduce peak temperature predictions even at high Nusselt number. Thus, conventional nozzle wall cooling means may not constitute an effective means of minimizing the likelihood of mixture preignition.
2. For low Nusselt number, $Nu = 267$, the computed peak temperatures are very close to those obtained assuming adiabatic wall conditions. Accordingly, natural heat convection from small diameter nozzles is not expected to significantly affect peak temperature predictions.
3. Large values of the heat transfer coefficient may appreciably reduce peak temperatures in thin walled nozzles whenever the injection velocity is not extremely high. In these situations, forced cooling techniques may be especially tailored in order to effectively minimize the risk of mixture ignition.

It is finally emphasized that, when wall heat transfer is accounted for, the peak temperature achieved at a given streamwise location may not always coincide with the wall temperature. Generally, as heat losses increase, the maximum temperature location moves away from the wall into the thermal boundary layer. This effect is illustrated in Figs 4.14-4.15, which respectively show radial temperature profiles at the nozzle exit for injection velocities $U = 100m/s$ and $300m/s$. Consequently, unlike insulated wall conditions, the peak temperature distributions plotted in Figs. 4.11-4.13 do not always correspond to wall temperature distributions.

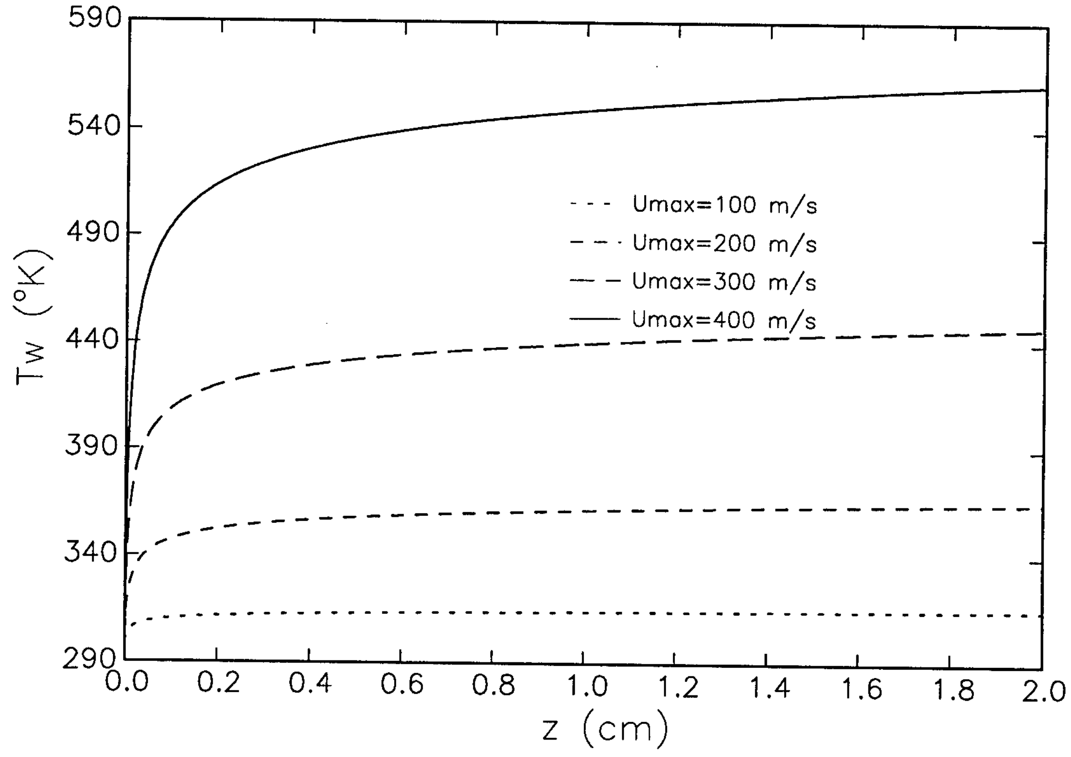

Figure 4.9: Steady state wall temperature distributions for high-speed injection of LP 1846 with $T_o = 298^oK$ at four different velocities, $U = 100m/s$, $U = 200m/s$, $U = 300m/s$, and $U = 400m/s$. The computations are performed using the steady parabolized approximation on a stretched grid with a stretching parameter $a = 6.5$, $N_r = 401$ points in the radial direction and $N_z = 8001$ points in the streamwise direction.

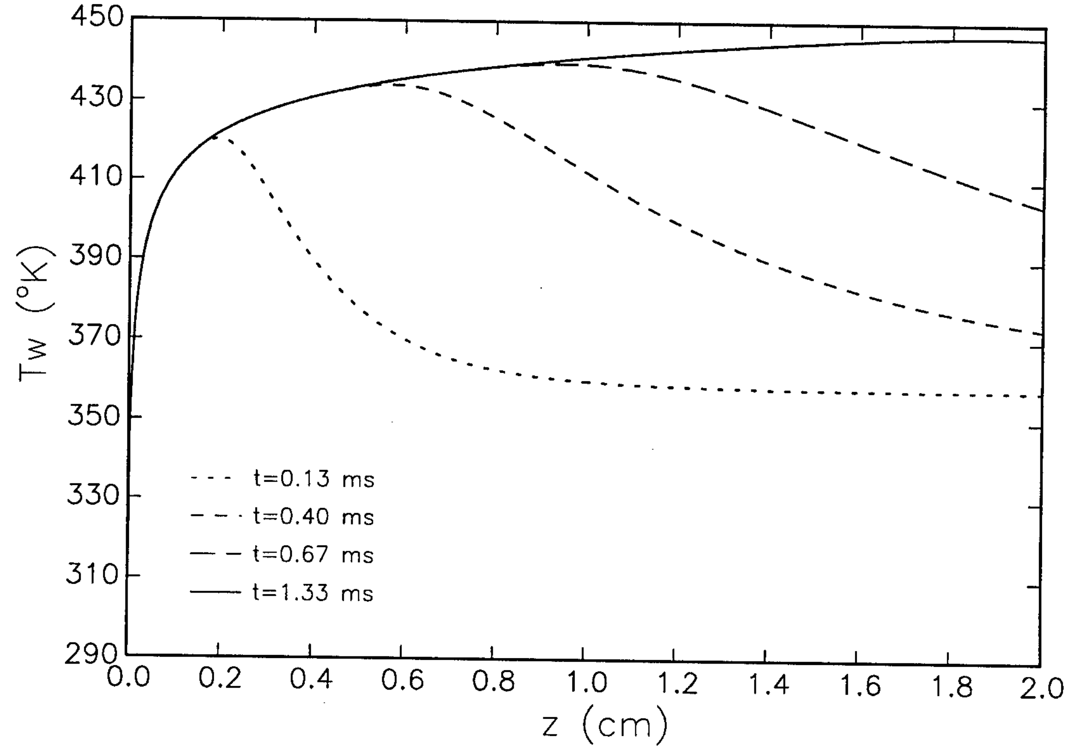

Figure 4.10: Instantaneous wall temperature distribution for high-speed injection of LP 1846 with $T_o = 298^oK$ and $U = 300m/s$. The computations are performed using the unsteady parabolized approximation on a stretched grid with a stretching parameter $a = 6$, $N_r = 201$ points in the radial direction and $N_z = 801$ points in the streamwise direction. The integration time step $\Delta t = 4 \times 10^{-4}$.

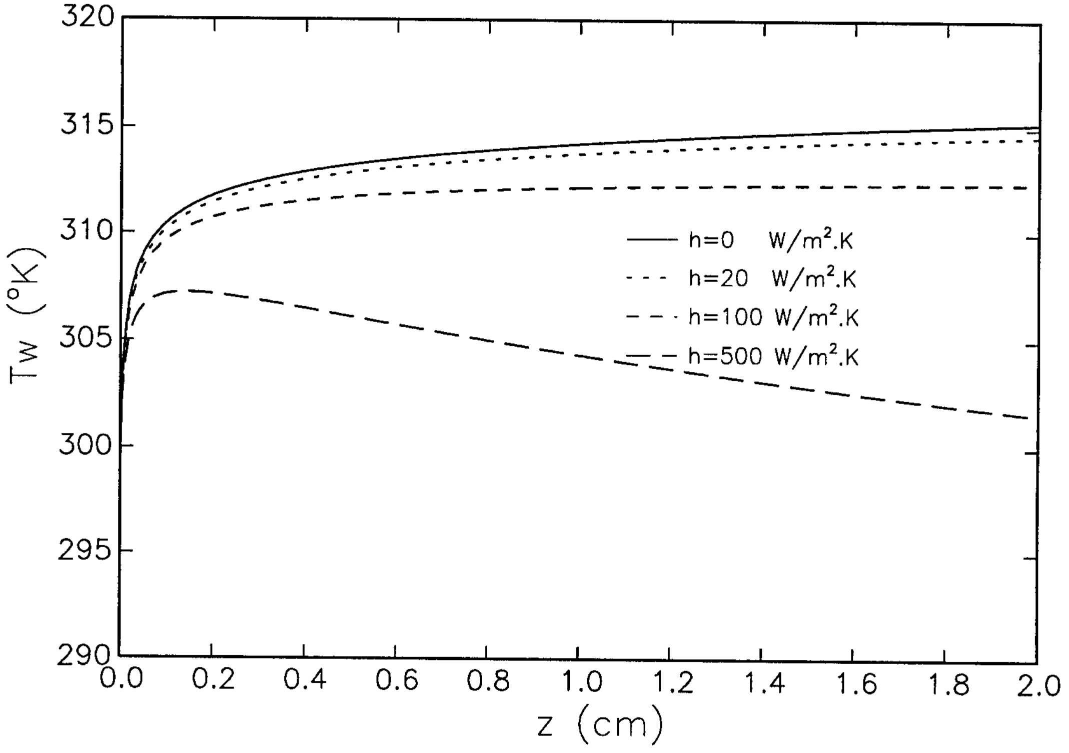

Figure 4.11: Steady state peak temperature distributions for high-speed injection of LP 1648 with $T_o = 298^oK$, $U = 100m/s$, and four different Nusselt number $Nu = 0$, $Nu = 0.267$, $Nu = 1.33$, and $Nu = 6.67$. The computations are performed using the steady parabolized approximation on a stretched grid with a stretching parameter $a = 6.5$, $N_r = 401$ points in the radial direction and $N_z = 8001$ points in the streamwise direction.

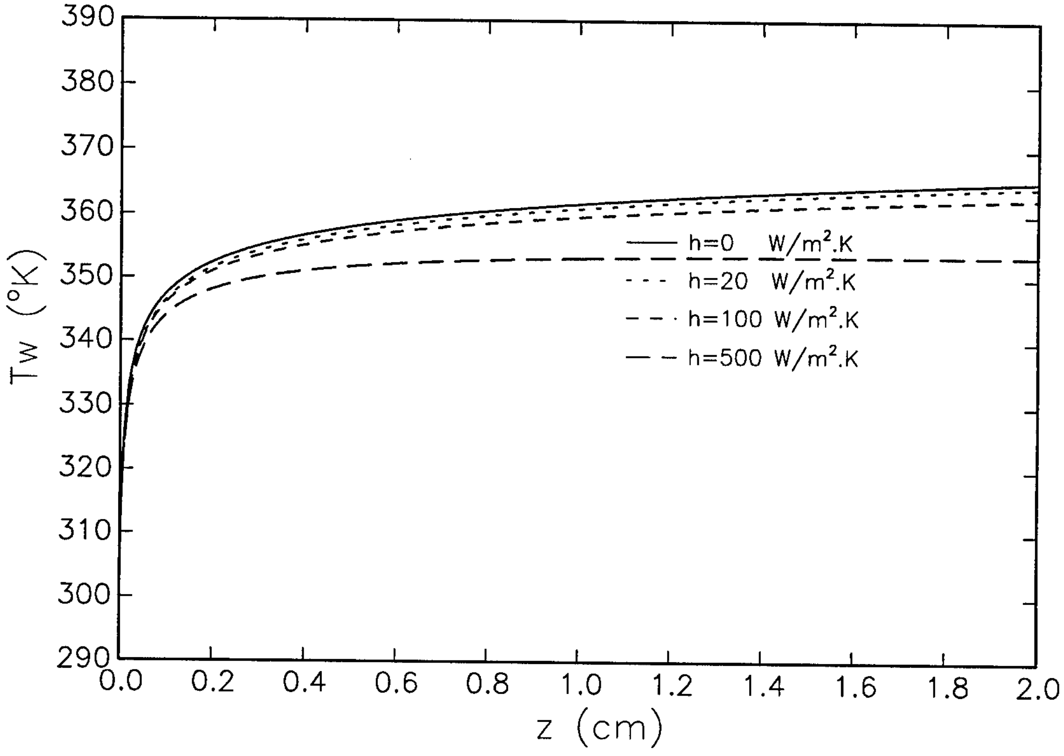

Figure 4.12: Steady state peak temperature distributions for high-speed injection of LP 1648 with $T_o = 298^oK$, $U = 200m/s$, and four different Nusselt number $Nu = 0$, $Nu = 0.267$, $Nu = 1.33$, and $Nu = 6.67$. The computations are performed using the steady parabolized approximation on a stretched grid with a stretching parameter $a = 6.5$, $N_r = 401$ points in the radial direction and $N_z = 8001$ points in the streamwise direction.

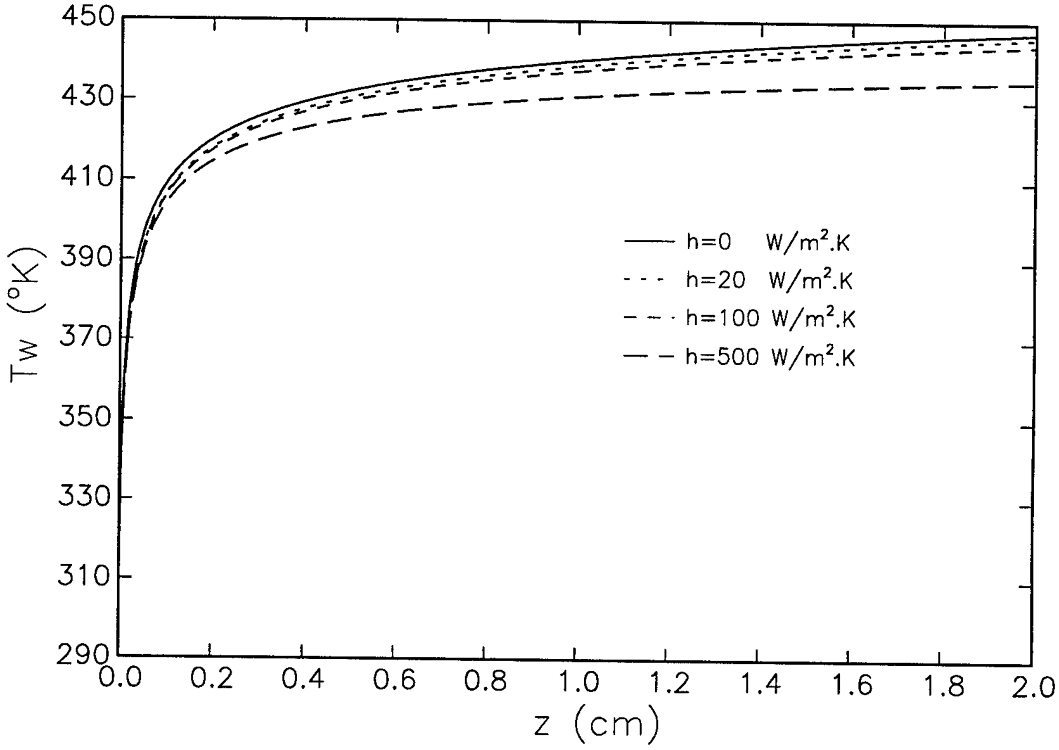

Figure 4.13: Steady state peak temperature distributions for high-speed injection of LP 1648 with $T_o = 298^oK$, $U = 300m/s$, and four different Nusselt number $Nu = 0$, $Nu = 0.267$, $Nu = 1.33$, and $Nu = 6.67$. The computations are performed using the steady parabolized approximation on a stretched grid with a stretching parameter $a = 6.5$, $N_r = 401$ points in the radial direction and $N_z = 8001$ points in the streamwise direction.

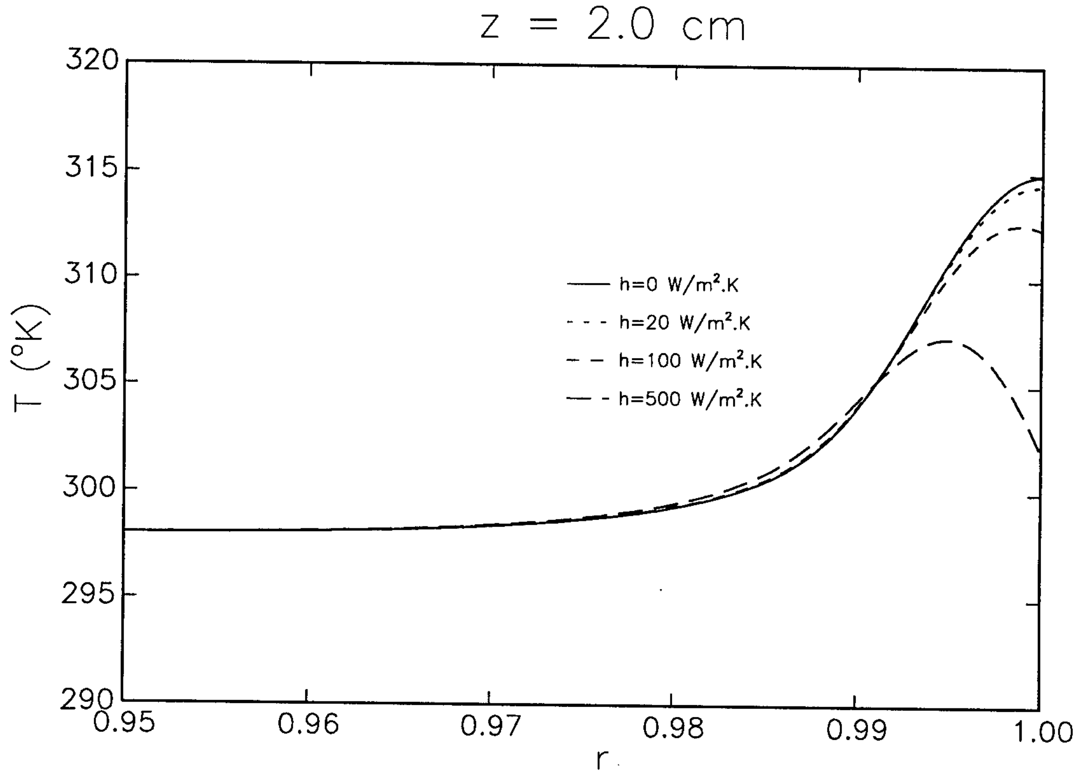

Figure 4.14: Steady state radial temperature profile at the nozzle exit for high-speed injection of LP 1648 with $T_o = 298^o K$, $U = 100 m/s$, and four different Nusselt number $Nu = 0$, $Nu = 0.267$, $Nu = 1.33$, and $Nu = 6.67$. The computations are performed using the steady parabolized approximation on a stretched grid with a stretching parameter $a = 6.5$, $N_r = 401$ points in the radial direction and $N_z = 8001$ points in the streamwise direction.

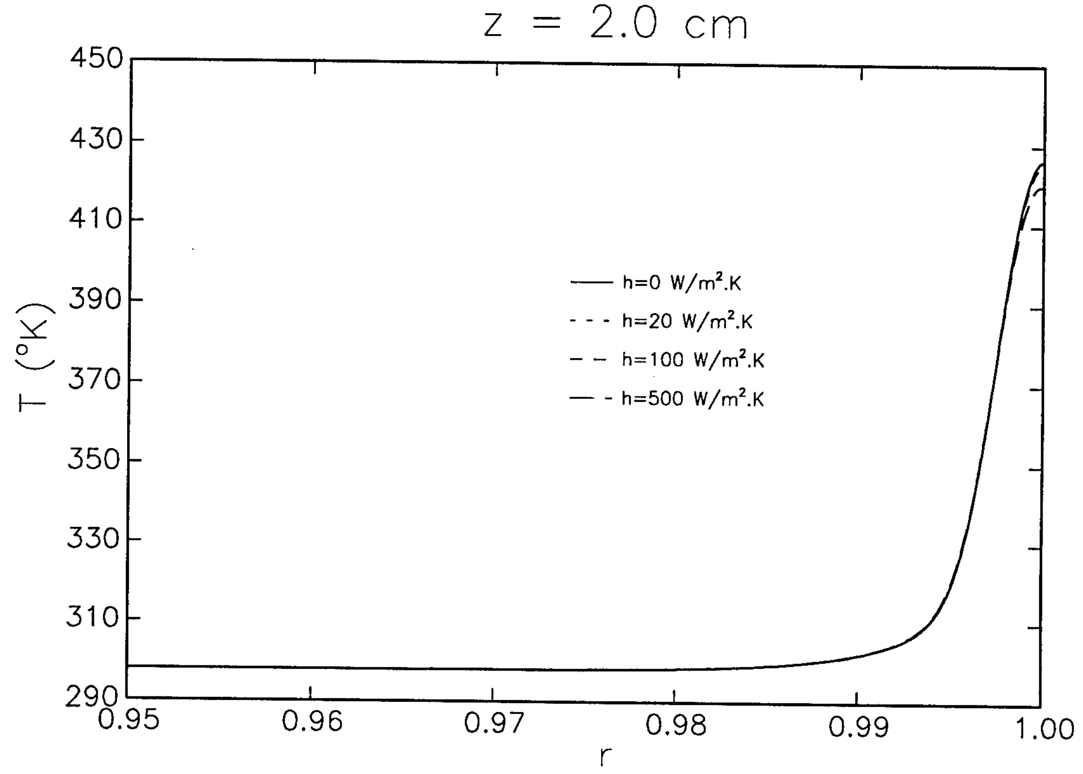

Figure 4.15: Steady state radial temperature profile at the nozzle exit for high-speed injection of LP 1648 with $T_o = 298^oK$, $U = 300m/s$, and four different Nusselt number $Nu = 0$, $Nu = 0.267$, $Nu = 1.33$, and $Nu = 6.67$. The computations are performed using the steady parabolized approximation on a stretched grid with a stretching parameter $a = 6.5$, $N_r = 401$ points in the radial direction and $N_z = 8001$ points in the streamwise direction.

Chapter 5

Variable Mixture Properties

In this section, the constant-properties assumption is relaxed and shear heating mechanisms are examined for a mixture with temperature-dependent viscosity and thermal conductivity. The nozzle geometry and injection regime of interest are identical to those considered in the previous section. However, the accommodation of a variable property mixtures necessitates a significant change both in the governing equations (given in section 5.1) and in the corresponding numerical simulation schemes. The latter are discussed in Appendix B, which summarizes both steady and unsteady schemes for the simulation of the parabolized equations where the temperature dependence of the viscosity and thermal conductivity may not be exactly known. In section 5.3, the computational codes are applied to predict shear-induced heating of liquid monopropellant LP 1846 for different injection speeds, inlet temperatures, and wall cooling conditions.

5.1 Formulation

As in Section 4, we assume that the mixture is an incompressible liquid, and focus on the same injection parameters and nozzle geometries considered there. However, the viscosity and thermal conductivity of the mixture are now allowed to vary with temperature. This generalization does not necessitate any changes in the basic modeling of the flow domain or boundary conditions. Furthermore, all kinematical relationships are left unaffected. Specifically, vorticity-streamfunction relationships and the viscous dissipation function definition introduced in previous sections continue to hold. Thus, we limit our discussion to a simple statement of the vorticity transport and energy conservation equations, whose form changes in order to accommodate the desired extension.

Using the same normalization conventions introduced in Section 2, and introducing the following normalized viscosity and thermal conductivity definitions,

$$\nu^* \equiv \frac{\tilde{\nu}(\tilde{T})}{\tilde{\nu}(\tilde{T}_o)} \tag{5.1}$$

$$k^* \equiv \frac{\tilde{k}(\tilde{T})}{\tilde{k}(\tilde{T}_o)} \tag{5.2}$$

where $\sim$ denotes dimensional quantities, the vorticity transport and energy conservation equations are respectively expressed as:

$$\begin{aligned}\frac{\partial \omega}{\partial t}+\frac{\partial}{\partial r}(\omega v_r) &+ \frac{\partial}{\partial z}(\omega v_z)=\frac{1}{Re}[\nu^*(\frac{\partial^2\omega}{\partial r^2}+\frac{\partial}{\partial r}(\frac{\omega}{r})+\frac{\partial^2\omega}{\partial z^2})\\ &+ \frac{\partial \nu^*}{\partial z}\frac{\partial \omega}{\partial z}+\frac{\partial \nu^*}{\partial r}(2\frac{\partial \omega}{\partial r}+\frac{\omega}{r})+2\frac{\partial^2\nu^*}{\partial z\partial r}(\frac{\partial v_r}{\partial r}-\frac{\partial v_z}{\partial z})\\ &+ (\frac{\partial v_z}{\partial r}+\frac{\partial v_r}{\partial z})(\frac{\partial^2\nu^*}{\partial z^2}-\frac{\partial^2\nu^*}{\partial r^2})] \qquad (5.3)\end{aligned}$$

$$\frac{\partial T}{\partial t}+v_r\frac{\partial T}{\partial r}+v_z\frac{\partial T}{\partial z}=\frac{1}{RePr}[\frac{1}{r}\frac{\partial}{\partial r}(k^*r\frac{\partial T}{\partial r})+\frac{\partial}{\partial z}(k^*\frac{\partial T}{\partial z})]+\frac{Ec}{Re}\nu^*\Phi \qquad (5.4)$$

Here, the Reynolds and Prandtl numbers are based on the viscosity and thermal conductivity measured at the inlet mixture temperature, i.e.

$$Re \equiv \frac{\tilde{\rho}\tilde{U}\tilde{R}}{\tilde{\mu}(\tilde{T}_o)} \qquad (5.5)$$

$$Pr \equiv \frac{\tilde{\nu}(\tilde{T}_o)}{\tilde{\alpha}(\tilde{T}_o)} \qquad (5.6)$$

5.2 Modeling Strategies

The applications discussed in this section are motivated by a desire to characterize the likelihood of preignition due to shear-induced heating of liquid monopropellants during high-speed injection; LP 1846 will be specifically selected in all applications. For this mixture, the dependence of the dynamic viscosity on temperature may be expressed as:

$$\tilde{\mu}=C\exp\left(\frac{D}{\tilde{T}-\tilde{T}_{ref}}\right) \qquad (5.7)$$

where $\tilde{\mu}$ is the viscosity measured in centipoise(cp), $\tilde{T}$ is the temperature measured in Kelvin, $\tilde{T}_{ref}=164^oK$ is a reference temperature while $C=0.16773$

cp and $D = 502.52^o K$ are dimensionalconstants. Unfortunately, the dependence of the thermal conductivity of LP-1846 on the prevailing temperature is not known, and only a single value $\tilde{k}(\tilde{T} = 298^o K) = 0.15 W/m.^o K$ is reported in the literature.

In order to tackle the uncertainty regarding temperature-related variations of the thermal conductivity, two modeling approaches are adopted in the following computations. The first modeling approach is based on the observation that in most liquids, variations of the thermal conductivity are much smaller than those of the dynamic viscosity. Specifically, for most liquids, the dynamic viscosity decreases rapidly with increasing temperature, with corresponding small variation in the thermal conductivity. Accordingly, the Prandtl number is expected to drop appreciably with increasing temperature. Thus, the first model calls for treating the thermal conductivity as temperature-independent, and using the reported value for a mixture at $298^o K$. Since both the density and heat capacity of LP-1846 ($c_p = 2300 J/kg^o K$) vary slightly with temperature, the thermal diffusivity is consequently constant and the first model is called the uniform Peclet number model.

The second modeling approach is motivated by the theoretical findings of Section 3 and the simulation of section 4, which indicate that, other parameters being equal, shear heating effects tend to be significantly more pronounced for mixtures having higher Prandtl number. Thus, the second model conservatively assumes that the thermal conductivity (and consequently the thermal diffusivity) admits a temperature dependence which is similar to that of the dynamic viscosity. Thus, the second model is called the uniform Prandtl number model. It is expected to yield more conservative estimated peak temperatures since it ignores the potential decrease in the Prantle number with increasing temperature. Both models are evaluated in the simulations discussed below.

5.3 Application of LP-1846

Simulation schemes accommodating variable-property mixtures are applied to re-examine the predictions shown in Section 4.4.3. High-speed injection of LP-1846 is once again considered, with injection velocities, $U = 100 m/s$, $U = 200 m/s$, $U = 300 m/s$, and $U = 400 m/s$. In all cases, an injection temperature $T_o = 298^o K$ is assumed. These injection experiments are respectively characterized by the following Reynolds-Eckert number pairs: ($Re = 40096$, $Ec = 0.014$), ($Re = 80109$, $Ec = 0.058$), ($Re = 120287$, $Ec = 0.13$), and ($Re = 160384$, $Ec = 0.23$), and by a Prandtl $Pr = 109.4$. All dimensionless groups are based on properties evaluated at the injection temperature. Unless otherwise stated, adiabatic wall conditions are assumed.

Results of the computations are summarized in Figs. 5.1 and 5.2, which respectively show steady state wall temperature distributions obtained using the uniform Peclet and Prandtl number models. As before, the validity of these predictions are checked against those of unsteady computations. Since a similar agreement to the observed in Section 4.4 is again observed, results of this exercise are omitted.

Comparison of the present results with those obtained in Section 4.4.3 are summarized as follows:

(1) For moderate injection speeds, $U \leq 200m/s$, the predictions of the uniform Peclet number model are very close for those obtained assuming constant properties. At higher injection speeds, the larger temperature variations induced by intense shear heating of the mixture cause a significant deviation between the predictions. The uniform Peclet number model predicts lower steady state peak temperatures than the corresponding constant property simulation. The nature of this deviation is not surprising since the viscosity decreases with increasing temperature, resulting in a drop in the Prandtl number. Thus, by neglecting the temperature dependence of the viscosity, the constant property model yields more conservative estimates of shear induced heating effects.

(2) When the Prandtl number is artificially held constant, an unrealistically large shear heating of the mixture is predicted. Figure 5.2 shows that the uniform Prandtl number model yields peak temperature which, for large injection speeds, may be twice as large as those predicted

by the other two models. These temperature increases are deemed unrealistic since, as previously mentioned, the thermal conductivity drops slightly with increasing temperature while the viscosity decreases more substantially. Thus, by prescribing a temperature dependence of the thermal conductivity which is similar to that of the viscosity, the uniform Prandtl model generally yields overly conservative estimates of shear heating effects and should not, therefore, be relied upon as a reliable predictive tool.

Following the above discussion, only the uniform Peclet number model is used in the computations presented below.

5.3.1 Effect of Wall Heat Transfer

The impact of wall heat transfer is analyzed in a similar fashion to that adopted in constant property simulations. We use the uniform Peclet number model and apply steady parabolized approximation to predict shear heating with heat transfer conditions characterized by the following coefficients: $\tilde{h} = 20W/m^2.^oK$, $\tilde{h} = 100W/m^2.^oK$, and $\tilde{h} = 500W/m^2.^oK$. Note that, since a uniform Peclet number model is used, the thermal conductivity is taken to be constant. Consequently, the Nusselt number definition given in Section 4.3 also holds, and modification of the adiabatic wall condition is performed in an identical manner to that described there.

Results of the computations are summarized in Figs. 5.3 – 5.5, which show that peak temperature distributions for high speed LP 1846 injection with $T_o = 298^oK$, and $U = 100m/s$, $U = 200m/s$, and $U = 300m/s$. Examination of these predictions confirm earlier expectations regarding both the role of heat transfer and the effect of variable properties. Specifically, all the trends established using the constant-property model are once again observed. Moreover, comparison of the results of the uniform Peclet number and constant-property model are also in agreement with adiabatic wall predictions. In particular, when the injection speed is low, results of the uniform Peclet number model are very close to those obtained using constant-property model. For higher injection speeds, temperature variations are significantly more pronounced and the uniform Peclet number model yields smaller peak temperature predictions than those obtained using constant-property simulations.

5.3.2 Effect of injection temperature

Finally, the effect of inlet temperature is investigated. We consider three injection speeds, $U = 100m/s$, $U = 200m/s$, and $U = 300m/s$, and assume adiabatic nozzle wall conditions. Results of steady parabolized approximations are shown in Figs. 5.6 – 5.8, which respectively show wall temperature distributions for three inlet temperatures, $T_o = 278^oK$, $T_o = 298^oK$, and $T_o = 318^oK$.

For low injection speed, $U = 100m/s$, the effects of shear-induced heating are essentially similar for all inlet temperatures. For these injection characteristics, moderate heating in the thermal boundary layer occurs, and the wall temperature distributions for different cases appear to be shifted vertically as the inlet temperature is varied. This result is not surprising, and is in agreement with previous results, since the temperature distributions – and consequently the viscosity – do not exhibit large variations.

At higher injection speeds, $U = 200m/s$, variable viscosity effects start becoming more pronounced. Figure 5.7 indicates that shear heating of the mixture is more substantial as the inlet temperature is decreased. Note that, for lower inlet temperatures, the inlet viscosity of the mixture is higher. Therefore, shear stresses and viscous dissipation are also higher; this results in larger wall temperature increases. This trend can also be interpreted in terms of the expectation, established earlier in the context of quasi 1D flow and constant-property simulations, that shear heating effects are pronounced for mixtures with higher Prandtl number. The present results are consistent with this trend, since the inlet Prandtl number increases with decreasing temperature.

Another important observation is that, at high injection velocities, all similarity between wall temperature distributions is lost as the inlet temperature developed at low injection temperatures may exceed that corresponding to higher inlet temperature. Further examination of the computations indicates that these trends are due to different development of both the thermal and viscous boundary layers. Specifically, as illustrated in Figs. 5.9-5.10, when intense shear-heating of the mixture occurs, both the structure and spatial evolution of the boundary layer exhibit significant differences as the inlet temperature is varied.

The observed dependence of shear heating effects on the injection temperature appears to pose a significant challenge to the evaluation of the likelihood of mixture ignition. However, it should be noted that this dependence admits a consistent trend, namely that injection characteristics having higher inlet Prandtl number exhibit higher temperature increases. Thus, conservative estimates of shear heating effects can still be obtained by focusing the analysis on injection conditions which are characterized by the highest anticipated Prandtl number.

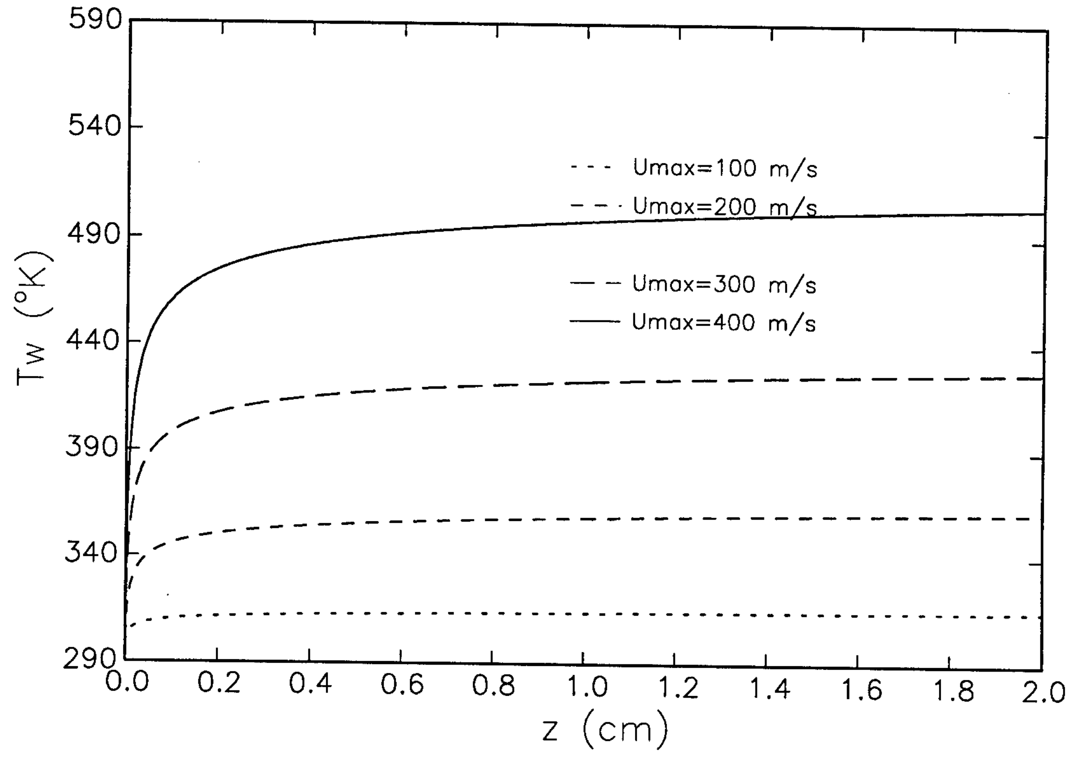

Figure 5.1: Steady state wall temperature distribution for high-speed injection of LP 1648 with $T_o = 298^oK$ at four difference velocities, $U = 100m/s$, $U = 200m/s$, $U = 300m/s$, and $U = 400m/s$. The uniform Peclet number model is adopted, and the computations are performed using the steady parabolized approximation on a stretched grid with a stretching parameter $a = 6.5$, $N_r = 401$ points in the radial direction and $N_z = 8001$ points in the streamwise direction.

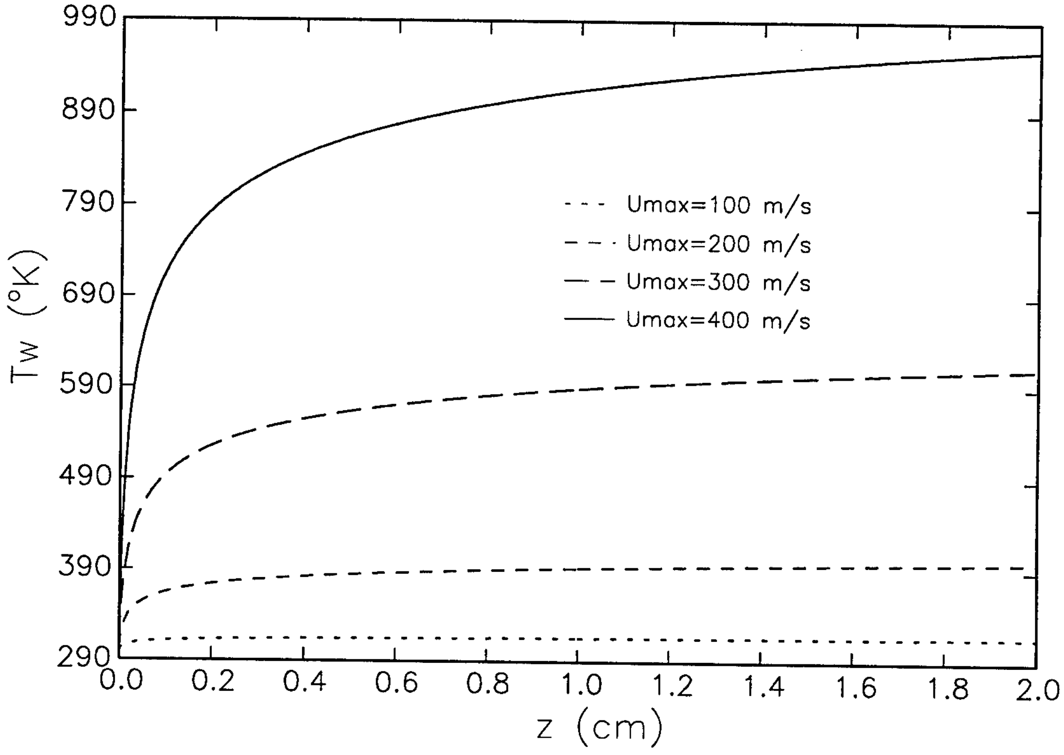

Figure 5.2: Steady state wall temperature distribution for high-speed injection of LP 1648 with $T_o = 298^oK$ at four difference velocities, $U = 100m/s$, $U = 200m/s$, $U = 300m/s$, and $U = 400m/s$. The uniform Prandtl number model is adopted, and the computations are performed using the steady parabolized approximation on a stretched grid with a stretching parameter $a = 6.5$, $N_r = 401$ points in the radial direction and $N_z = 8001$ points in the streamwise direction.

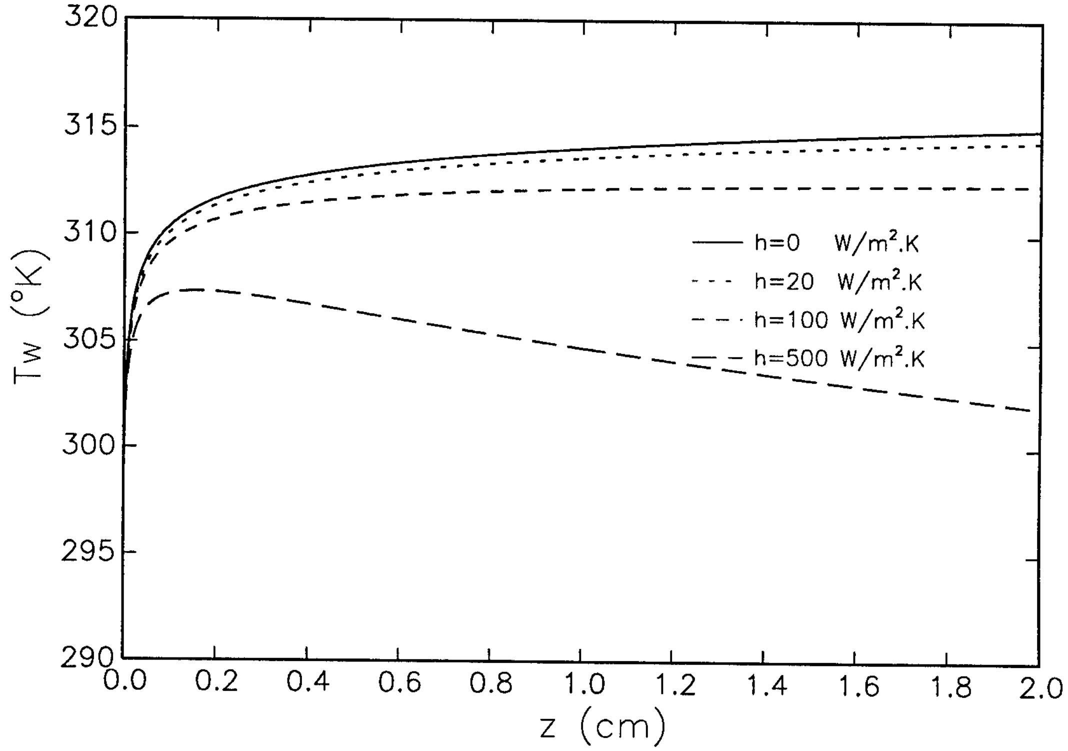

Figure 5.3: Steady state peak temperature distribution for high-speed injection of LP 1648 with $T_o = 298^oK$, $U = 100m/s$, and four different Nusselt number $Nu = 0$, $Nu = 0.267$, $Nu = 1.33$, and $Nu = 6.67$. The uniform Peclet number model is adopted, and the computations are performed using the steady parabolized approximation on a stretched grid with a stretching parameter $a = 6.5$, $N_r = 401$ points in the radial direction and $N_z = 8001$ points in the streamwise direction.

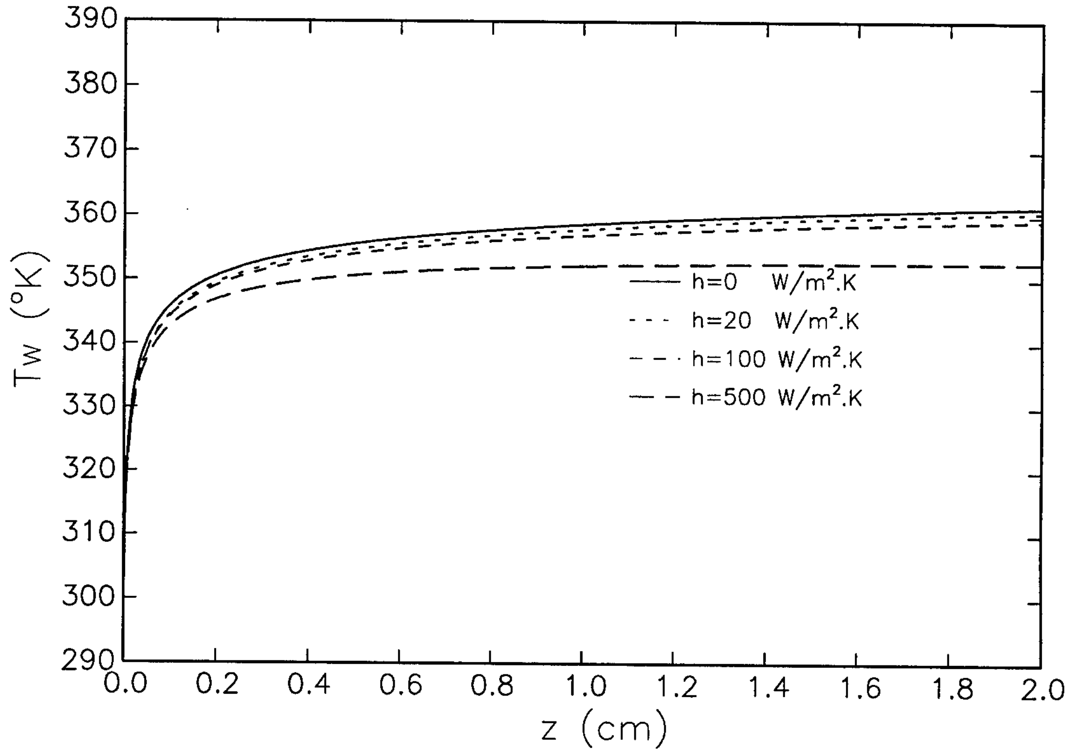

Figure 5.4: Steady state peak temperature distribution for high-speed injection of LP 1648 with $T_o = 298^o K$, $U = 200 m/s$, and four different Nusselt number $Nu = 0$, $Nu = 0.267$, $Nu = 1.33$, and $Nu = 6.67$. The uniform Peclet number model is adopted, and the computations are performed using the steady parabolized approximation on a stretched grid with a stretching parameter $a = 6.5$, $N_r = 401$ points in the radial direction and $N_z = 8001$ points in the streamwise direction.

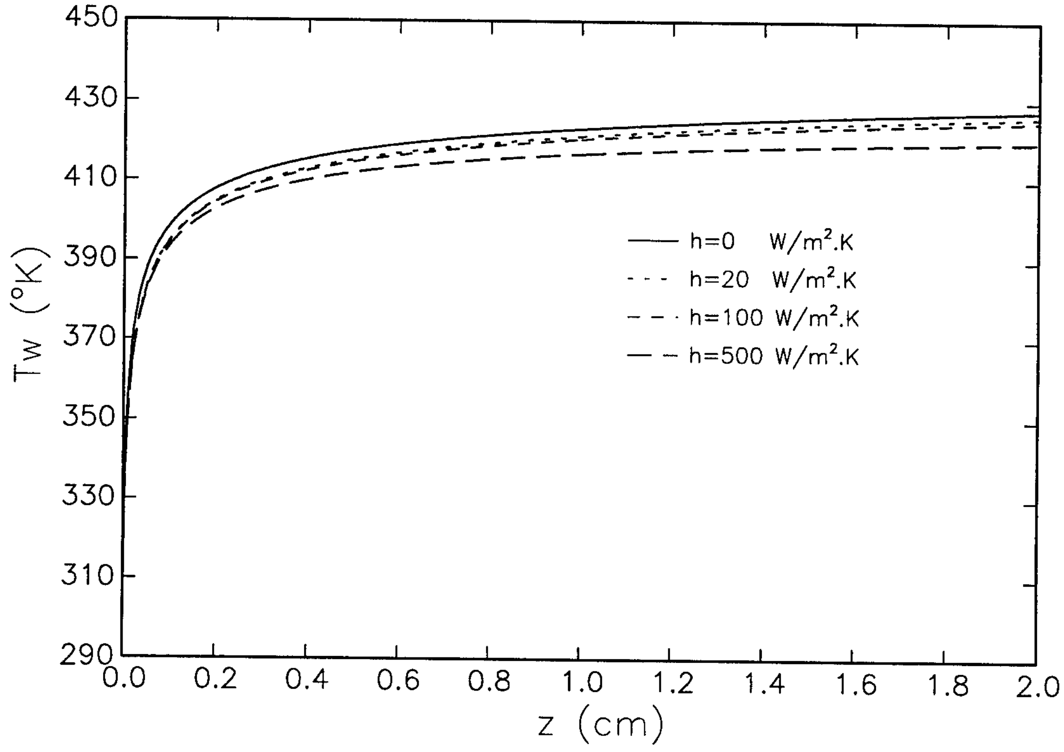

Figure 5.5: Steady state peak temperature distribution for high-speed injection of LP 1648 with $T_o = 298^o K$, $U = 300 m/s$, and four different Nusselt number $Nu = 0$, $Nu = 0.267$, $Nu = 1.33$, and $Nu = 6.67$. The uniform Peclet number model is adopted, and the computations are performed using the steady parabolized approximation on a stretched grid with a stretching parameter $a = 6.5$, $N_r = 401$ points in the radial direction and $N_z = 8001$ points in the streamwise direction.

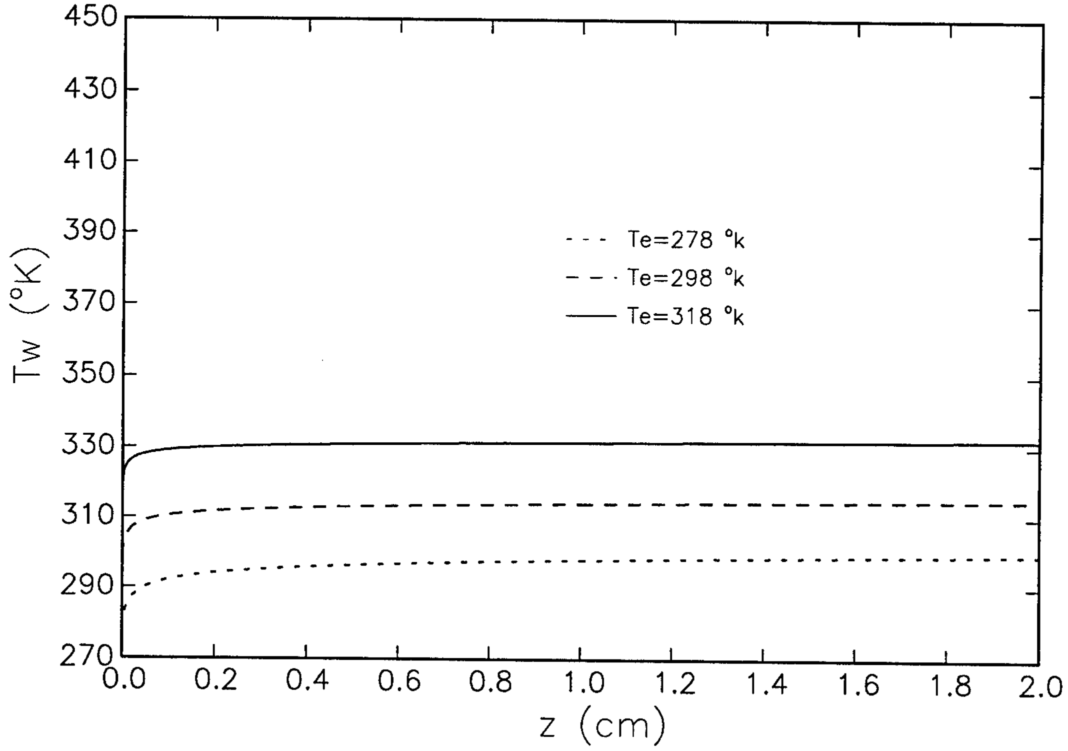

Figure 5.6: Steady state peak temperature distribution for high-speed injection of LP 1648 with $U = 100m/s$, and three different inlet temperatures $T_o = 278^oK$, $T_o = 298^oK$, and $T_o = 318^oK$. The uniform Peclet number model is adopted, and the computations are performed using the steady parabolized approximation on a stretched grid with a stretching parameter $a = 6.5$, $N_r = 401$ points in the radial direction and $N_z = 8001$ points in the streamwise direction.

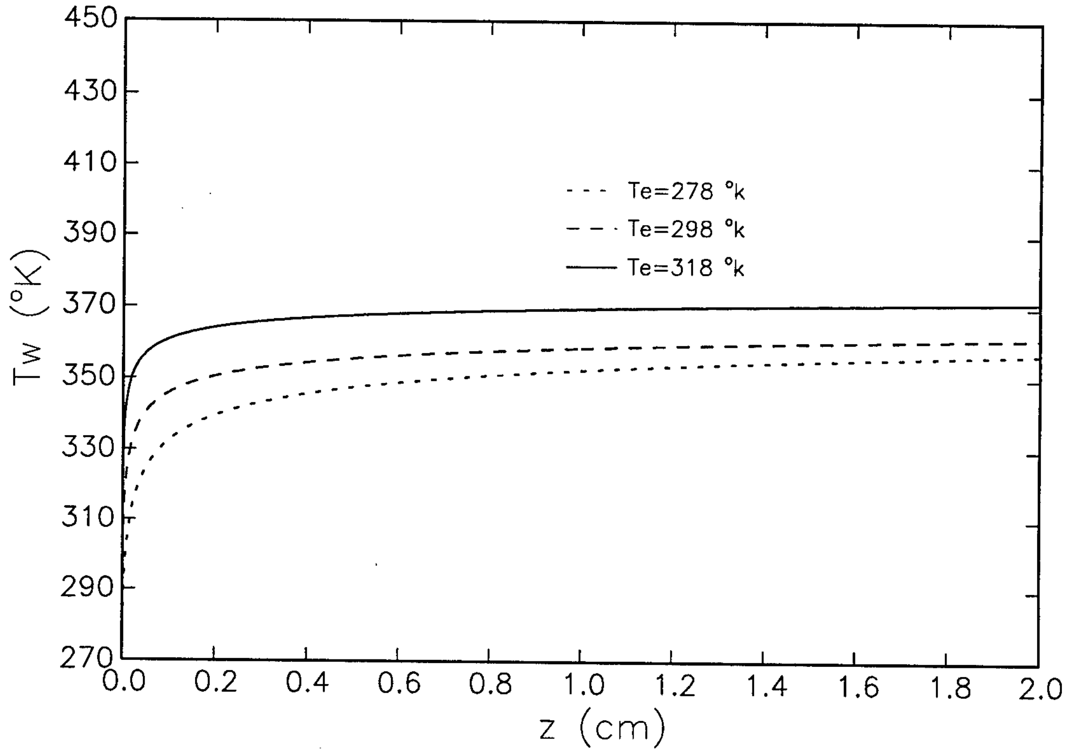

Figure 5.7: Steady state peak temperature distribution for high-speed injection of LP 1648 with $U = 200m/s$, and three different inlet temperatures $T_o = 278^oK$, $T_o = 298^oK$, and $T_o = 318^oK$. The uniform Peclet number model is adopted, and the computations are performed using the steady parabolized approximation on a stretched grid with a stretching parameter $a = 6.5$, $N_r = 401$ points in the radial direction and $N_z = 8001$ points in the streamwise direction.

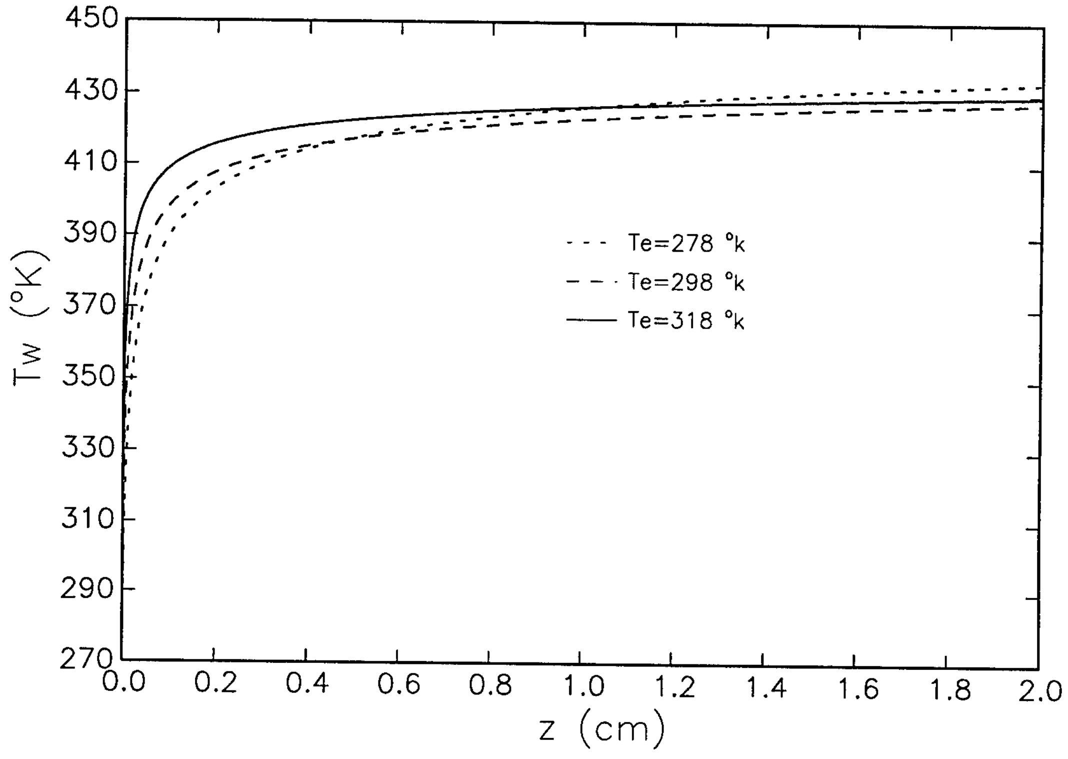

Figure 5.8: Steady state peak temperature distribution for high-speed injection of LP 1648 with $U = 300m/s$, and three different inlet temperatures $T_o = 278^oK$, $T_o = 298^oK$, and $T_o = 318^oK$. The uniform Peclet number model is adopted, and the computations are performed using the steady parabolized approximation on a stretched grid with a stretching parameter $a = 6.5$, $N_r = 401$ points in the radial direction and $N_z = 8001$ points in the streamwise direction.

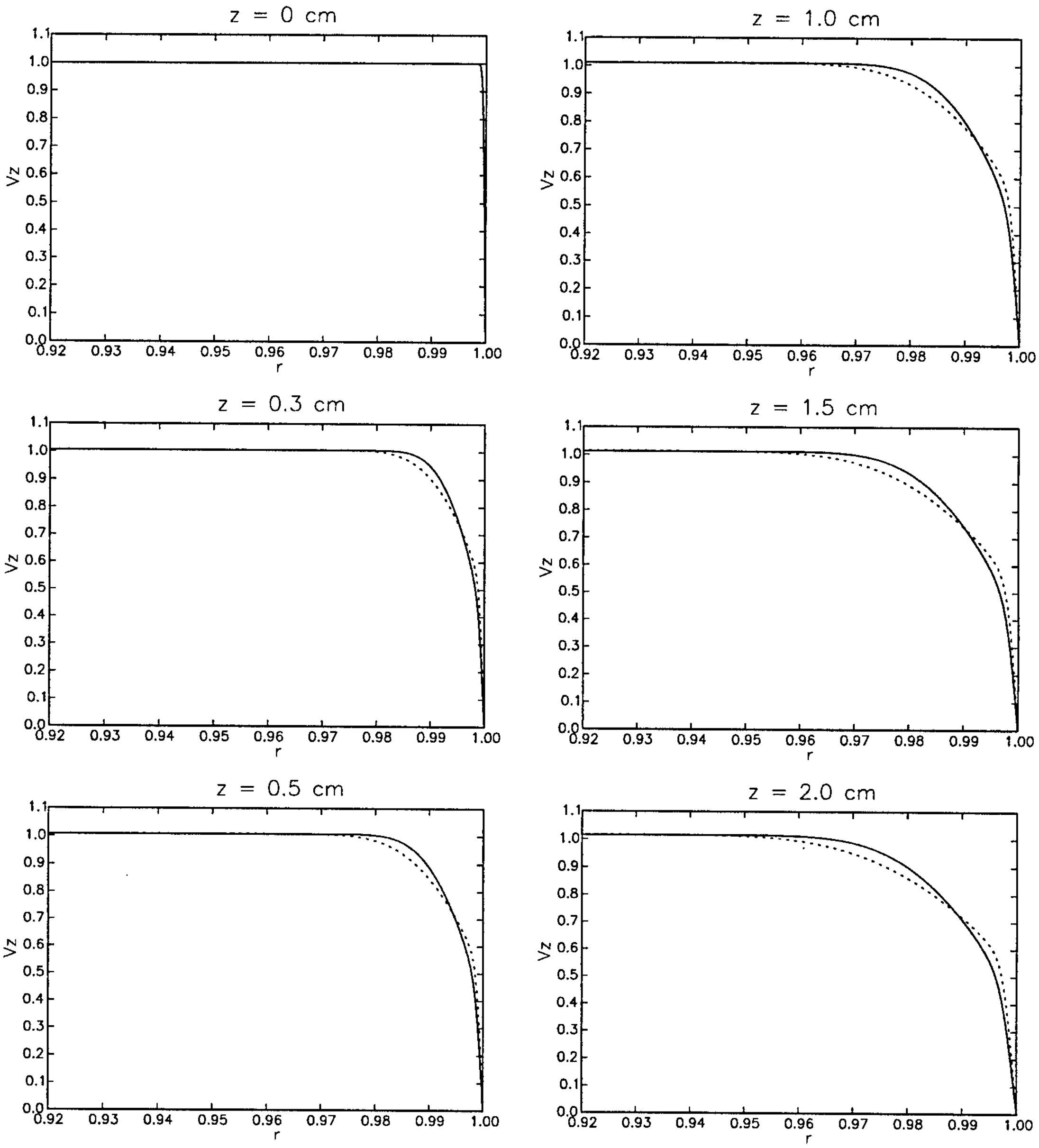
z = 0 cm

z = 1.0 cm

z = 0.3 cm

z = 1.5 cm

z = 0.5 cm

z = 2.0 cm

Figure 5.9: Steady state streamwise velocity profiles at different streamwise locations for high-speed injection of LP 1846 with $U = 300m/s$, and two different inlet temperature $T_o = 278^oK$(dashed line), and $T_o = 298^oK$ (solid line). The uniform Peclet number model is adopted, and the computations are performed using the steady parabolized approximation on a stretched grid with a stretching parameter $a = 6.5$, $N_r = 401$ points in the radial direction and $N_z = 8001$ points in the streamwise direction.

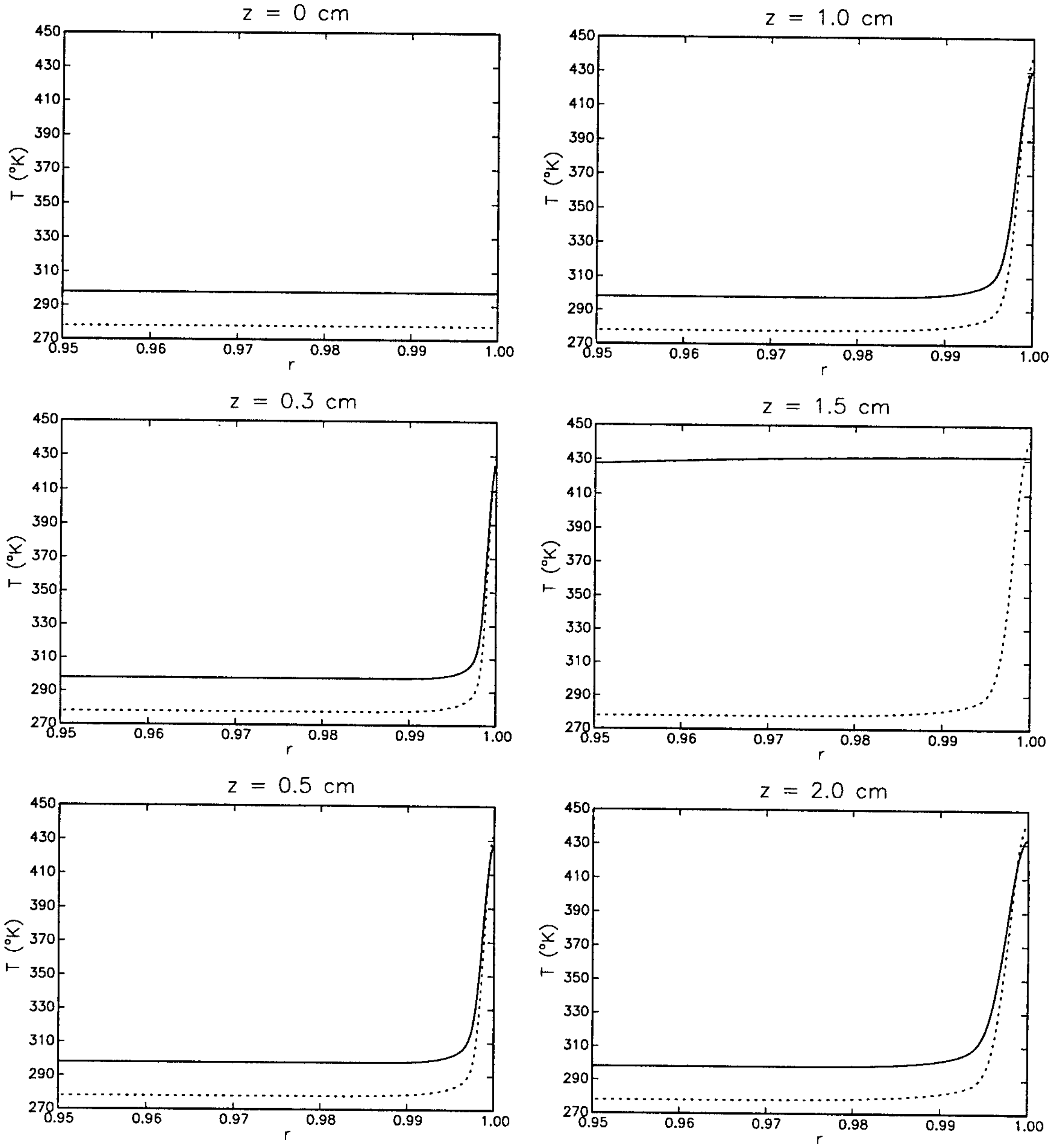

Figure 5.10: Steady state temperature profiles at different streamwise locations for high-speed injection of LP 1846 with $U = 300m/s$, and two different inlet temperature $T_o = 278^oK$(dashed line), and $T_o = 298^oK$ (solid line). The uniform Peclet number model is adopted, and the computations are performed using the steady parabolized approximation on a stretched grid with a stretching parameter $a = 6.5$, $N_r = 401$ points in the radial direction and $N_z = 8001$ points in the streamwise direction.

Chapter 6

Summary and Conclusions

Shear-induced heating of a liquid monopropellant during high-speed injection in an axisymmetric nozzle is analyzed numerically. The numerical schemes are based on a finite-difference discretization of the vorticity transport and energy equations. Steady and unsteady codes are applied to predict peak temperatures of LP1846 during high-speed short-duration injection in a nozzle having $4mm$ diameter and $2mm$ length. When adiabatic wall conditions are assumed, computed results reveal a quadratic dependence of the peak temperature on injection velocity. Significant temperature increase, of the order of $100^o K$ or more, is predicted for injection velocities higher than $200m/s$. Thus, for such injection conditions, mixture preignition is likely to occur.

Wall heat transfer, modeled in terms of a wall heat transfer coefficient, h, is also analyzed. Three values $h = 20$, 50, and $500 W/m^2.^o K$, which are representative of free convection conditions in air, forced air cooling at low speed, and forced liquid cooling at moderate speed, are selected in the analysis. When the injection speed is very high ($U > 200m/s$), wall heat transfer dies not significantly reduce peak temperature predictions even for high heat transfer coefficient. In addition, for low heat transfer coefficient, peak temperatures are close to those obtained assuming adiabatic wall conditions. Thus, free convection heat transfer does not significantly reduce the likelihood of mixture ignition. On the other hand, large values of the heat transfer coefficient may appreciably reduce peak temperatures in thin walled nozzles whenever the injection velocity is not extremely high. In these situations, forced cooling techniques may be especially tailored in order to effectively minimize the risk of mixture ignition.

The impact of a temperature-dependent viscosity is also examined. While all trends established using a constant property model are once again observed, the dependence of viscosity on temperature may significantly affect shear heating predictions. Computed results show that, for moderate injection speeds, temperature predictions of both constant and variable viscosity models are very close. However, for high injection speeds, peak temperatures obtained using a variable-viscosity model are smaller than those obtained using constant property simulation. This effect is related to the decrease of viscosity and Prandtl number with increasing temperature. Variation of the mixture inlet temperature also affects temperature predictions. In particular, it is found that shear heating effects are more pronounced for smaller inlet temperature, i.e. when the inlet Prandtl number is larger.

Finally, it is worthwhile summarizing the modeling approaches used in the present analysis and the scope of the present computations.

(1) In all multi-dimensional simulations discussed here, we have focused on laminar heating in a small-diameter high-speed nozzle. A boundary layer of vanishingly small thickness is simulated by systematically decreasing the inlet boundary layer thickness until the results become effectively indensitive to this parameter.

(2) In all cases considered, a small constant-diameter axisymmetric is assumed. The nozzle diameter and length are kept fixed, $d = 4mm$, and $R = 2mm$, respectively. Due to the short length of the nozzle, the boundary layer remains much thinner than the nozzle radius for all flow conditions analyzed above. Consequently, no significant spatial acceleration of the mixture within the potential core was observed. The potential contribution of this effect to viscous heating of the mixture should be carefully analyzed, especially if nozzles having much smaller diameter than those considered here are selected.

(3) As mentioned above, the present analysis of wall heat transfer is based on selection of a heat transfer coefficient, h. Inherently, the corresponding models assumes that the nozzle walls are very thin; therefore, their

heat storage capacity is ignored as is their contribution to the overall thermal resistance to heat flux. For thick-walled nozzles, or for nozzles embedded within large systems, the present modeling approach should be appropriately altered.

Part II

Direct Numerical Simulation of Turbulent Flow

Chapter 7

1D Solution of Turbulent Flow between Parallel Plates

As discussed in the Introduction, boundary layer transition is expected to occur for long-duration injection or when the nozzle length is large. In order to study shear heating mechanisms within a transitional or turbulent flow environment, one must first characterize the mean flow and the fluctuations around the mean flow. The objective of this chapter is to construct solutions for the mean temperature field, using well-established empirical correlations for the mean velocity field. Temperature fluctutations around the mean will be the focus of subsequent chapters.

7.1 The Mean Temperature Distribution

The starting point for determining the mean temperature distribution consists of the Reynolds-averaged equations of motion. We focus our attention on fully-developed turbulent flow in a two-dimensional channel, and assume that the channel plates have infinite extent in the streamwise $x-$ direction, and the cross-stream $z-$ direction. For steady, incompressible, constant property boundary flow, x-momentum and energy conservation equations are:

$$u\frac{\partial u}{\partial x} + v\frac{\partial u}{\partial y} = -\frac{1}{\rho}\frac{dp}{dx} + \nu\frac{\partial^2 u}{\partial y^2} \tag{7.1}$$

$$\rho c_p(u\frac{\partial T}{\partial x} + v\frac{\partial T}{\partial y}) = k\nabla^2 T + \Phi \tag{7.2}$$

where, u and v are the velocity components in the x and y directions, respectively, p is pressure, ρ is density, c_p is the specific heat at constant pressure, k is the thermal conductivity, T is temperature, and Φ is the viscous dissipation function.

By taking the time average of the energy conservation equation, we obtain the following governing equation for the mean temperature profile in a fully-developed turbulent channel flow:

$$\rho c_p\left(\overline{u}\frac{\partial\overline{T}}{\partial x} + \overline{v}\frac{\partial\overline{T}}{\partial y}\right) = -\frac{\partial q_t}{\partial y} + \tau_t\frac{\partial\overline{u}}{\partial y} \tag{7.3}$$

Here, τ_t denotes the total shear stress while q_t represents the total heat flux. q_t and τ_t are respectively given by:

$$\tau_t = \mu\frac{\partial\overline{u}}{\partial y} - \rho\overline{u'v'}$$

$$q_t = -\left(k\frac{\partial\overline{T}}{\partial y} - \rho c_p\overline{v'T'}\right)$$

and consist of contributions due to molecular diffusion and turbulent mixing.

Next, we invoke the Boussinesq analogy for eddy viscosity and eddy conductivity. We thus have:

$$\tau_t = (\mu + \mu_t)\frac{\partial \overline{u}}{\partial y}$$

$$q_t = -(k + k_t)\frac{\partial \overline{T}}{\partial y}$$

Here, neither μ_t and k_t is a property of a fluid; their ratio defines a dimensionless group, the turbulent Prandtl number:

$$Pr_t = \frac{c_p \mu_t}{k_t}$$

Note that Pr_t is of order unity. In all our calculations, Pr_t is taken to be 0.9.

Substituting the Boussinesq analogy into the mean energy equation, we obtain:

$$\rho c_p \left(\overline{u}\frac{\partial \overline{T}}{\partial x} + \overline{v}\frac{\partial \overline{T}}{\partial y}\right) = (\mu + \mu_t)\left(\frac{\partial \overline{u}}{\partial y}\right)^2 + \frac{\partial}{\partial y}\left((k + k_t)\frac{\partial \overline{T}}{\partial y}\right) \tag{7.4}$$

Since $\partial \overline{T}/\partial x = 0$ and $\overline{v} = 0$ for fully-developed flow, the above equation reduces to:

$$\frac{\partial}{\partial y}\left((k + k_t)\frac{\partial \overline{T}}{\partial y}\right) = -(\mu + \mu_t)\left(\frac{\partial \overline{u}}{\partial y}\right)^2 \tag{7.5}$$

Recall that,

$$\mu + \mu_t = \mu(1 + \epsilon_M/\nu)$$

$$k + k_t = k(1 + \epsilon_H/\alpha)$$

where ϵ_M is the eddy diffusivity for momentum transfer, while ϵ_H is the eddy diffusivity for heat transfer. They are respectively defined by the following expressions:

$$\rho\epsilon_M \frac{\partial \overline{u}}{\partial y} \equiv -\rho\overline{u'v'}$$

$$\epsilon_H \frac{\partial T}{\partial y} \equiv -\overline{v'T'}$$

Substituting the above relationships into the time-averaged energy equation, we get:

$$\frac{\partial}{\partial y}\left((\alpha + \epsilon_H)\frac{\partial \overline{T}}{\partial y}\right) = -\frac{\mu}{\rho c_p}(1 + \epsilon_M/\nu)\left(\frac{\partial \overline{u}}{\partial y}\right)^2 \tag{7.6}$$

The temperature boundary conditions are:

$$\begin{cases} \frac{\partial \overline{T}}{\partial y}|_{y=y_c} = 0 \\ \overline{T}|_{y=0} = T_w \end{cases} \tag{7.7}$$

Integrating the energy equation once with respect to y, we have

$$(\alpha + \epsilon_H)\frac{\partial \overline{T}}{\partial y} + \frac{q_w}{\rho c_p} = -\frac{\mu}{\rho c_p}\int_0^y (1 + \epsilon_M/\nu)\left(\frac{\partial \overline{u}}{\partial y}\right)^2 dy \tag{7.8}$$

where q_w is the heat flux at the wall, which is determined from a global energy conservation constraint. Integrating the energy equation from the wall to the center line, we get:

$$q_w = -\int_0^{y_c} \mu(1 + \epsilon_M/\nu)\left(\frac{\partial \overline{u}}{\partial y}\right)^2 dy \tag{7.9}$$

Integrating the energy equation twice with respect to y, we have

$$\begin{aligned}\overline{T}-T_w = & -\frac{q_w}{\rho c_p}\int_0^y \frac{1}{\alpha+\epsilon_H}dy \\ & -\frac{\mu}{\rho c_p}\int_0^y \frac{1}{\alpha+\epsilon_H}\left(\int_0^{y_1}(1+\epsilon_M/\nu)\left(\frac{\partial\overline{u}}{\partial y_2}\right)^2 dy_2\right)dy_1\end{aligned} \quad (7.10)$$

The above expression is normalized by introducing friction velocity

$$u_* \equiv \sqrt{\tau_w/\rho}$$

where τ_w is the wall shear stress, and defining the following dimensionless groups,

$$\begin{aligned}u^+ &= \frac{\overline{u}}{u_*}\\ y^+ &= \frac{y u_*}{\nu}\\ T^+ &= \frac{(T_w-\overline{T})u_*}{q_w/(\rho c_p)}\end{aligned}$$

Using this normalization convention, the non-dimensional temperature distribution is given by:

$$\begin{aligned}T^+ = & \int_0^{y^+}\frac{1}{\frac{1}{Pr}+\frac{1}{Pr_t}\frac{\epsilon_M}{\nu}}dy^+ + \frac{\rho u_*^3}{q_w} \\ \times & \int_0^{y^+}\frac{1}{\frac{1}{Pr}+\frac{1}{Pr_t}\frac{\epsilon_M}{\nu}}\left(\int_0^{y^+}(1+\epsilon_M/\nu)\left(\frac{\partial u^+}{\partial y^+}\right)^2 dy^+\right)dy^+\end{aligned} \quad (7.11)$$

where,

$$\frac{q_w}{\rho u_*^3} = -\int_0^{y_c^+}(1+\epsilon_M/\nu)\left(\frac{\partial u^+}{\partial y^+}\right)^2 dy^+ \quad (7.12)$$

In oder to solve the above equation, we need to estimate the value of ϵ_M/ν, which depends on the mean velocity profile. For simplicity, a two-layer model for the mean velocity distribution is used. In this model, the turbulent boundary layer consists of two distinct regions: a viscous sublayer, in which $\nu \gg \epsilon_M$, and a fully turbulent region, where $\epsilon_M \gg \nu$. In the viscous sublayer, the mean velocity is given by:

$$u^+ = y^+ \tag{7.13}$$

while in the outer layer the velocity profile follows (Kays and Crawford 1980):

$$u^+ = 2.5 \ln \left(y^+ \frac{1.5[1 + (h - y)/h]}{1 + 2[(h - y)/h]^2} \right) + 5.5 \tag{7.14}$$

Note that the outer layer approaches

$$u^+ = 2.5 \ln y^+ + 5.5 \tag{7.15}$$

near the wall, and it has zero slope at the center line, i.e. at $y = h$. The critical value of y^+ for the two-layer model is taken to be 12 in our calculations.

Next, the value of ϵ_M/ν in the viscous sublayer is evaluated by incorporating the Prandtl mixing length model

$$\epsilon_M = l^2 \left| \frac{\partial \overline{u}}{\partial y} \right|$$

with the Van Driest proposition,

$$l = \kappa y [1 - \exp(-y^+/A^+)]$$

where constant A^+ is an emperically-determined effective sublayer thickness. In our calculations, A^+ is taken to be 25.0 (Kays and Crawford 1980). The resulting expression of ϵ_M/ν in the viscous sublayer is:

$$\epsilon_M/\nu = (\kappa y^+)^2 \left(1 - \frac{1}{\exp(y^+/A^+)} \right)^2 \tag{7.16}$$

Note that the expression of ϵ_M/ν in the sublayer is based on the mixing length model. In the region toward the centerline of the channel the assumption of a constant mixing length, which is recommended for the external boundary layers, is no longer appropriate. Thus, we rely on the empirical equation proposed by Riechardt, which is valid for the entire region outside of the viscous sublayer,

$$\epsilon_M/\nu = \frac{\kappa y^+}{6}(1 + \frac{h-y}{h})[1 + 2(\frac{h-y}{h})^2] \tag{7.17}$$

Here, h denotes the distance between the plate and central line. Using the empirical correlations u^+ and ϵ_M, the temperature profile is determined by numerically evaluating the integral on the right-hand side of Eq. (7.11).

7.2 Results and Discussion

The mean temperature profile for a fully-developed flow in 2D channel of half-depth $h = 2$mm, with friction velocity $u^* = 11$ m/s and kinematic viscosity $\nu = 5 \times 10^{-6} m^2/s$ are obtained using the approach of the previous section. The corresponding mean velocity $\overline{u}$ at the center line is about $300 m/s$, and y^+ ranges from 0 to 4400. The results are depicted in Figs. (7.1-7.4).

Fig. 7.1 shows the two-layer model mean velocity profile in the range of $0 \leq y^+ \leq 4400$. Note that the velocity gradient at the center line ($y^+ = 4400$) is zero, as required by the symmetry of the velocity profile across the channel. In Fig. 7.2, the comparison of turbulent and laminar parabolic profiles for the same mean velocity is made. The velocities are normalized with the maximum velocity at the center line.

The temperature variations for different Prandtl numbers are plotted in Fig 7.3. Note that, the discontinuity of $\frac{dT^+}{dy^+}$ at $y^+ = 12$ is due to the discontinuity of $\frac{dU^+}{dy^+}$ at $y^+ = 12$, and the fact that the estimates of ϵ/nu is also dependent $\frac{dU^+}{dy^+}$. Since the constant wall temperature boundary condition is used in the calculation, the wall tempearuture keeps unchanged, and the highest temperature occurs near to the wall due to the higher heat generation there.

Finally, the computed temperature profile is compared in Fig. 7.4 with that of laminar entrance flow. The plots indicated that a higher peak temperature is predicted for fully-developed turbulent flow, and this effect is attributed to the fact that, in the turbulent flow region, the viscous sublayer is spatially uniform and has a thickness which is significantly smaller than that of the laminar boundary layer in the entrance region.

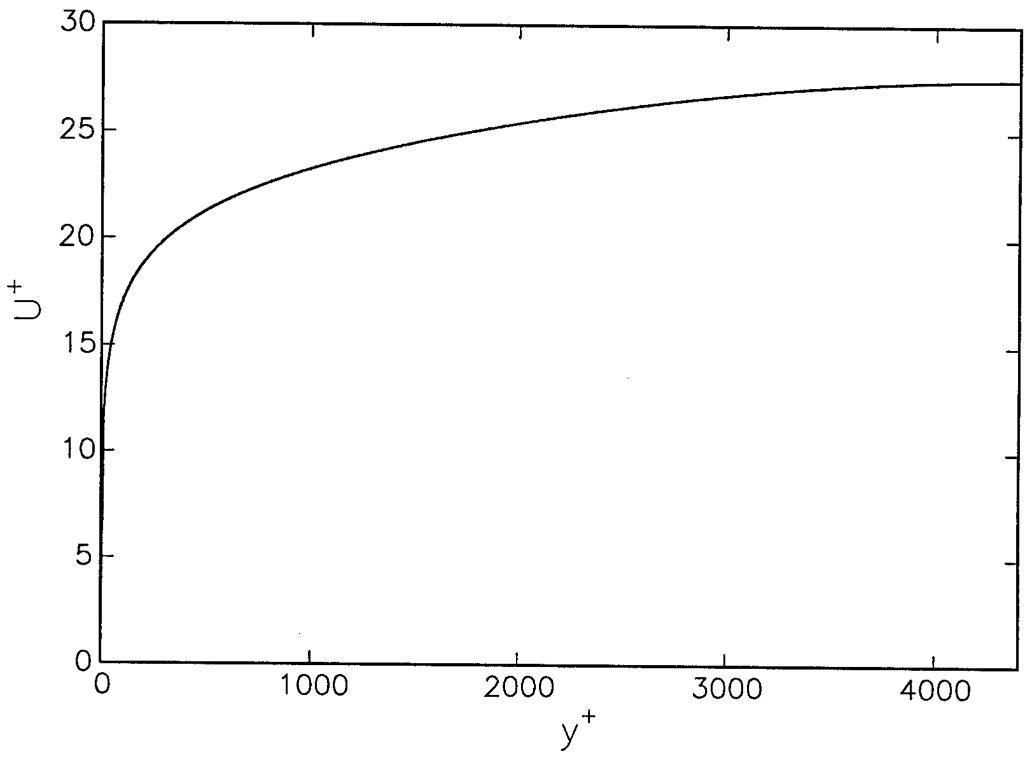

Figure 7.1: Turbulent mean velocity distribution in wall coordinates. The calculation is performed with maximum mean velocity $\overline{u}_{max} = 300m/s$, half channel depth $h = 2mm$, viscosity $\nu = 5.0e^{-6}$.

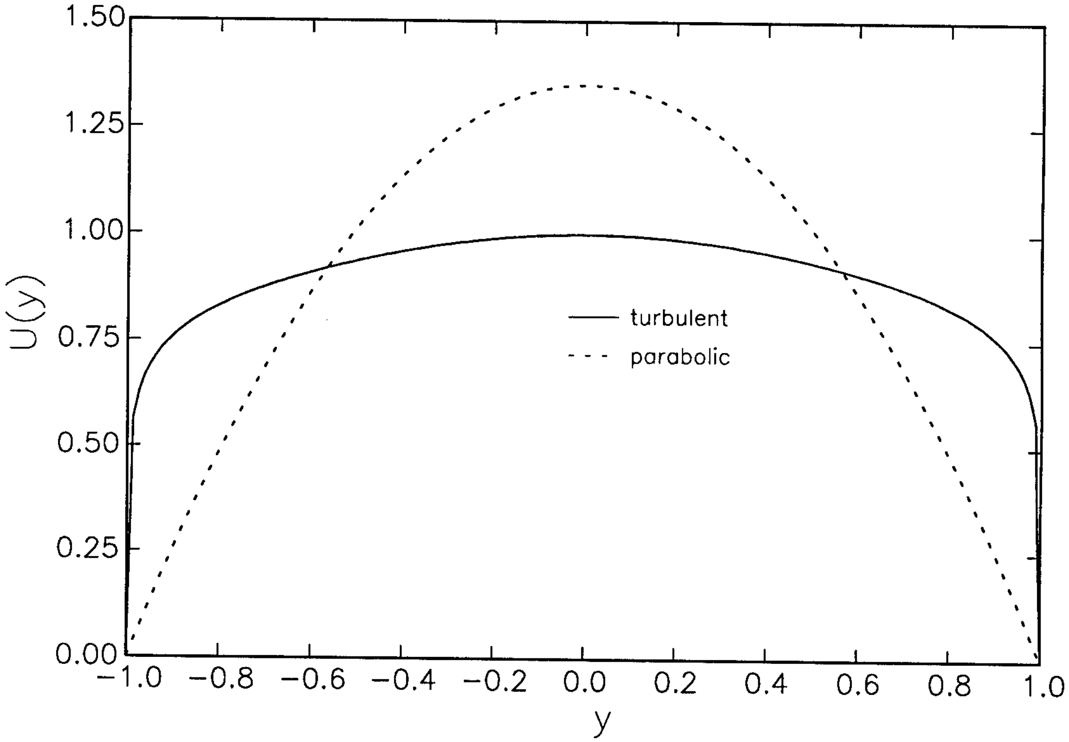

Figure 7.2: Comparison of turbulent and laminar parabolic profiles for the same mean velocity. The velocities are normalized with the maximum turbulent velocity at the center line. The turbulent velocity profile is computed with maximum mean velocity $\overline{u}_{max} = 300m/s$, half channel depth $h = 2mm$, viscosity $\nu = 5.e^{-6}$.

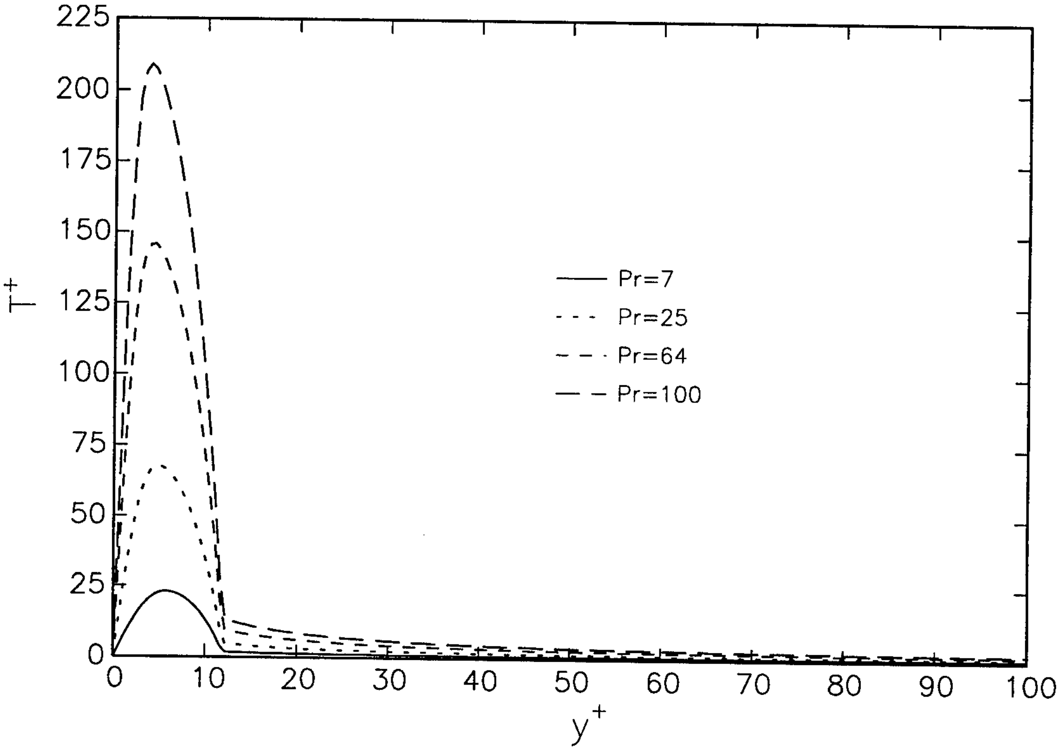

Figure 7.3: Turbulent mean temperature profile with four different Prandtl numbers, 7, 25, 64 and 100 in wall coordinates and constant wall temperature condition. The calculations are performed with maximum mean velocity $\overline{u}_{max} = 300m/s$, half channel depth $h = 2mm$, and viscosity $\nu = 5.e^{-6}$.

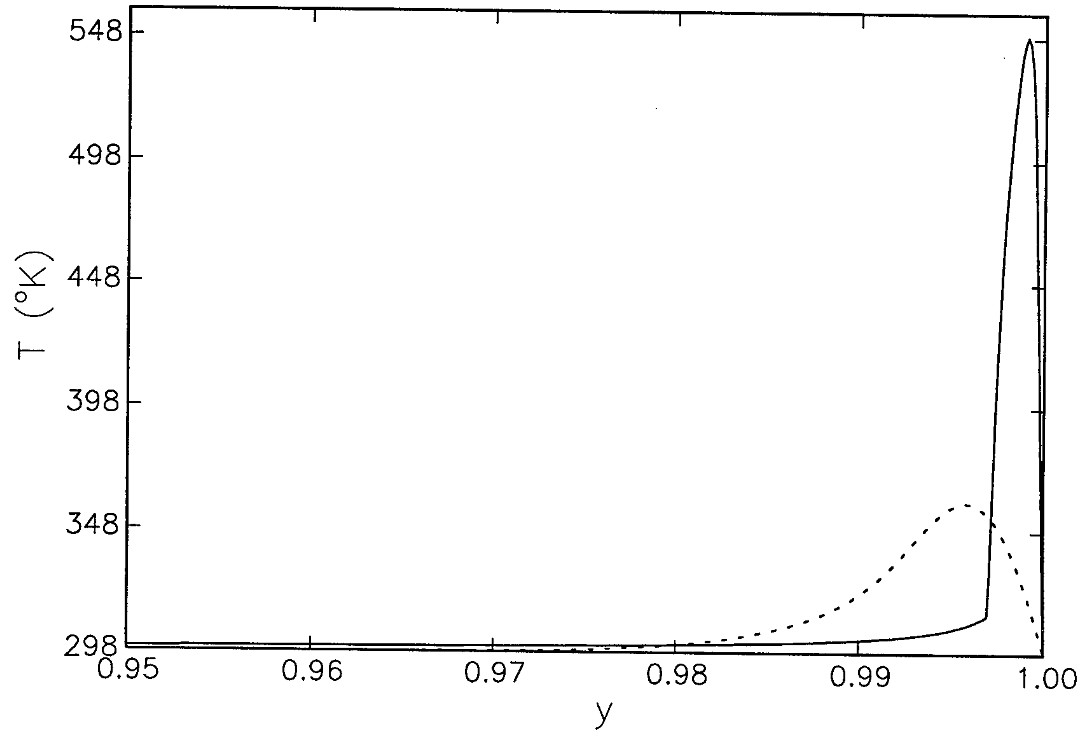

Figure 7.4: Dimensional turbulent mean temperature profile (maximum mean velocity $\overline{u}_{max} = 300m/s$) and laminar entrance temperature profile (maximum velocity is $300m/s$) with $Pr = 109$, half channel depth $h = 2mm$, and viscosity $\nu = 5.e^{-6}$. Also, constant wall temperature condition is imposed at both cases.

Chapter 8

Homogeneous Isotropic Turbulence

8.1 Introduction

As discussed earlier, characterization of the effects of shear-induced heating in transitional/turbulent flows necessitates a study of unsteady temperature fluctuations around their mean values. In the present chapter, estimates are obtained for the simplified case of a statistically-steady homogeneous isotropic turbulent field. The primary motivation behind the present exercise is to derive approximate estimates for the amplitude of spatial temperature fluctuations, and to gain insight into the phenomena which govern their behavior. To this end, we shall select high values for the kinetic energy dissipation rate which are characteristic of high-speed flows in thin channels. The evolution of the isotropic velocity and temperature distributions will be computed using direct numerical simulation of the vorticity transport and energy equations. The results will then be contrasted in the following chapter with simulations of turbulent channel flow.

8.2 Formulation

We assume an incompressible, constant-density fluid with constant properties. The motion of the fluid is governed by the conservation equations for mass, momentum and energy. In a vorticity-based formulation, the governing equations are expressed as:

$$\frac{\partial \vec{\omega}}{\partial t} + \nabla \times (\vec{\omega} \times \vec{u}) = \nu \nabla^2 \vec{\omega} + \nabla \times \vec{f} \tag{8.1}$$

$$\nabla^2 \vec{u} = -\nabla \times \vec{\omega} \tag{8.2}$$

$$\rho c_p \frac{DT}{Dt} = k \nabla^2 T + \mu \Phi \tag{8.3}$$

where $\vec{u}$ is the velocity vector, $\vec{\omega}$ is the vorticity, T is temperature, ρ is density, t is time, $\vec{f}$ is the force acting on the fluid, c_p is specific heat at constant pressure, k is the thermal conductivity, ν is the kinematic viscosity, μ is the dynamic viscosity, $\frac{D}{Dt} \equiv \frac{\partial}{\partial t} + \vec{u} \cdot \nabla$ is the material derivative, and Φ is viscous dissipation function. The above vorticity-velocity formulation has become, to a growing number of people, an attractive alternative to formualtions in primitive variables. This interest (Guevremont et al. 1990; Gresho 1991) is mainly linked to easier treatment of boundary conditions since the pressure is no longer part of the solution.

Let $\vec{b} = \nabla \times \vec{f}$, $\vec{f} = (f_1, f_2, f_3)$, $\vec{b} = (b_1, b_2, b_3)$ in a Cartesian coordinate system $(x, y, z) = (x_1, x_2, x_3)$. In component form, the vorticity forcing term is given by:

$$
\begin{aligned}
b_1 &= \frac{\partial f_3}{\partial y} - \frac{\partial f_2}{\partial z} \\
b_2 &= \frac{\partial f_1}{\partial z} - \frac{\partial f_3}{\partial x} \\
b_3 &= \frac{\partial f_2}{\partial x} - \frac{\partial f_1}{\partial y}
\end{aligned}
$$

and the governing equations are expressed as:

$$\frac{\partial \omega_1}{\partial t} + \frac{\partial s_3}{\partial y} - \frac{\partial s_2}{\partial z} = \nu \nabla^2 \omega_1 + b1 \tag{8.4}$$

$$\frac{\partial \omega_2}{\partial t} + \frac{\partial s_1}{\partial z} - \frac{\partial s_3}{\partial x} = \nu \nabla^2 \omega_2 + b2 \tag{8.5}$$

$$\frac{\partial \omega_3}{\partial t} + \frac{\partial s_2}{\partial x} - \frac{\partial s_1}{\partial y} = \nu \nabla^2 \omega_3 + b3 \tag{8.6}$$

$$\nabla^2 u_1 = \frac{\partial \omega_2}{\partial z} - \frac{\partial \omega_3}{\partial y} \tag{8.7}$$

$$\nabla^2 u_2 = \frac{\partial \omega_3}{\partial x} - \frac{\partial \omega_1}{\partial z} \tag{8.8}$$

$$\nabla^2 u_3 = \frac{\partial \omega_1}{\partial y} - \frac{\partial \omega_2}{\partial x} \tag{8.9}$$

$$\frac{\partial T}{\partial t} + \frac{\partial (u_1 T)}{\partial x} + \frac{\partial (u_2 T)}{\partial y} + \frac{\partial (u_3 T)}{\partial z} = \alpha \nabla^2 T + \frac{\nu}{c_p} \Phi \tag{8.10}$$

Here,

$$s_1 \equiv u_3 \omega_2 - u_2 \omega_3$$

$$s_2 \equiv u_1 \omega_3 - u_3 \omega_1$$

$$s_3 \equiv u_2 \omega_1 - u_1 \omega_2$$

and the viscous dissipation function Φ is given by:

$$\Phi \equiv 2 \left[(\frac{\partial u_1}{\partial x})^2 + (\frac{\partial u_2}{\partial y})^2 + (\frac{\partial u_3}{\partial z})^2 \right] \tag{8.11}$$

$$+ \quad \left(\frac{\partial u_1}{\partial y} + \frac{\partial u_2}{\partial x}\right)^2 + \left(\frac{\partial u_1}{\partial z} + \frac{\partial u_3}{\partial x}\right)^2 + \left(\frac{\partial u_2}{\partial z} + \frac{\partial u_3}{\partial y}\right)^2$$

For a statistically-steady, isotropic turbulent flow, we further assume that periodic boundary conditions hold along the coordinate directions for the velocity, vorticity, and temperature fields. Thus, these variables admit a Fourier representation in terms of the coordinate variables x, y and z. In Fourier space, the governing equations take the following form:

$$(\frac{\partial}{\partial t} + \nu| \vec{k} |^2)\hat{\omega}_1 = ik_z\hat{s}_2 - ik_y\hat{s}_3 + \hat{b}_1 \tag{8.12}$$

$$(\frac{\partial}{\partial t} + \nu| \vec{k} |^2)\hat{\omega}_2 = ik_x\hat{s}_3 - ik_z\hat{s}_1 + \hat{b}_2 \tag{8.13}$$

$$(\frac{\partial}{\partial t} + \nu| \vec{k} |^2)\hat{\omega}_3 = ik_y\hat{s}_1 - ik_x\hat{s}_2 + \hat{b}_3 \tag{8.14}$$

$$| \vec{k} |^2\hat{u}_1 = ik_z\hat{\omega}_2 - ik_y\hat{\omega}_3 \tag{8.15}$$

$$| \vec{k} |^2\hat{u}_2 = ik_x\hat{\omega}_3 - ik_z\hat{\omega}_1 \tag{8.16}$$

$$| \vec{k} |^2\hat{u}_3 = ik_y\hat{\omega}_1 - ik_x\hat{\omega}_2 \tag{8.17}$$

$$(\frac{\partial}{\partial t} + \alpha| \vec{k} |^2)\hat{T} + ik_x\widehat{u_1T} + ik_y\widehat{u_2T} + ik_z\widehat{u_3T} = \frac{\nu}{c_p}\hat{\Phi} \tag{8.18}$$

where, $\vec{k} = (k_x, k_y, k_z)$ is the wavenumber vector, and

$$\left|\vec{k}\right| = \sqrt{k_x^2 + k_y^2 + k_z^2} \tag{8.19}$$

is the modulus of $| \vec{k} |$.

8.3 Numerical Schemes

Flowfield simulation is performed using a pseudo-spectral formulation of the governing equations. Briefly, the evolution of the Fourier coefficients for vorticity and temperature are computed by approximating non-linear source terms using spectral collocation derivatives and numerically integrating the resulting equations.

In the numerical implementation, we start with the vorticity transport equation. We rely on factorization of the viscous diffusion term, and recast the equations of motion of the Fourier coefficients of vorticity as:

$$\frac{\partial}{\partial t}(e^{\nu|\vec{k}|^2 t}\widehat{\omega_1}) = e^{\nu|\vec{k}|^2 t}(ik_z\widehat{s_2} - ik_y\widehat{s_3} + \widehat{b_1}) \tag{8.20}$$

$$\frac{\partial}{\partial t}(e^{\nu|\vec{k}|^2 t}\widehat{\omega_2}) = e^{\nu|\vec{k}|^2 t}(ik_x\widehat{s_3} - ik_z\widehat{s_1} + \widehat{b_2}) \tag{8.21}$$

$$\frac{\partial}{\partial t}(e^{\nu|\vec{k}|^2 t}\widehat{\omega_3}) = e^{\nu|\vec{k}|^2 t}(ik_y\widehat{s_1} - ik_x\widehat{s_2} + \widehat{b_3}) \tag{8.22}$$

The Fourier coefficients $\widehat{s_1}$, $\widehat{s_2}$, and $\widehat{s_3}$ are approximated using spectral collocation derivatives and the discrete system is integrated using the second-order Adams-Bashforth scheme. The resulting discrete evolution equations are:

$$\begin{aligned}
\frac{\widehat{\omega_1}^{n+1} - e^{-\nu|\vec{k}|^2\Delta t}\widehat{\omega_1}^{n}}{\Delta t} &= \sum_{j=0}^{1}\beta_j e^{-\nu|\vec{k}|^2(j+1)\Delta t}(ik_z\widehat{s_2}^{n-j} \\
&- ik_y\widehat{s_3}^{n-j}) + e^{-\nu|\vec{k}|^2\Delta t}\widehat{b_1} && (8.23) \\
\frac{\widehat{\omega_2}^{n+1} - e^{-\nu|\vec{k}|^2\Delta t}\widehat{\omega_2}^{n}}{\Delta t} &= \sum_{j=0}^{1}\beta_j e^{-\nu|\vec{k}|^2(j+1)\Delta t}(ik_x\widehat{s_3}^{n-j} \\
&- ik_z\widehat{s_1}^{n-j}) + e^{-\nu|\vec{k}|^2\Delta t}\widehat{b_2} && (8.24) \\
\frac{\widehat{\omega_3}^{n+1} - e^{-\nu|\vec{k}|^2\Delta t}\widehat{\omega_3}^{n}}{\Delta t} &= \sum_{j=0}^{1}\beta_j e^{-\nu|\vec{k}|^2(j+1)\Delta t}(ik_y\widehat{s_1}^{n-j} \\
&- ik_x\widehat{s_2}^{n-j}) + e^{-\nu|\vec{k}|^2\Delta t}\widehat{b_3} && (8.25)
\end{aligned}$$

In equations (8.23-8.25), $i = \sqrt{-1}$, $\beta_0 = 3/2$, $\beta_1 = -1/2$, and Δt is time step.

Recall that the Fourier transform of $f(x)$ is defined by:

$$F_x[f(x)] = F(\xi) = \frac{1}{\sqrt{2\pi}} \int_{-\infty}^{+\infty} f(x) e^{-i\xi x} dx \tag{8.26}$$

and that the inverse Fourier transform of $F(\xi)$ is given by:

$$f(x) = F_x^{-1}[F(\xi)] = \frac{1}{\sqrt{2\pi}} \int_{-\infty}^{+\infty} F(\xi) e^{i\xi x} d\xi \tag{8.27}$$

where F_x and F_x^{-1} denote the forward and inverse Fourier transforms, respectively. By considering terms of the form $F_x^{-1}[e^{-a\xi^2} F_x[f(x)]]$, where a is a positive number, it is easy to verify using the definitions of F_x and F_x^{-1} that if the function $f(x)$ is real-valued then this is also the case for $F_x^{-1}[e^{-a\xi^2} F_x[f(x)]]$. A similar observation also holds for terms of the form $F_x^{-1}[i\xi e^{-a\xi^2} F_x[f(x)]]$.

In the computations, we take advantage of the above observations, and also exploit the linearity of Fourier operators and the fact that transforms and inverse transforms along different coordinate directions commute. By doing so, we arrive at the following discrete system of evolution equations:

$$\begin{aligned}
\omega_1^{n+1} &= (F_x^{-1} e^{-\nu k_x^2 \Delta t} F_x)(F_y^{-1} e^{-\nu k_y^2 \Delta t} F_y)(F_z^{-1} e^{-\nu k_z^2 \Delta t} F_z)\omega_1^n + \sum_{j=0}^{1} \Delta t \beta_j \\
&\times [(F_x^{-1} e^{-\nu k_x^2 \Delta t} F_x)(F_y^{-1} e^{-\nu k_y^2 \Delta t} F_y)(F_z^{-1} e^{-\nu k_z^2 \Delta t} i k_z F_z) s_2^{n-j} \\
&- (F_x^{-1} e^{-\nu k_x^2 \Delta t} F_x)(F_y^{-1} e^{-\nu k_y^2 \Delta t} i k_y F_y)(F_z^{-1} e^{-\nu k_z^2 \Delta t} F_z) s_3^{n-j}] \\
&+ \Delta t (F_x^{-1} e^{-\nu k_x^2 \Delta t} F_x)(F_y^{-1} e^{-\nu k_y^2 \Delta t} F_y)(F_z^{-1} e^{-\nu k_z^2 \Delta t} F_z) b_1
\end{aligned} \tag{8.28}$$

$$\begin{aligned}
\omega_2^{n+1} &= (F_x^{-1} e^{-\nu k_x^2 \Delta t} F_x)(F_y^{-1} e^{-\nu k_y^2 \Delta t} F_y)(F_z^{-1} e^{-\nu k_z^2 \Delta t} F_z)\omega_2^n + \sum_{j=0}^{1} \Delta t \beta_j \\
[& (F_x^{-1} e^{-\nu k_x^2 \Delta t} i k_x F_x)(F_y^{-1} e^{-\nu k_y^2 \Delta t} F_y)(F_z^{-1} e^{-\nu k_z^2 \Delta t} F_z) s_3^{n-j} \\
- & (F_x^{-1} e^{-\nu k_x^2 \Delta t} F_x)(F_y^{-1} e^{-\nu k_y^2 \Delta t} F_y)(F_z^{-1} e^{-\nu k_z^2 \Delta t} i k_z F_z) s_1^{n-j}] \\
+ & \Delta t (F_x^{-1} e^{-\nu k_x^2 \Delta t} F_x)(F_y^{-1} e^{-\nu k_y^2 \Delta t} F_y)(F_z^{-1} e^{-\nu k_z^2 \Delta t} F_z) b_2 \qquad (8.29)
\end{aligned}$$

$$\begin{aligned}
\omega_3^{n+1} &= (F_x^{-1} e^{-\nu k_x^2 \Delta t} F_x)(F_y^{-1} e^{-\nu k_y^2 \Delta t} F_y)(F_z^{-1} e^{-\nu k_z^2 \Delta t} F_z)\omega_3^n + \sum_{j=0}^{1} \Delta t \beta_j \\
[& (F_x^{-1} e^{-\nu k_x^2 \Delta t} F_x)(F_y^{-1} e^{-\nu k_y^2 \Delta t} i k_y F_y)(F_z^{-1} e^{-\nu k_z^2 \Delta t} F_z) s_1^{n-j} \\
- & (F_x^{-1} e^{-\nu k_x^2 \Delta t} i k_x F_x)(F_y^{-1} e^{-\nu k_y^2 \Delta t} F_y)(F_z^{-1} e^{-\nu k_z^2 \Delta t} F_z) s_2^{n-j}] \\
+ & \Delta t (F_x^{-1} e^{-\nu k_x^2 \Delta t} F_x)(F_y^{-1} e^{-\nu k_y^2 \Delta t} F_y)(F_z^{-1} e^{-\nu k_z^2 \Delta t} F_z) b_3 \qquad (8.30)
\end{aligned}$$

The advantage of the above system is that it yields the discrete evolution of the vorticity field in physical space using a spectral collocation scheme which involves real Fourier transforms only. This simplifies the numerical implementation and results in significant computational savings over complex FFTs.

Once the vorticity field is updated, Eq. (8.2) is inverted in order to determine the velocity field. In the computations, we first consider the velocity components u_1 and u_2, as well as the combination,

$$u_c \equiv u_1 + i u_2 \qquad (8.31)$$

Based on the updated values of ω_1, ω_2, ω_3, we form the source terms

$$r_1 \equiv \frac{\partial \omega_2}{\partial z} - \frac{\partial \omega_3}{\partial y}$$

$$r_2 \equiv \frac{\partial \omega_3}{\partial x} - \frac{\partial \omega_1}{\partial z}$$

using spectral collocation derivatives, and define the combination,

$$r_c \equiv r_1 + i r_2 \tag{8.32}$$

Using Eqs. (8.15) and (8.16), the Fourier transform of u_c is determined from:

$$\widehat{u_c}(\vec{k}) = -\frac{1}{\left|\vec{k}\right|^2}\widehat{r_c}(\vec{k}) \qquad \vec{k} \neq 0 \tag{8.33}$$

with $\widehat{u_c} = 0$ for $\vec{k} = 0$. The components u_1 and u_2 are then solved together by inverting Eq. (8.33), at the cost of one complex FFT.

Once u_1 and u_2 are determined, the velocity component u_3 is obtained by using continuity equation and the definition of vorticity, $\vec{\omega} \equiv \nabla \times \vec{u}$. In Cartesian coordinates, we have:

$$\omega_1 = \frac{\partial u_3}{\partial y} - \frac{\partial u_2}{\partial z} \tag{8.34}$$

$$\omega_2 = \frac{\partial u_1}{\partial z} - \frac{\partial u_3}{\partial x} \tag{8.35}$$

$$\omega_3 = \frac{\partial u_2}{\partial x} - \frac{\partial u_1}{\partial y} \tag{8.36}$$

From u_1 and ω_2, we find $\frac{\partial u_3}{\partial x}$ using Eq. (8.35), and its Fourier transform with respect to x. Suppose that $\widehat{\frac{\partial u_3}{\partial x}} = \hat{a}_r + i\hat{a}_i$, and $\widehat{u_3} = \widehat{u_3}_r + i\widehat{u_3}_i$, then $ik_x\widehat{u_3} = \hat{a}_r + i\hat{a}_i$. When $k_x \neq 0$, $\widehat{u_3}$ can be obtained through the spectrum of $\frac{\partial u_3}{\partial x}$. Assuming u_3 vanishes at $(0,0,0)$, we have from the definition of the Fourier transform:

$$u_3(0,0,0) = \sum_{k_x=-N/2}^{N/2-1} \widehat{u_3}(k_x, 0, 0) \tag{8.37}$$

Note that for 1-D real FFT, the real part of the Fourier coefficients is symmetric with respect to wave number, while the imaginary part of the coefficients is antisymmetric with respect to wave number, i.e. $R_e(\widehat{u_3}(k_x, 0, 0)) = R_e(\widehat{u_3}(-k_x, 0, 0))$, $I_m(\widehat{u_3}(k_x, 0, 0)) = -\widehat{u_3}(-k_x, 0, 0)$. Thus, the above expression reduces to

$$\widehat{u_3}(0, 0, 0) = -2 \sum_{k_x=1}^{N/2-1} Re(\widehat{u_3}(k_x, 0, 0)) \tag{8.38}$$

and one inverse FFT will yield $u_3(x, 0, 0)$, i.e velocity component u_3 along the x-axis.

Next, from $u_3(x, 0, 0)$, we can solve for $u_3(x, y, 0)$, i.e the value of u_3 in the x-y plane. We now form $\frac{\partial u_3}{\partial y}$ using Eq. (8.34), and its Fourier transform with respect to y to obtain an expression of the form, $\widehat{\frac{\partial u_3}{\partial y}} = \hat{b}_r + i\hat{b}_i$. Then, $\widehat{u_3} = b_i/k_y + ib_r/k_y$ if $k_y \neq 0$. The coefficient of the zeroth mode is determined using the definition of the Fourier transform; we have:

$$u_3(x, 0, 0) = \sum_{k_y=-N/2}^{N/2-1} \widehat{u_3}(x, k_y, 0) \tag{8.39}$$

Taking advantage of the conjugate properties of the Fourier coefficients, we obtain:

$$\widehat{u_3}(x, k_y = 0, 0) = u_3(x, y = 0, z = 0) - 2 \sum_{k_y=1}^{N/2-1} \widehat{u_3}(x, k_y, 0) \tag{8.40}$$

where $u_3(x, 0, 0)$ is known from the previous step. Then, the inverse FFT will give the value of u_3 in x-y plane.

Finally, we consider the continuity equation to compute

$$\frac{\partial u_3}{\partial z} = -\left(\frac{\partial u_1}{\partial x} + \frac{\partial u_2}{\partial y}\right) \tag{8.41}$$

and apply a similar procedure to that of the previous two steps in order to determine the Fourier coefficients $\widehat{u_3}(x, y, k_z)$. The complete distribution of u_3 is then determined using 1D inverse Fourier transforms for points in the x-y plane.

The new temperature field is obtained in the last step of the numerical scheme. The energy equation is treated in a similar fashion to the integration of the vorticity transport equation. Specifically, we rely on spectral collocation derivative for the convective terms and viscous dissipation function and on factorization of diffusive terms. In conjunction with this spatial discretization scheme, we use the second-order Adams-Bashforth scheme for the convective terms, and treat the dissipation term in an implicit fashion using a Crank-Nicolson formulation. The resulting discrete temperature evolution equation is:

$$\begin{aligned} T^{n+1} \;=\;& (F_x^{-1} e^{-\alpha k_x^2 \Delta t} F_x)(F_y^{-1} e^{-\alpha k_y^2 \Delta t} F_y)(F_z^{-1} e^{-\alpha k_z^2 \Delta t} F_z) T^n \\ & + \frac{1}{2} \frac{\alpha \Delta t}{c_p} [(F_x^{-1} e^{-\alpha k_x^2 \Delta t} F_x)(F_y^{-1} e^{-\alpha k_y^2 \Delta t} F_y)(F_z^{-1} e^{-\alpha k_z^2 \Delta t} F_z) \Phi^n \\ & + \Phi^{n+1}] - \sum_{j=0}^{2} \beta_j \Delta t [(F_x^{-1} F_y^{-1} F_z^{-1}) \\ & (e^{-\alpha |\vec{k}|^2 (j+1) \Delta t} F_x F_y F_z) P^{n-j}] \end{aligned} \tag{8.42}$$

where $P = \nabla.(\vec{u}\, T)$.

8.4 Forcing

In order to maintain a statistically steady field, a forcing function is used on the right-hand side of the vorticity transport equation with forcing applied at lower modes. Specifically, all Fourier modes with wavenumber components equal to 0 or 1 are forced with a constant amplitude a_f, but with a random phase θ. Both the amplitude and phase are independent of $\vec{k}$. Note that the components of $\vec{k}$ take only integer values, since the space period is 2π. Such a force field can be synthesized as

$$f_j(x,y,z) = \sum_{k_x=0}^{1} \sum_{k_y=0}^{1} \sum_{k_z=0}^{1} a_{f_j} e^{i(k_x x + k_y y + k_z z + \theta)} \tag{8.43}$$

and the three components of force field are generated independently. As will be shown later, the kinetic energy dissipation rate does not achieve constant steady-state values using the present forcing approach. Thus, a statistically-steady state will be reached in the sense that the dissipation rate undergoes small-amplitude fluctuation around a mean, constant value.

To reach a statistically steady state, energy loss through viscous dissipation had to be balanced with the energy injection through large-scale foring function. Since we wish to fix the value of the kinetic energy dissipation rate, ϵ, the magnitude of the forcing field is adjusted during the calculations. In particular, the coefficients of the forcing field are adjusted every several time steps so that:

$$\frac{1}{V}\oint \vec{f}\cdot\vec{u}\,dV=\epsilon \tag{8.44}$$

where V is the volume of the compuational domain.

8.5 Initial Conditions

A random velocity field $\vec{u}$ with $-\frac{5}{3}$ spectrum is synthesized by superposing Fourier modes with random phases θ, uniformly distributed in the range of $[0, 2\pi]$,

$$u_i(x,y,z)=\sum_{k_x,k_y,k_z}(k_x^2+k_y^2+k_z^2)^{-\frac{11}{12}}e^{i(k_x x+k_y y+k_z z+\theta_i)} \tag{8.45}$$

The three velocity components, u_i $i = 1, 2, 3$, are generated independently. Since the resulting velocity field may not be divergence free, a correction (or projection) step is necessary to ensure suitable initial conditions. There exist several approaches which can be performed on the synthesized field u_i to render it divergence free. The method we have used is based on finding the vorticity of the synthesized field, then reconstructing the velocity field by inverting Eq. (8.2). This guarantees that the reconstructed field satisfy the divergence-free condition.

As mentioned earlier, we wish to prescribe energy dissipation rates that are characteristic of high-speed flows in pipes or channels with small cross-sectional area. As a representative example, we consider a pipe of diameter

D, with mean flow velocity u_m. Based on these 'input' values, we determine the Reynolds number,

$$Re \equiv \frac{u_m D}{\nu} \tag{8.46}$$

where ν is the kinematic viscosity. Next, we take advantage of well-known correlations for the friction factor (Incropera & DeWitt 1990),

$$\begin{cases} f = 0.316 Re_D^{-1/4} & Re_D \leq 2 \times 10^4 \\ f = 0.184 Re_D^{-1/5} & Re_D \geq 2 \times 10^4 \end{cases} \tag{8.47}$$

use the definition of the friction factor,

$$f \equiv \frac{-(dp/dx)D}{\rho u_m^2/2} \tag{8.48}$$

and the force balance across the area of the pipe to obtain the friction velocity:

$$u_* = \sqrt{\frac{D}{4}\frac{1}{\rho}\frac{dp}{dx}} \tag{8.49}$$

For turbulent pipe flow, the viscous dissipation rate ϵ can be approximated as

$$\epsilon \sim u_*^3/\kappa y \tag{8.50}$$

where y is the distance from the wall and κ is the von-Karman constant. In the calculations, we shall choose values of ϵ corresponding to $y = 12\nu/u_*$, i.e. the viscous dissipation rate at the viscous sublayer.

8.6 Results and Discussion

We present results of three simulations, performed with different resolution grids. The first simulation is performed on a grid with $N_x \times N_y \times N_z = 64 \times 64 \times 64$ mesh points, while the other two are computed with a grid having $N_x \times N_y \times N_z = 96 \times 96 \times 96$ points. For all three cases, the prescribed viscous dissipation rate $\epsilon = 1.25 \times 10^9 m^2/s^3$. Following the discussion of the previous section, the chosen value of ϵ corresponds to a high-speed flow with mean velocity $u_m = 300m/s$, viscosity $\nu = 5.0 \times 10^{-6} m^2/s$, in a pipe of internal diameter $D = 4mm$. Based on the prescibed value of ϵ, the Kolmogorov microscale $\eta = (\nu^3/\epsilon)^{1/4} \sim 0.562 \mu m$.

The conditions of the simulations are listed in Table 8.1 which in particular provides values of the Kolmogorov microscale, η, the integral scale, L_c, the Prandtl number, Pr, as well as the minumum allowable values of the normalized Kolmogorov scale, $\hat{\eta}_{min}$, and the normalized Batchelor scale $\hat{\xi}_{min}$. In estimating these quantities, which are governed by the resolution of the grid, we have related the Batchelor scale to the Kolmogorov scale by $\xi = \sqrt{Pr}\eta$, and the criterion $K \times max(\hat{\eta}, \hat{\xi}) > 1.5$ for the flow to be well resolved. Here, $K = N/2$ is the normalized wavenumber corresponding to wavelength equal to one grid size. Note that, since resolution requirements increase significantly with increasing Prandtl number, we have restricted the computations to the range $Pr < 13$.

Table 8.1

Case	$\hat{\xi}_{min}$	$\hat{\eta}_{min}$	η	L_c	L_c/η	Pr
1	0.0468	0.1146	$0.562\mu m$	$31\mu m$	55.3	6
2	0.03125	0.07654	$0.562\mu m$	$46\mu m$	81.8	6
3	0.03125	0.1148	$0.562\mu m$	$31\mu m$	55.3	13.5

The computations are carried out for simulation times that are long enough for statistically steady conditions to be reached. To verify that this is in fact the case, we plot in Fig. 8.1-8.2 the evolution of the dissipation rate, ϵ, and the root-mean-square velocity, u_{rms}. The evolution of the energy spectra for cases 1-3 is depicted in Figs. 8.3-8.5. The figures indicate that the root-mean-square velocity undergoes small-amplitude fluctuations, and that the energy spectra taken at large simulation times are nearly identical. Thus, statistically-steady conditions are reached during the simulations, and this is not surprising since the simulation times correspond to several eddy turnover times. For the presently selected value of the dissipation rate, $\epsilon \sim 1.25 \times 10^9 m^2/s^3$, the eddy turnover time is about $0.38\mu s$ for case 1, $0.42\mu s$ for case 2, and $0.40\mu s$ for case 3.

The primary results of the temperature simulations are summarized in Figs. 8.6-8.8, which respectively depict the temperature spectrum at different time steps for the cases 1-3. The figures indicate that, after a few turnover times, the temperature spectrum also reaches a statistically steady state. The amplitudes of the Fourier coefficients remain quite small, of the order of $1^o K$ or less. This leads us to expect that spatial temperature fluctuations also remain small. In order to verify this expected trend, we compare in Fig. 8.9 the evolution of the peak within the domain to that of the average temperature. We start from a uniform-temperature initial condition, so that the peak and mean temperatures coincide at time $t = 0$. Due to the (nearly) constant dissipation rate, the mean temperature rises linearly, at a rate of about $1.6^o K/\mu s$. Despite the high-rate of energy injection, and the rapid increase of the mean temperature of the fluid, the peak temperature remains within less than two degrees from the average. This trend is consistent with the results for the temperature spectrum which exhibits amplitude levels of the same order approximately.

We also note that the amplitude of the spatial fluctuations in temperature are weakly dependent on the Prandtl number. This observation, may be verified by comparing the range of amplitudes in the temperature spectra in Figs. 8.6-8.8, should be contrasted with the quasi-one-dimentional predictions in the previous chapter which reflected a linear dependence on Pr. Thus, although the present simulations are restricted to low Reynolds numbers, the present results support the notion that in isotropic turbulence the regions of high energy dissipation also experience vigorous mixing, and that the turbulent mixing of the fluid substantially reduces otherwise sharp thermal gradients. In the following chapter, this intuitive picture will be re-examined in light of simulations of turbulent channel flow.

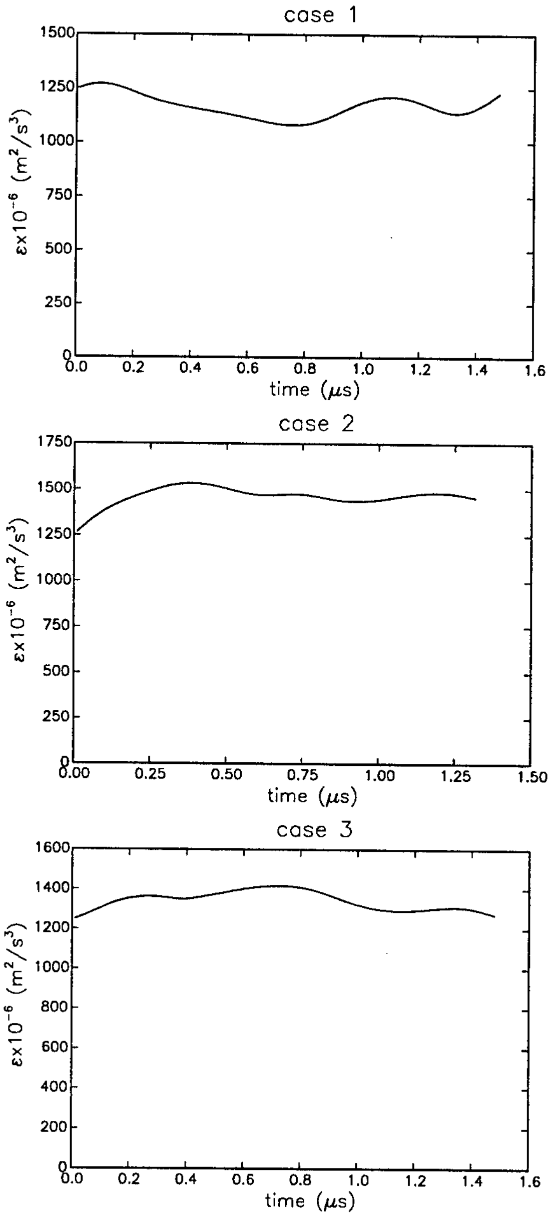

Figure 8.1: The variation of the viscous dissipation rate.

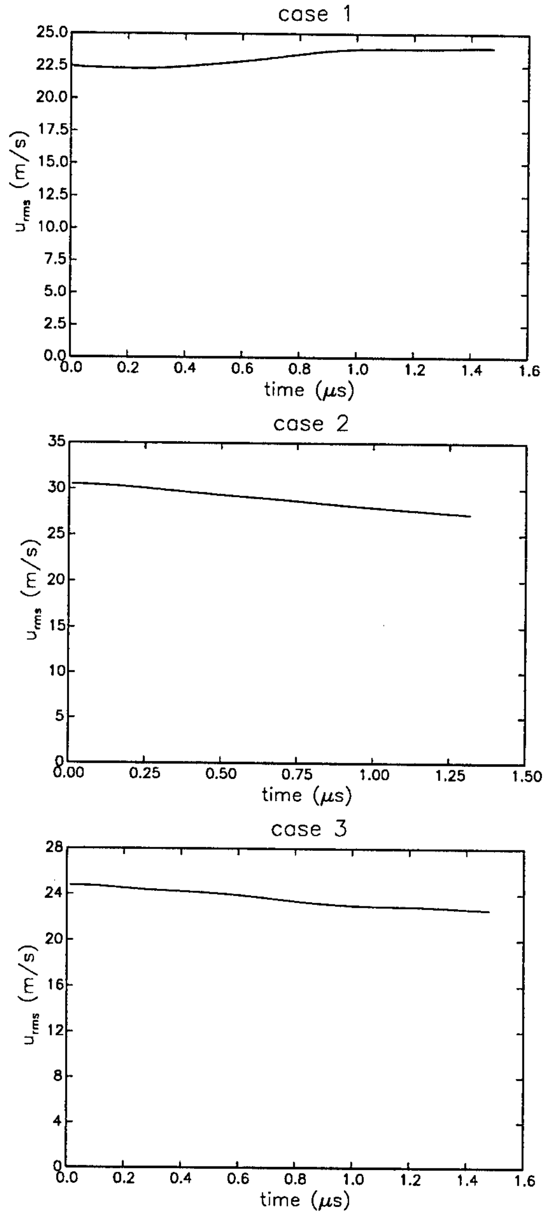

Figure 8.2: The variation of the root-mean=square velocity of turbulent flow.

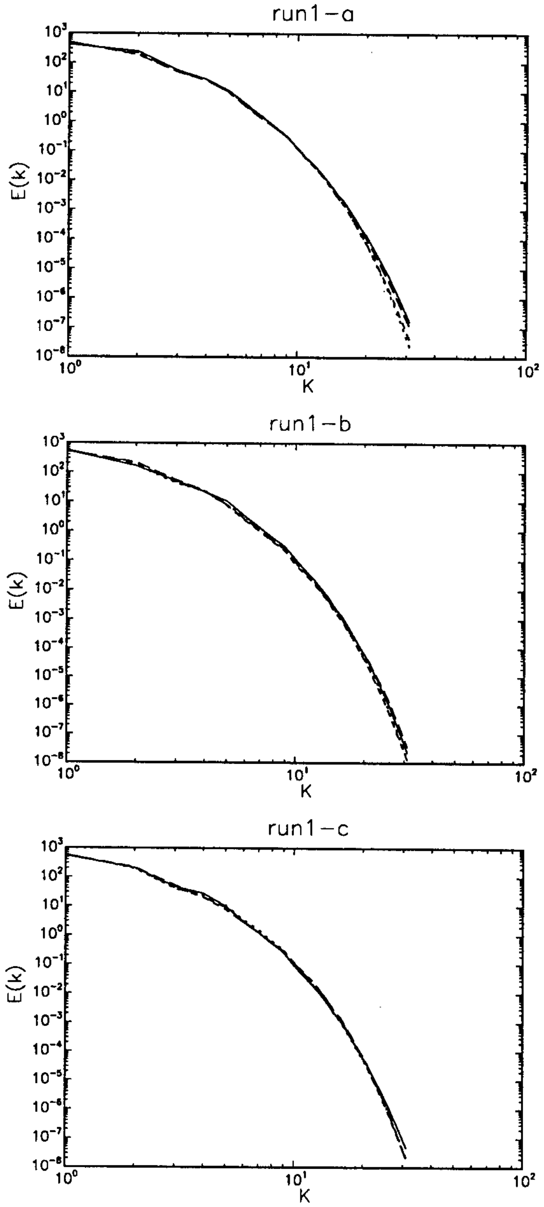

Figure 8.3: The evolution of the energy spectrum for case 1.

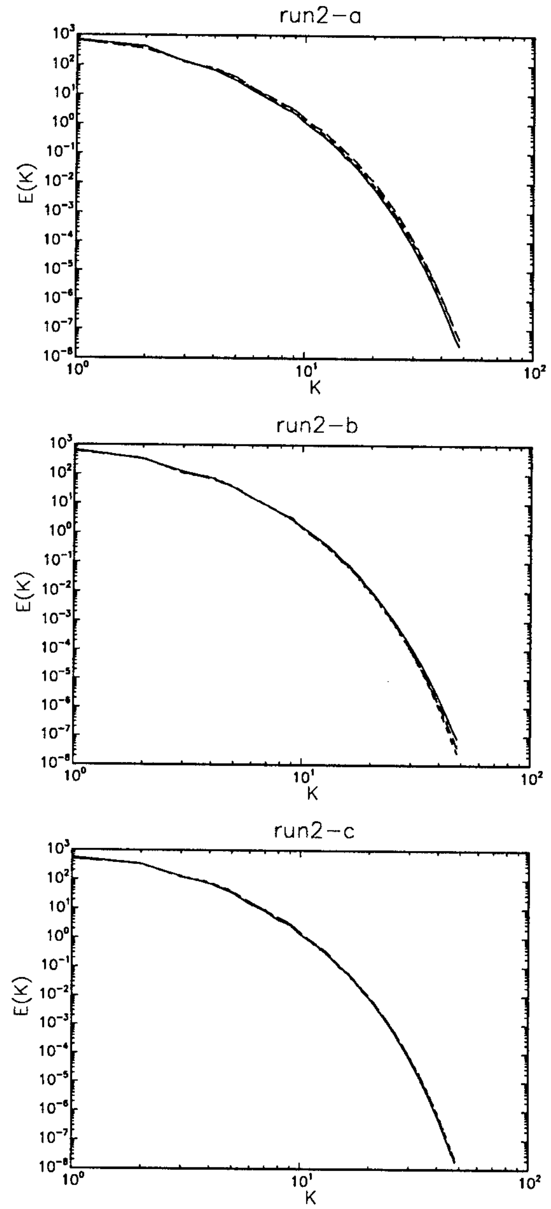

Figure 8.4: The evolution of the energy spectrum for case 2.

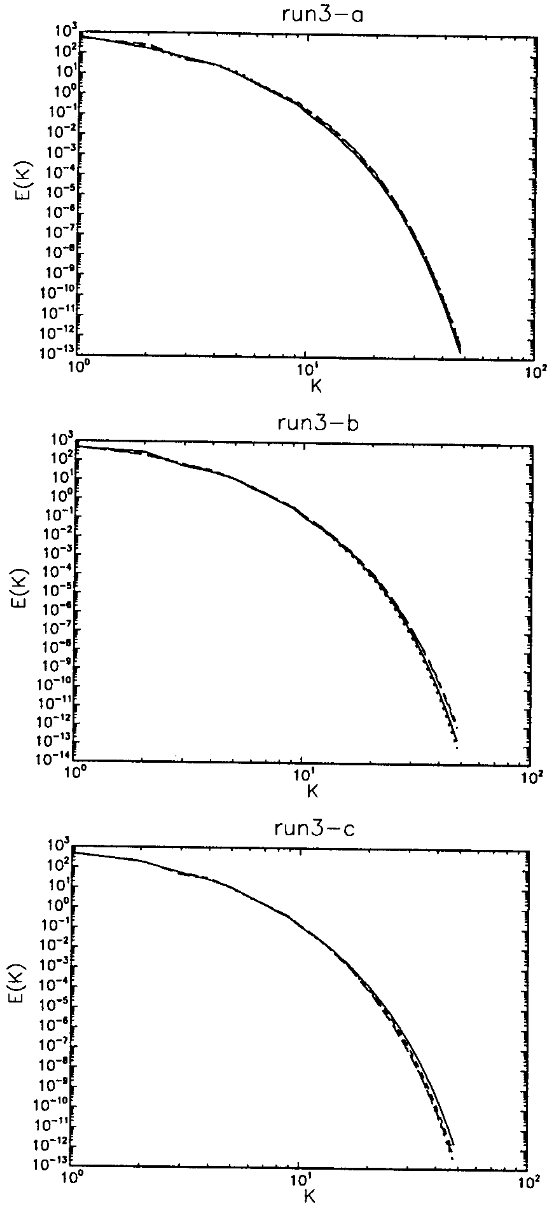
run3-a

run3-b

run3-c

Figure 8.5: The evolution of the energy spectrum for case 3.

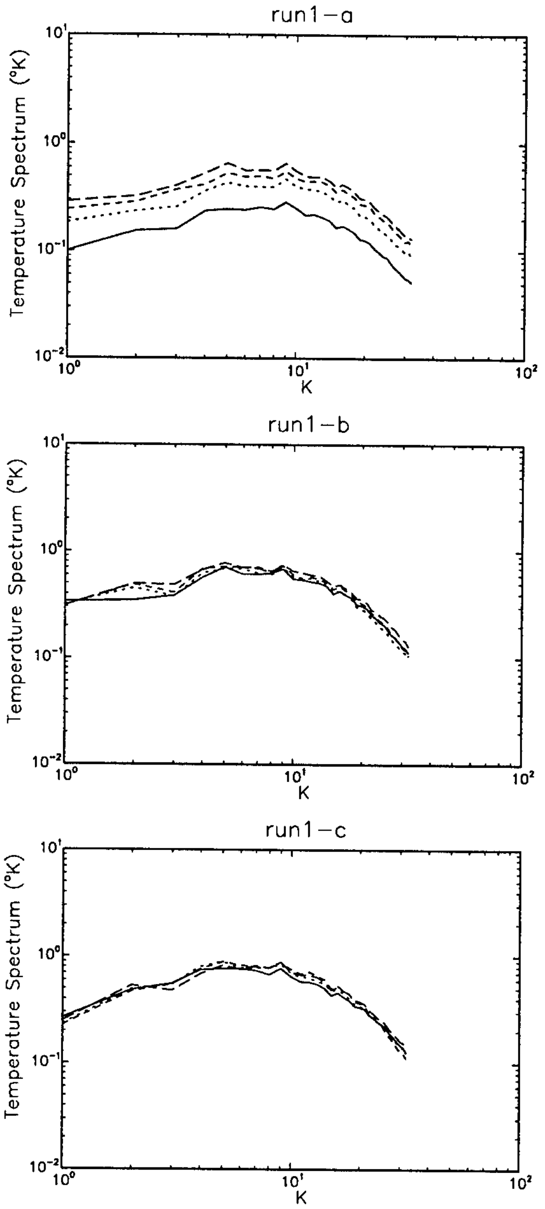

Figure 8.6: Temperature spectrum for case 1.

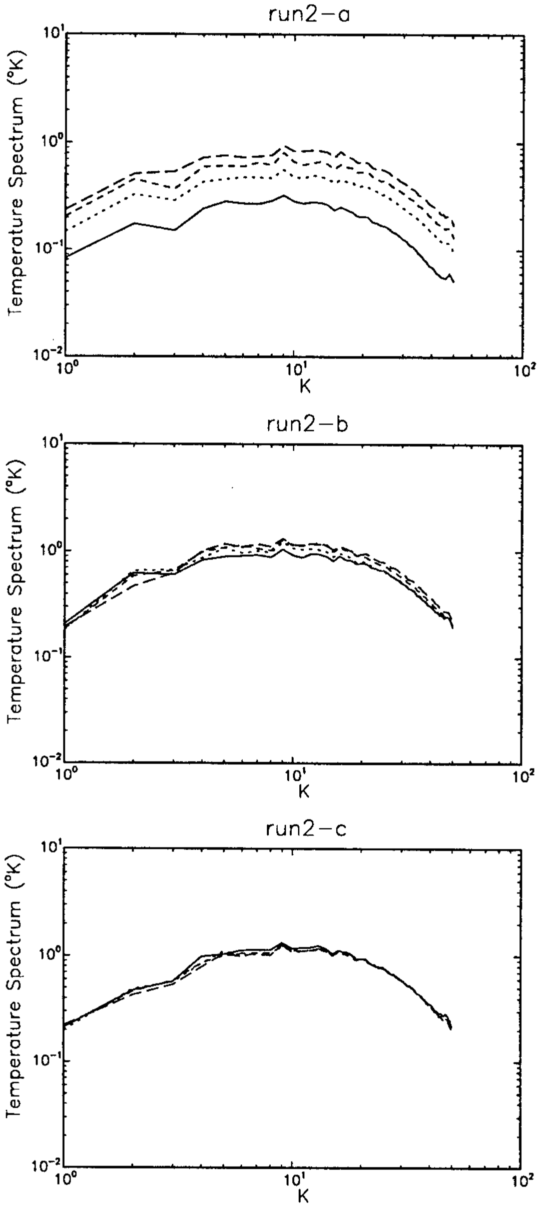

Figure 8.7: Temperature spectrum for case 2.

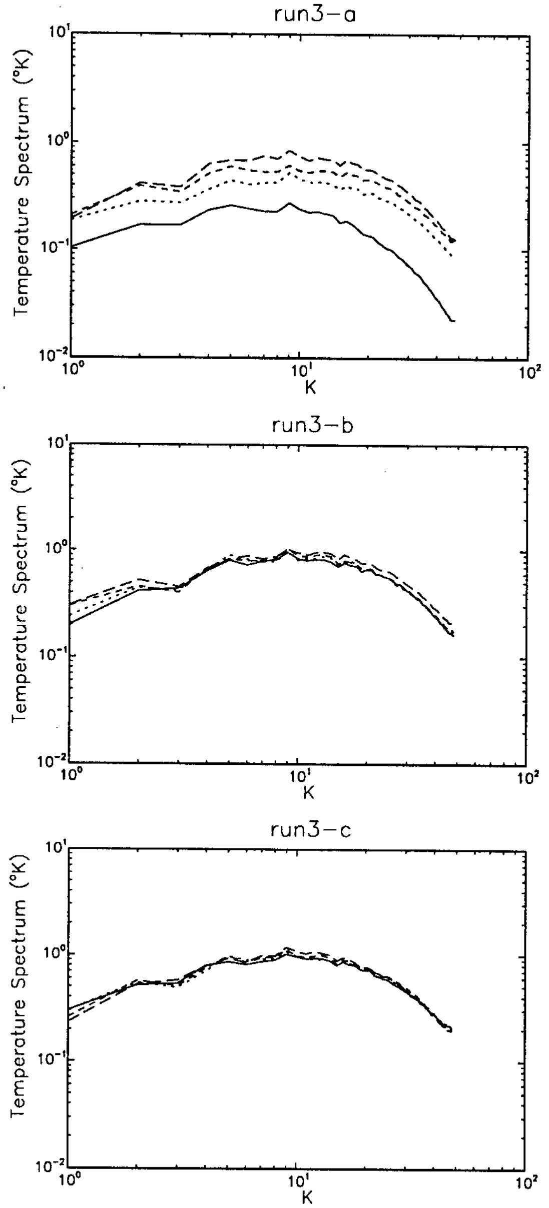

Figure 8.8: Temperature spectrum for case 3.

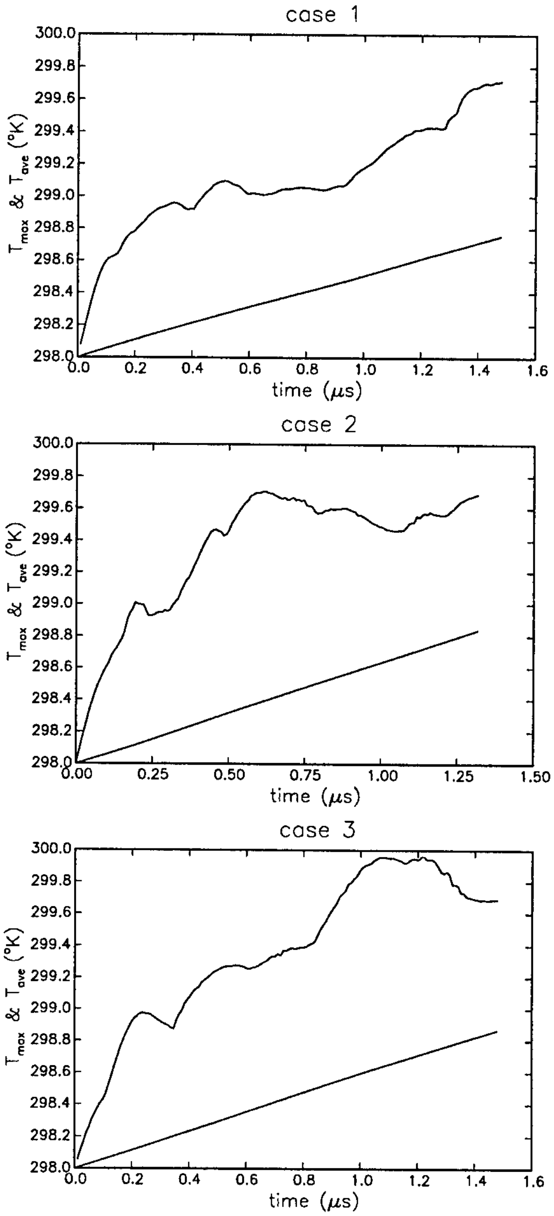

case 1

case 2

case 3

Figure 8.9: The evolution of the maximum and mean temperature.

Chapter 9

Turbulent Channel Flow

9.1 Introduction

In this chapter we examine the effects of shear-induced heating in a plane channel flow. As indicated below, we adapt the vorticity-based formulation of the previous section to periodic channel, and rely on direct numerical simulation of the governing equations to characterize the temperature field in a transitional/turbulent flow environment. The predictions are then contrasted with earlier results for isotropic turbulent flow.

9.2 Formulation

The physical formulation is identical to that of the previous chapter. Specifically, we assume an incompressible fluid with constant physical properties, and adopt a vorticity-based formulation of mass, momentum and energy conservation equations.

In order to describe the set-up of the computations, we recall from the previous chapter the governing equations in component form. We have:

$$\frac{\partial \omega_1}{\partial t} + \frac{\partial s_3}{\partial y} - \frac{\partial s_2}{\partial z} = \nu \nabla^2 \omega_1 \tag{9.1}$$

$$\frac{\partial \omega_2}{\partial t} + \frac{\partial s_1}{\partial z} - \frac{\partial s_3}{\partial x} = \nu \nabla^2 \omega_2 \tag{9.2}$$

$$\frac{\partial \omega_3}{\partial t} + \frac{\partial s_2}{\partial x} - \frac{\partial s_1}{\partial y} = \nu \nabla^2 \omega_3 \tag{9.3}$$

$$\nabla^2 u_1 = \frac{\partial \omega_2}{\partial z} - \frac{\partial \omega_3}{\partial y} \tag{9.4}$$

$$\nabla^2 u_2 = \frac{\partial \omega_3}{\partial x} - \frac{\partial \omega_1}{\partial z} \tag{9.5}$$

$$\nabla^2 u_3 = \frac{\partial \omega_1}{\partial y} - \frac{\partial \omega_2}{\partial x} \tag{9.6}$$

$$\frac{\partial T}{\partial t} + \frac{\partial (u_1 T)}{\partial x} + \frac{\partial (u_2 T)}{\partial y} + \frac{\partial (u_3 T)}{\partial z} = \alpha \nabla^2 T + \frac{\nu}{c_p} \Phi \tag{9.7}$$

where (u_1, u_2, u_3) denotes the velocity vector, $(\omega_1,\ \omega_2,\ \omega_3)$ the vorticity,

$$s_1 \equiv u_3 \omega_2 - u_2 \omega_3$$

$$s_2 \equiv u_1 \omega_3 - u_3 \omega_1$$

$$s_3 \equiv u_2 \omega_1 - u_1 \omega_2$$

t is time, ν the kinematic viscosity, α the thermal diffusivity, c_p the specific heat at constant pressure, and Φ the viscous dissipation function.

The governing equations are solved in periodic channel of height $2d$. The channel walls are assumed to be flat with normal along the z-direction. The mean flow is oriented along the x-direction and y is the spanwise direction. We assume that the velocity and temperature field are periodic along both the x and y directions. No slip boundary conditions are imposed at solid walls are imposed, and heat losses at the walls are modeled using a prescribed heat transfer coefficient. At the solid walls, $z = 0$ and $z = 2d$, we have:

$$\begin{aligned} u_1 = u_2 = u_3 = 0 \\ -k\frac{\partial T}{\partial n} = h(T_w - T_\infty) \end{aligned}$$

where, d is the half depth of the channel, h is heat transfer coefficient, n is normal to the wall, T_w is wall temperature, and T_∞ is the ambient temperature outside channel. In addition to the above conditions, the definition of the vorticity is also enforced at the solid boundaries. As explained below, the mean vorticity at the walls is related to the mean pressure gradient, which is treated as a parameter of the problem.

9.3 Normalization

The numerical scheme discussed in the following sections solves a normalized form of the governing equations. Variables are normalized using the appropriate combination of the the fluid density, ρ, the channel half depth d, the centerline velocity U_c of the undisturbed flow, and the ambient temperature outside of the channel T_∞. For this choice of characteristic density, length, velocity and temperature scales, the normalized governing equations become:

$$\frac{\partial \omega_1}{\partial t} + \frac{\partial s_3}{\partial y} - \frac{\partial s_2}{\partial z} = \frac{1}{Re}\nabla^2\omega_1 \tag{9.8}$$

$$\frac{\partial \omega_2}{\partial t} + \frac{\partial s_1}{\partial z} - \frac{\partial s_3}{\partial x} = \frac{1}{Re}\nabla^2\omega_2 \tag{9.9}$$

$$\frac{\partial \omega_3}{\partial t} + \frac{\partial s_2}{\partial x} - \frac{\partial s_1}{\partial y} = \frac{1}{Re}\nabla^2 \omega_3 \tag{9.10}$$

$$\nabla^2 u_1 = \frac{\partial \omega_2}{\partial z} - \frac{\partial \omega_3}{\partial y} \tag{9.11}$$

$$\nabla^2 u_2 = \frac{\partial \omega_3}{\partial x} - \frac{\partial \omega_1}{\partial z} \tag{9.12}$$

$$\nabla^2 u_3 = \frac{\partial \omega_1}{\partial y} - \frac{\partial \omega_2}{\partial x} \tag{9.13}$$

$$\frac{\partial T}{\partial t} + \frac{\partial (u_1 T)}{\partial x} + \frac{\partial (u_2 T)}{\partial y} + \frac{\partial (u_3 T)}{\partial z} = \frac{1}{RePr}\nabla^2 T + \frac{Ec}{Re}\Phi \tag{9.14}$$

where

$$Re \equiv \frac{\rho U_c d}{\mu} \tag{9.15}$$

is the Reynolds number,

$$Pr \equiv \frac{\nu}{\alpha} \tag{9.16}$$

the Prandtl number, and

$$Ec \equiv \frac{U_c^2}{C_p T_\infty} \tag{9.17}$$

the Eckert number.

9.4 Numerical Scheme

The numerical scheme used is based on a mixed pseudo-spectral finite-difference discretization of the governing equations. We use Fourier expansions in x and y directions, and rely on second-order centered difference in the cross-stream

z direction. By Fourier transforming the governing equations in both x and y, we obtain the following governing system for the Fourier coefficients:

$$\frac{\partial\widehat{\omega_1}}{\partial t} + ik_y\widehat{s_3} - \frac{\partial\widehat{s_2}}{\partial z} = \frac{1}{Re}(-|\vec{k}|^2 + \frac{\partial^2}{\partial z^2})\widehat{\omega_1} \tag{9.18}$$

$$\frac{\partial\widehat{\omega_2}}{\partial t} - ik_x\widehat{s_3} + \frac{\partial\widehat{s_1}}{\partial z} = \frac{1}{Re}(-|\vec{k}|^2 + \frac{\partial^2}{\partial z^2})\widehat{\omega_2} \tag{9.19}$$

$$\frac{\partial\widehat{\omega_3}}{\partial t} + ik_x\widehat{s_2} - ik_y\widehat{s_1} = \frac{1}{Re}(-|\vec{k}|^2 + \frac{\partial^2}{\partial z^2})\widehat{\omega_3} \tag{9.20}$$

$$(-|\vec{k}|^2 + \frac{\partial^2}{\partial z^2})\widehat{u_1} = \frac{\partial\widehat{\omega_2}}{\partial z} - ik_y\widehat{\omega_3} \tag{9.21}$$

$$(-|\vec{k}|^2 + \frac{\partial^2}{\partial z^2})\widehat{u_2} = ik_x\widehat{\omega_3} - \frac{\partial\widehat{\omega_1}}{\partial z} \tag{9.22}$$

$$(-|\vec{k}|^2 + \frac{\partial^2}{\partial z^2})\widehat{u_3} = ik_y\widehat{\omega_1} - ik_x\widehat{\omega_2} \tag{9.23}$$

$$\frac{\partial\hat{T}}{\partial t} + ik_x\widehat{T_a} + ik_y\widehat{T_b} + \frac{\partial}{\partial z}\widehat{T_c} = \frac{1}{RePr}(-|\vec{k}|^2 + \frac{\partial^2}{\partial z^2})\hat{T} + \frac{Ec}{Re}\hat{\Phi} \tag{9.24}$$

where

$$T_a \equiv u_1 T$$

$$T_b \equiv u_2 T$$

$$T_c \equiv u_3 T$$

The boundary conditions for the above system are:

$$\widehat{u_1}\,|_1 = \widehat{u_1}\,|_N = 0$$

$$\widehat{u_2}\,|_1 = \widehat{u_2}\,|_N = 0$$

$$\widehat{u_3}\,|_1 = \widehat{u_3}\,|_N = 0$$

$$\begin{cases} \frac{\partial\widehat{\omega_1}}{\partial z}\,|_{1,N} = 0 & (k_x = k_y = 0) \\ \widehat{\omega_1}\,|_{1,N} = -\frac{\partial\widehat{u_2}}{\partial z} & (|\vec{k}| \neq 0) \end{cases}$$

$$\begin{cases} \frac{\partial \widehat{\omega_2}}{\partial z} \mid_{1,N} = \frac{1}{Re}\frac{\partial \overline{p}}{\partial x} & (k_x = k_y = 0) \\ \widehat{\omega_2} \mid_{1,N} = \frac{\partial \widehat{u_1}}{\partial z} & (\mid \vec{k} \mid \neq 0) \end{cases}$$

$$\widehat{\omega_3} \mid_{1,N} = 0$$

$$\frac{\partial \hat{T}}{\partial n} \mid_{1,N} = N_u(\hat{T} \mid_{1,N} - 1) \tag{9.25}$$

Here, $Nu \equiv hd/k$ is the Nusselt number, and N denotes the number of finite difference points in the z direction. Note that the equation of ω_3 is not coupled with other equations, so that its time integration may be carried out independently of the others. On the other hand, $\widehat{\omega_1}$ and $\widehat{\omega_2}$ are coupled at the boundaries with u_2 and u_1. To overcome the difficulties associated with this coupling, a boundary Green's function technique is used.

Numerical integration of the vorticity transport and energy equations is based on linear multi-step methods. For diffusion terms, an implicit treatment is used based on the second-order Crank-Nicolson scheme. We use the second-order Adams-Bashforth scheme for the convective terms in the vorticity transport equation, and rely on spectral collacation derivative for the convective terms in the energy equation. Following Daube (1992), a staggered grid is employed in z direction. The grid points for the different field quantities are defined as follows:

- u_1, u_2 and ω_3 are computed at nodes $(i\Delta x, j\Delta y, (k+\frac{1}{2})\Delta z)$ for $i, j = 1, \cdots, N$; $k = 1, \cdots, N-1$.

- u_3, ω_1, ω_2 and T are computed at nodes $(i\Delta x, j\Delta y, k\Delta z)$, for $i, j, k = 1, \cdots, N$.

At each interior point, standard second-ordered differences have been used for both first and second derivatives. For nodes adjacent to the channel walls, a special treatment is employed. Specifically, for velocity component u_1, the second derivative is approximated using

$$(\frac{\partial^2 u_1}{\partial z^2})_{\frac{3}{2}} = \frac{4}{3\Delta y^2}(u_{1,\frac{5}{2}} - 3u_{1,\frac{3}{2}} + 2u_{1,1})$$

This approximation comes from the usual centered difference over the nodes $(i, j, \frac{5}{2})$, $(i, j, \frac{3}{2})$, and $(i, j, \frac{1}{2})$ incorporated with the extrapolation of u_1 at the fictitious point $(i, j, \frac{1}{2})$ outside of the computational domain

$$u_{1,\frac{1}{2}} = \frac{1}{3}(u_{1,\frac{5}{2}} - 6u_{1,\frac{3}{2}} + 8u_{1,1})$$

Similarly, the first derivative of u_1 on the nozzle wall $k = 1$ is approximated using:

$$(\frac{\partial u_1}{\partial z})_1 = \frac{1}{3\Delta z}(-u_{1,\frac{5}{2}} + 9u_{1,\frac{3}{2}} - 8u_{1,1})$$

Thus, derivatives in the z-directions are approximated using second-order differences at both the interior and boundary nodes.

Implementation of the numerical scheme is summarized as follows. The Fourier coefficient for the z-component of vorticity, $\widehat{\omega_3}$ is updated by inverting the discrete Helmholtz equation:

$$H\widehat{\omega_3}_i^{n+1} = RW_i^n \tag{9.26}$$

with Dirichlet boundary conditions:

$$\begin{cases} \widehat{\omega_3}_1^{n+1} = 0 \\ \widehat{\omega_3}_N^{n+1} = 0 \end{cases} \tag{9.27}$$

Here, H denotes the Helmholtz operator,

$$\begin{aligned} H\widehat{\omega_3}_i^{n+1} = & -\frac{1}{2Re\Delta z^2}\widehat{\omega_3}_{i-\frac{1}{2}}^{n+1} + (\frac{1}{\Delta t} + \frac{1}{2Re}\mid \vec{k} \mid^2 \\ & + \frac{1}{2Re\Delta z^2})\widehat{\omega_3}_{i+\frac{1}{2}}^{n+1} + \frac{1}{2Re\Delta z^2}\widehat{\omega_3}_{i+\frac{3}{2}}^{n+1} \end{aligned}$$

and RW the explicit source term,

$$\begin{aligned} RW_i^n = & \frac{1}{\Delta t}\widehat{\omega_3}_{i+\frac{1}{2}}^n - ik_x\widehat{s_2}_{i+\frac{1}{2}} + ik_y\widehat{s_1}_{i+\frac{1}{2}} - \frac{1}{2Re}\mid \vec{k} \mid^2\widehat{\omega_3}_{i+\frac{1}{2}}^n \\ & + \frac{1}{2Re}\frac{\widehat{\omega_3}_{i+\frac{3}{2}}^n - 2\widehat{\omega_3}_{i+\frac{1}{2}}^n + \hat{\omega_3}_{i-\frac{1}{2}}^n}{\Delta z^2} \end{aligned} \tag{9.28}$$

Next, we solve for $\widehat{u_1}$ and $\widehat{\omega_2}$ by inverting the coupled system:

$$H_2\widehat{\omega_2}_i^{n+1} = R_2W(\widehat{\omega_2}_i^n) \tag{9.29}$$

$$L_2\widehat{u_1}_{i+\frac{1}{2}}^{n+1} = Q_2W(\widehat{\omega_2}_i^{n+1}) \tag{9.30}$$

with boundary conditions

$$\begin{cases} \widehat{u_1}_1^{n+1} = 0 \\ \widehat{u_1}_N^{n+1} = 0 \end{cases} \tag{9.31}$$

$$\begin{cases} \widehat{\omega_2}_1 = \frac{\partial \widehat{u_1}_1}{\partial z} & \text{if } |\tilde{k}| \neq 0 \\ \widehat{\omega_2}_N = \frac{\partial u_{1N}}{\partial z} & \text{if } |\tilde{k}| \neq 0 \end{cases} \tag{9.32}$$

$$\begin{cases} \frac{\widehat{\omega_2}_1}{\partial z} = Re\frac{\partial \overline{p}}{\partial x}|_1 & \text{if } |\tilde{k}| = 0 \\ \frac{\omega_{2N}}{\partial z} = Re\frac{\partial \overline{p}}{\partial x}|_N & \text{if } |\tilde{k}| = 0 \end{cases} \tag{9.33}$$

Here, H_2 denotes the Helmholtz operator,

$$\begin{aligned} H_2\widehat{\omega_2}_i^{n+1} = & -\frac{1}{2Re\Delta z^2}\widehat{\omega_2}_{i-1}^{n+1} + (\frac{1}{\Delta t} + \frac{1}{2Re}|\tilde{k}|^2 \\ & + \frac{1}{Re\Delta z^2})\widehat{\omega_2}_i^{n+1} - \frac{1}{2Re\Delta z^2}\widehat{\omega_2}_{i+1}^{n+1} \end{aligned} \tag{9.34}$$

and R_2W the explicit source term,

$$\begin{aligned} R_2W(\widehat{\omega_2}_i^n) &= \frac{\widehat{\omega_2}_i^n}{\Delta t} - \frac{\widehat{S_1}_{i+\frac{1}{2}}^n - \widehat{S_1}_{i-\frac{1}{2}}^n}{\Delta z} + ik_x\widehat{S_3}_i^n \\ & -\frac{1}{2Re}|\tilde{k}|^2\widehat{\omega_2}_i^n + \frac{1}{2Re}\frac{\widehat{\omega_2}_{i+1}^n - 2\widehat{\omega_2}_i^n + \widehat{\omega_2}_{i-1}^n}{\Delta z^2} \end{aligned} \tag{9.35}$$

Meanwhile, L_2 represent a discrete "Laplacian" operator defined by:

$$L_2\widehat{u_1}_{i+\frac{1}{2}}^{n+1} = \frac{\widehat{u_1}_{i-\frac{1}{2}}^{n+1}}{\Delta z^2} - (|\tilde{k}|^2 + \frac{2}{\Delta z^2})\widehat{u_1}_{i+\frac{1}{2}}^{n+1} + \frac{\widehat{u_1}_{i+\frac{3}{2}}^{n+1}}{\Delta z^2} \tag{9.36}$$

and

$$Q_2W(\widehat{\omega_2}_{i+1}^{n+1}) = \frac{\widehat{\omega_2}_{i+1}^{n+1} - \widehat{\omega_2}_i^{n+1}}{\Delta z} - ik_y\widehat{\omega_3}_{i+\frac{1}{2}}^{n+1} \tag{9.37}$$

is the corresponding source term.

For non zero modes, boundary Green's functions are employed to decouple the equations of $\hat{u}_1$ and $\hat{\omega}_2$. The boundary Green's function technique exploits the linearity of the elliptic operators by first solving the auxiliary system:

$$\left\{ \begin{array}{l} H_2\widetilde{\omega_2}_i^{n+1} = R_2W(\widehat{\omega_2}_i^n) \\ \widetilde{\omega_2}_1^{n+1} = \widetilde{\omega_2}_N^{n+1} = 0 \end{array} \right. \tag{9.38}$$

$$\left\{ \begin{array}{l} L_2\widetilde{u_1}_{i+\frac{1}{2}}^{n+1} = Q_2W(\widetilde{\omega_2}_i^{n+1}) \\ \widetilde{u_1}_1^{n+1} = \widetilde{u_1}_N^{n+1} = 0 \end{array} \right. \tag{9.39}$$

and then expressing the solution of the full system as:

$$\left\{ \begin{array}{l} \widehat{\omega_2}_i^{n+1} = \widetilde{\omega_2}_i^{n+1}) + \sum_{k=1}^2 \alpha_k g_i^k \\ \widehat{u_1}_{i+\frac{1}{2}}^{n+1} = \widetilde{u_1}_{i+\frac{1}{2}}^{n+1} + \sum_{k=1}^2 \alpha_k f_{i+\frac{1}{2}}^k \end{array} \right. \tag{9.40}$$

Here, g_i^k and $f_{i+\frac{1}{2}}^k$ are the solutions of the elementary problems:

$$\left\{ \begin{array}{ll} H_2 g_i^k = 0 & (k = 1, 2\ ) \\ g_1^1 = 1 & g_N^1 = 0 \\ g_1^2 = 0 & g_N^2 = 1 \end{array} \right. \tag{9.41}$$

$$\begin{cases} L_2 f_i^k = 0 & (k = 1, 2) \\ f_1^k = 0 & f_N^k = 0 \end{cases} \tag{9.42}$$

and α_k $(k = 1, 2)$ are unknown coefficients. Their values are determined by requiring that the corresponding solution satisfies the desired boundary conditions, namely $\widehat{\omega_2}|_i^{n+1} = \frac{\partial \widehat{u_1}}{\partial z}|_i^{n+1}$, at $i = 1$ and $i = N$. This requirement leads to the following linear equation system:

$$\begin{aligned} \alpha_1\left(1 - \frac{3}{\Delta z} f^1_{\frac{3}{2}} + \frac{1}{3\Delta z} f^1_{\frac{5}{2}}\right) \ + \ & \alpha_2\left(\frac{1}{3\Delta z} f^2_{\frac{5}{2}} - \frac{3}{\Delta z} f^2_{\frac{3}{2}}\right) \\ = \ & \frac{3}{\Delta z} \widehat{u_1}^{n+1}_{\frac{3}{2}} - \frac{1}{3\Delta z} \widehat{u_1}^{n+1}_{\frac{5}{2}} \end{aligned} \tag{9.43}$$

$$\begin{aligned} \alpha_1\left(\frac{3}{\Delta z} f^1_{N-1/2} - \frac{1}{3\Delta z} f^1_{N-3/2}\right) \ + \ & \alpha_2\left(1 - \frac{1}{3\Delta z} f^2_{N-3/2} + \frac{3}{\Delta z} f^2_{N-1/2}\right) \\ = \ & \frac{1}{3\Delta z} \widehat{u_1}^{n+1}_{N-3/2} - \frac{3}{\Delta z} \widehat{u_1}^{n+1}_{N-1/2} \end{aligned} \tag{9.44}$$

which is inverted for all Fourier modes with non-vanishing moduli. For the zeroth mode, i.e. when $k_x = k_y = 0$, the equations are integrated with the boundary conditions

$$\frac{\partial \widehat{\omega_2}}{\partial z}|_{1,N} = \frac{1}{\mu} \frac{\partial \overline{p}}{\partial x} \tag{9.45}$$

$$\widehat{u_1}_1^{n+1} = \widehat{u_1}_N^{n+1} = 0 \tag{9.46}$$

$$\tag{9.47}$$

A similar technique is used to update $\widehat{u_2}$ and $\widehat{\omega_1}$. The discrete system of equations is first expressed as:

$$H_3 \widehat{\omega_1}_i^{n+1} = R_3 W(\widehat{\omega_1}_i^n) \tag{9.48}$$

$$L_3 \widehat{u_2}_{i+\frac{1}{2}}^{n+1} = Q_3(\widehat{\omega_1}_i^{n+1}) \tag{9.49}$$

with boundary conditions

$$\begin{cases} \widehat{u_2}_1^{n+1} = 0 \\ \widehat{u_2}_N^{n+1} = 0 \end{cases} \tag{9.50}$$

$$\begin{cases} \widehat{\omega_1}_1 = -\frac{\partial \widehat{u_2}}{\partial z}|_1 & \text{if } |\tilde{k}| \neq 0 \\ \widehat{\omega_1}_N = -\frac{\partial \widehat{u_2}}{\partial z}|_N & \text{if } |\tilde{k}| \neq 0 \end{cases} \tag{9.51}$$

$$\begin{cases} \frac{\partial \widehat{\omega_1}}{\partial z}|_1 = 0 & \text{if } |\tilde{k}| = 0 \\ \frac{\partial \widehat{\omega_1}}{\partial z}|_N = 0 & \text{if } |\tilde{k}| = 0 \end{cases} \tag{9.52}$$

Here, H_3 denotes the Helmoholtz operator,

$$\begin{aligned} H_3 \widehat{\omega_1}_i^{n+1} &= -\frac{1}{2Re\Delta z^2} \widehat{\omega_1}_{i-1}^{n+1} + \left(\frac{1}{\Delta t} + \frac{1}{2Re} |\tilde{k}|^2 \right. \\ &\quad \left. + \frac{1}{Re\Delta z^2}\right) \widehat{\omega_1}_i^{n+1} - \frac{1}{2Re\Delta z^2} \widehat{\omega_1}_{i+1}^{n+1} \end{aligned} \tag{9.53}$$

and R_3W is the corresponding source term,

$$\begin{aligned} R_3W(\widehat{\omega_1}_i^n) &= \frac{\widehat{\omega_1}_i^n}{\Delta t} - ik_y \widehat{S_3}_i^n + \frac{\widehat{S_2}_{i+\frac{1}{2}}^n - \widehat{S_2}_{i-\frac{1}{2}}^n}{\Delta z} \\ &\quad - \frac{1}{2Re} |\tilde{k}|^2 \widehat{\omega_1}_i^n + \frac{1}{2Re} \frac{\widehat{\omega_1}_{i-1}^n - 2\widehat{\omega_1}_i^n + \widehat{\omega_1}_{i+1}^{n+1}}{\Delta z^2} \end{aligned} \tag{9.54}$$

Meanwhile, L_3 is a discrete "Laplacian" operator defined by:

$$L_3 \widehat{u_2}_{i+\frac{1}{2}}^{n+1} = \frac{\widehat{u_2}_{i-\frac{1}{2}}^{n+1}}{\Delta z^2} - \left(|\tilde{k}|^2 + \frac{2}{\Delta z^2}\right) \widehat{u_2}_{i+\frac{1}{2}}^{n+1} + \frac{\widehat{u_2}_{i+\frac{3}{2}}^{n+1}}{\Delta z^2} \tag{9.55}$$

and

$$Q_3(\widehat{\omega_1}_i^{n+1}) = ik_x \widehat{\omega_3}_{i+\frac{1}{2}}^{n+1} - \frac{\widehat{\omega_1}_{i+1}^{n+1} - \widehat{\omega_1}_{i-1}^{n+1}}{\Delta z} \tag{9.56}$$

is the corresponding source term.

For Fourier modes having a non-vanishing modulus, boundary Green's functions are used to decouple the governing equations for vorticity and velocity. We first solve the auxiliary system:

$$\left\{ \begin{array}{l} H_3 \widetilde{\omega_1}_i^{n+1} = R_3 W(\widehat{\omega_1}_i^n) \\ \widetilde{\omega_1}_1^{n+1} = \widetilde{\omega_1}_N^{n+1} = 0 \end{array} \right. \tag{9.57}$$

$$\left\{ \begin{array}{l} L_3 \widetilde{u_2}_{i+\frac{1}{2}}^{n+1} = Q_3(\widetilde{\omega_1}_1^{n+1}) \\ \widetilde{u_2}_1^{n+1} = \widetilde{u_2}_N^{n+1} = 0 \end{array} \right. \tag{9.58}$$

and then express the solution of the whole system as:

$$\left\{ \begin{array}{l} \widehat{\omega_1}_i^{n+1} = \widetilde{\omega_1}_i^{n+1}) + \sum_{k=1}^2 \beta_k \kappa_i^k \\ \widehat{u_2}_{i+\frac{1}{2}}^{n+1} = \widetilde{u_2}_{i+\frac{1}{2}}^{n+1} + \sum_{k=1}^2 \beta_k \lambda_{i+\frac{1}{2}}^k \end{array} \right. \tag{9.59}$$

Here, κ_i^k and $\lambda_{i+\frac{1}{2}}^k$ are the solutions of the elementary problems:

$$\left\{ \begin{array}{ll} H_3 \kappa_i^k = 0 & (k = 1, 2) \\ \kappa_1^1 = 1 & \kappa_N^1 = 0 \\ \kappa_1^2 = 0 & \kappa_N^2 = 1 \end{array} \right. \tag{9.60}$$

$$\left\{ \begin{array}{ll} L_3 \lambda_i^k = 0 & (k = 1, 2) \\ \lambda_1^k = 0 & \lambda_N^k = 0 \end{array} \right. \tag{9.61}$$

and β_k $(k = 1, 2)$ are unknown coefficients whose values are determined by requiring that the corresponding solution satisfied the desired wall boundary conditions. This requirement leads to the following linear equation system:

$$\begin{aligned} \beta_1(1 + \frac{3}{\Delta z}\lambda_{\frac{3}{2}}^1 - \frac{1}{3\Delta z}\lambda_{\frac{5}{2}}^1) & + \beta_2(\frac{3}{\Delta z}\lambda_{\frac{3}{2}}^2 - \frac{1}{3\Delta z}\lambda_{\frac{5}{2}}^2) \\ & = -\frac{3}{\Delta z}\widetilde{u_2}_{\frac{3}{2}}^{n+1} + \frac{1}{3\Delta z}\widetilde{u_2}_{\frac{5}{2}}^{n+1} \end{aligned} \tag{9.62}$$

$$\begin{aligned} \beta_1(\frac{1}{3\Delta z}\lambda_{N-3/2}^1 - \frac{3}{\Delta z}\lambda_{N-1/2}^1) & + \beta_2(1 - \frac{3}{\Delta z}\lambda_{N-1/2}^2 + \frac{1}{3\Delta z}\lambda_{N-3/2}^2) \\ & = \frac{1}{3\Delta z}\widetilde{u_2}_{N-1/2}^{n+1} - \frac{1}{3\Delta z}\widetilde{u_2}_{N-3/2}^{n+1} \end{aligned} \tag{9.63}$$

which is inverted for every mode.

For the zeroth mode, the equations are subjected to the following boundary conditions,

$$\frac{\partial \widehat{\omega_1}}{\partial z}|_{1,N} = 0 \tag{9.64}$$

$$\widehat{u_2}_1^{n+1} = \widehat{u_2}_N^{n+1} = 0 \tag{9.65}$$

and inverted independently of the others.

The velocity compoment u_3 is updated by the discrete equation:

$$\begin{aligned}\frac{1}{\Delta z^2}\widehat{u_3}_{i-1}^{n+1} - (|\tilde{k}|^2 + \frac{2}{\Delta z^2})\widehat{u_3}_i^{n+1} \quad &+ \quad \frac{1}{\Delta z^2}\widehat{u_3}_{i+1}^{n+1} \\ = ik_y\widehat{\omega_1}_i^{n+1} - ik_x\widehat{\omega_2}_i^{n+1}&\end{aligned} \tag{9.66}$$

with the boundary condition

$$\widehat{u_3}_1^{n+1} = \widehat{u_3}_N^{n+1} = 0 \tag{9.67}$$

Finally, the temperature field is advanced by inverting the discrete elliptic equation:

$$G\hat{T}_i^{n+1} = R\hat{T}_i^n \tag{9.68}$$

subject to the boundary condition,

$$\begin{cases} \frac{\partial \widehat{T}}{\partial z}|_1 = Nu(\widehat{T}_1 - 1) & \text{if } |\tilde{k}| = 0 \\ \frac{\partial \widehat{T}}{\partial z}|_1 = Nu\widehat{T}_1 & \text{if } |\tilde{k}| \neq 0 \end{cases} \tag{9.69}$$

$$\begin{cases} \frac{\partial \widehat{T}}{\partial z}|_N = -Nu(\widehat{T}_N - 1) & \text{if } |\tilde{k}| = 0 \\ \frac{\partial \widehat{T}}{\partial z}|_N = -Nu\widehat{T}_N & |\tilde{k}| \neq 0 \end{cases} \tag{9.70}$$

Here, G denotes the one-dimensional Helmholtz operator,

$$\begin{aligned} G\hat{T}_i^{n+1} &= -\frac{1}{2RePr\Delta z^2}\hat{T}_{i-1}^{n+1} + (\frac{1}{\Delta t} + \frac{1}{2RePr}|\tilde{k}|^2 \\ &+\frac{1}{2RePr\Delta z^2})\hat{T}_i^{n+1} - \frac{1}{2RePr\Delta z^2}\hat{T}_{i+1}^{n+1} \end{aligned} \tag{9.71}$$

RT the corresponding source term,

$$\begin{aligned} R\hat{T}_i^n &= \frac{\hat{T}_i^n}{\Delta t} - ik_x\widehat{T_{ai}}^n - ik_y\widehat{T_{bi}}^n - \frac{\widehat{T_{ci+1}}^n - \widehat{T_{ci-1}}^n}{2\Delta z} - \frac{1}{2RePr}|\tilde{k}|^2\hat{T}_i^n \\ &+\frac{1}{2RePr}\frac{\hat{T}_{i+1}^n - 2\hat{T}_i^n + \hat{T}_{i-1}^n}{\Delta z^2} + \frac{Ec}{2Re}(\hat{\Phi}_i^{n+1} + \hat{\Phi}_i^n) \end{aligned} \tag{9.72}$$

9.5 Initial Conditions

Simulations are performed in channel of depth of $0.2mm$. The periodic lengths in thestreamwise and spanwise directions are $0.4\pi mm$ and $0.2\pi mm$ respectively. The initial velocity field is obtained by superposing on the one-dimensional streamwise mean velocity profile (Fig. 9.1) a randomly generated homogeneous 3-dimensional velocity field. The undisturbed mean velocity profile is calculated using the two-layer model discussed in chapter 7, with the centerline velocity $U_c = 150m/s$. The purturbation velocity field has a root mean-square value equal to $0.02U_c$. For a kinematic viscosity $\nu = 5.0 \times 10^6 m^2/s$, the Reynolds number based on centerline velocity is about $6,000$. In order to avoid excessive resolution requirements, a moderate value of the Prandtl number, $Pr = 7$, is selected. The temperature field is initialized using the mean temperature distribution solution obtained in Chapter 7 (Fig. 9.2).

Another parameter we need to be concerned is the value of mean pressure gradient, i.e. $\frac{\partial \overline{p}}{\partial x}$, which controls the intensity of forcing within the channel, and therefore the mass flow rate within the channel. When the undisturbed centerline velocity is given, the corresponding friction velocity can be obtained numerically using the two-layer turbulent velocity model within the channel (Chapter 7). Then, the mean pressure gradient $\frac{\partial \overline{p}}{\partial x}$ is determined through,

$$\frac{\partial \overline{p}}{\partial x} = -\frac{\rho}{d} u_*^2 \tag{9.73}$$

The mean pressure gradient with respect to y, $\frac{\partial \overline{p}}{\partial y}$, is set to zero.

9.6 Results and Discussion

The computations are performed on a grid with $N_x \times N_y \times N_z = 80 \times 80 \times 160$ mesh points. We have let code run for $10,500$ time steps, which is long enough for the perturbation field to undergo significant deformation. The time step Δt is chosen to be $0.1 \Delta z$ in normalized units, i.e. the Courant number is approximately 0.1. The corresponding physical time step is about $0.818 ns$. As mentioned in the previous section, wall heat transfer is modeled using a heat transfer coefficient. In the simulation, we have selected a value $h = 100 W/m^2 \cdot {}^o K$, which is the representative of forced air cooling at low speed.

The evolution of the mean flow is depicted in Figs 9.3-9.5, which show profiles of the mean streamwise velocity $\overline{u_x}$, mean spanwise vorticity $\overline{\omega_y}$, and mean temperature respectively. The profiles are obtained by averaging the predictions along horizontal planes, i.e. planes parallel to the x-y plane. The figures indicate that the velocity, vorticity and thermal boundary layers adjust a little during the initial stages of the computations. Such an adjustment is not surprising since the mean flow is initialized using the approximate profiles of a two-layer model.

Spatial fluctations of the velocity and vorticity fields are shown Figs. 9.6-9.11 which respectively shown profiles of r.m.s. values of the fluctating part of the streamwise, spanwise, and cross-stream velocity components, and of the streamwise, spanwise, and cross-stream vorticity components. The fluctating components are found by subtracting from the raw data the corresponding mean value on horizontal planes, and the averaging on the same planes. The figures indicate that the velocity and vorticity fluctations also undergo an adjustment as time evolves, with an appreciable drop near the centerline of the channel. This adjustment is to be expected since the initial field used in the computations was perturbed using a homogeneous isotropic field.

Spatial fluctuations of the temperature field are first illustrated using temperature distribution plotted along streamwise planes, i.e. whose normal is parallel to the streamwise x-axis. Figures 9.12-9.14 show temperatures contours in the plane $x = 2\pi d$ at times $t = 2.05\mu s$, $t = 5.32\mu s$, and $t = 8.59\mu s$, respectively. The figures show that the temperature boundary layers at both the lower and upper walls spread slightly during the initial stages, and that the temperature distribution is significantly more deformed on the upper wall than the lower one. The shape of the deformation is indicative of the presence of concentrated eddies within the boundary layers. Comparison of the temperature contours with velocity and vorticity distribution generated in a similar fashion (not shown) indicated that the non-uniformities observed near the top of Figs. 9.12-9.14 are due to the presence of streamwise vortices which are periodically generated within the boundary layer and later ejected into the "free stream".

The magnitude of the deformation indicated by the contour plots of the temperature field leads us to expect significant temperature fluctations along horizontal planes. To quantify these deformations, Fig. 9.15 compares cross-stream profiles of the peak temperature and the mean temperature. The results show that the largest departures occur within the boundary layer structure. In particular, for the conditions of the simulation, the profiles for the mean temperature and peak temperature achieve their maxima at approximately the same location near the upper boundary, with temperature rises above the ambient of 10°K and 13°K, respectively. Thus, the temperature fluctuations can achieve amplitudes as large as 30% of the mean temperature rise, and thus represent a significant fraction of the total heating locally experienced by the fluid.

The present results should be contrated with those of the previous chapter which, for the case of isotropic turbulence, reflected spatial temperature fluctuations having very small amplitudes. We believe that this contrast is due to differences in the flow mechanisms which are associated with the observed heating. In the isotropic case, rapid mixing of the mixture effectively reduces the likelihood of occurrence of sharp temperature gradients. Such mechanisms are clearly lacking near solid boundaries, where concentrated eddies may be sustained for relatively large time periods in regions of low velocity.

At any rate, the result of the present computations indicate that the unsteady near-wall flow dynamics in transitional/turbulent flow regime can have a significant impact on shear heating phenomena. In particular, estimates of peak temperature based on mean temperature profiles only should generally be expected to significantly underpredict the risk of mixture ignition.

At present, it is unfortunately not feasible to rely on direct numerical simulations to extend the predictions to the high-Reynolds-number high-Prandtl-number regime. It would be possible, however, to obtain some conservative estimates by extrapolating low-Reynolds-number with the help of some reasonable assumptions, such as Reynolds-number independence and linear dependence on the Prandtl number. Nonetheless, it would be crucial that such extrapolations be tested against experimental results, and that experiements are conducted in order to carefully examine, in particular, the impact of near-wall dynamics on shear heating of the mixture.

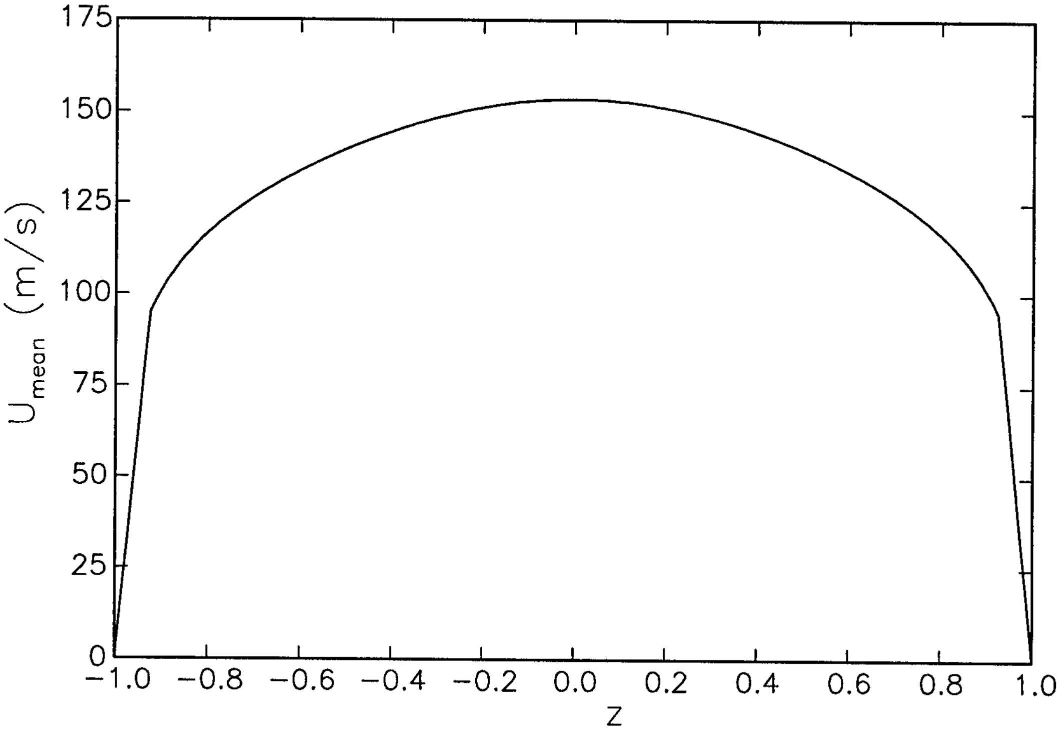

Figure 9.1: The initial undisturbed streamwise velocity profile.

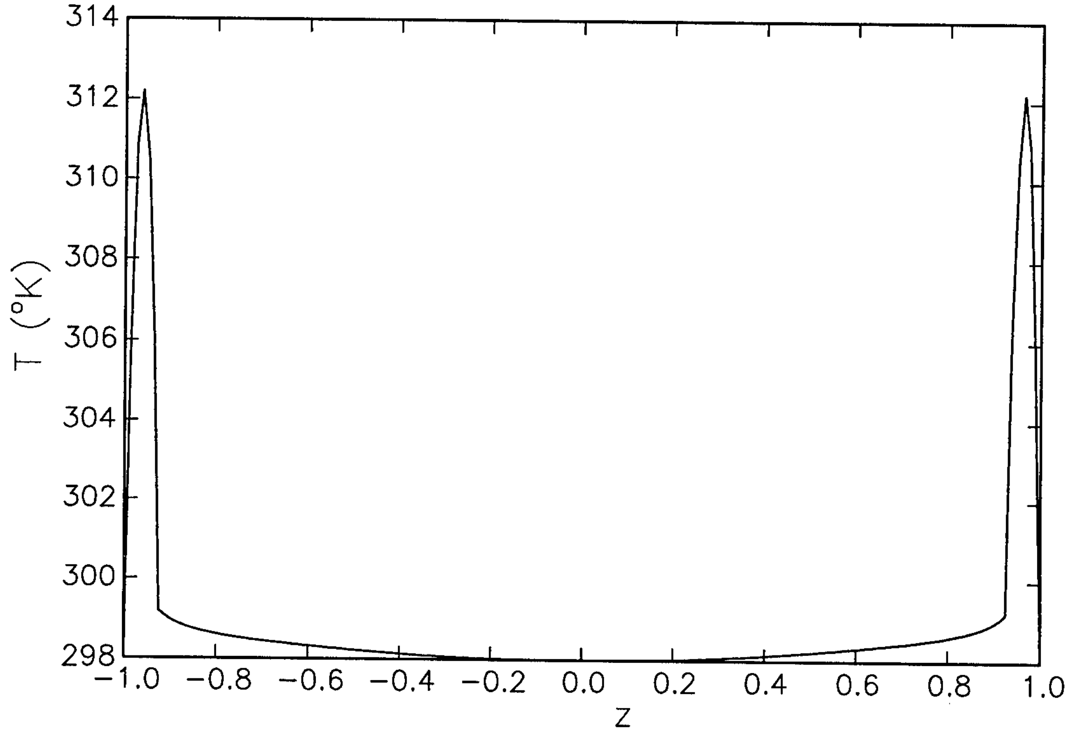

Figure 9.2: The initial cross-stream temperature profile with $Pr = 7$.

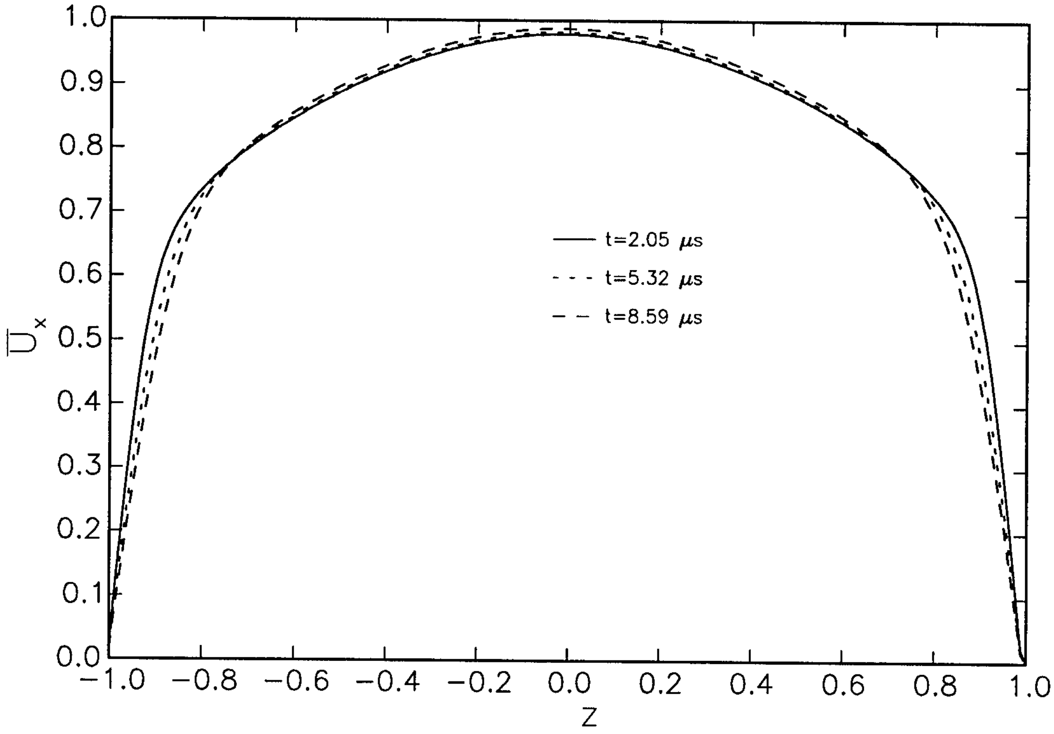

Figure 9.3: The evolution of the mean streamwise velocity u_x.

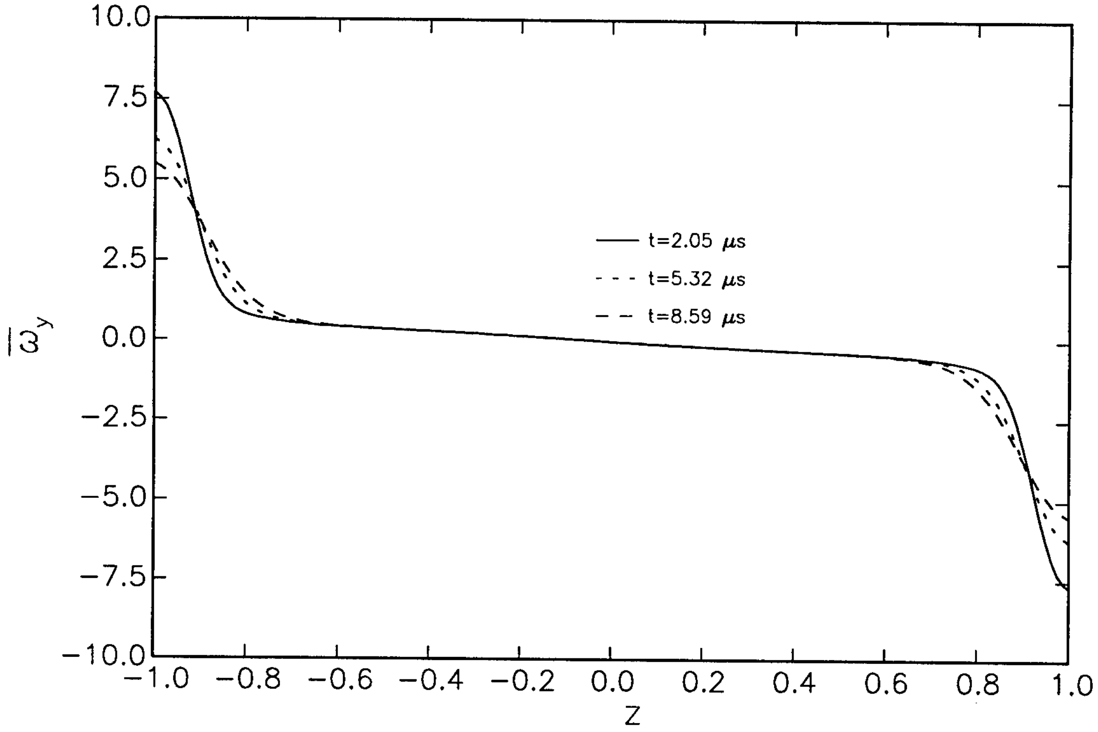

Figure 9.4: The evolution of the mean spanwise vorticity ω_y.

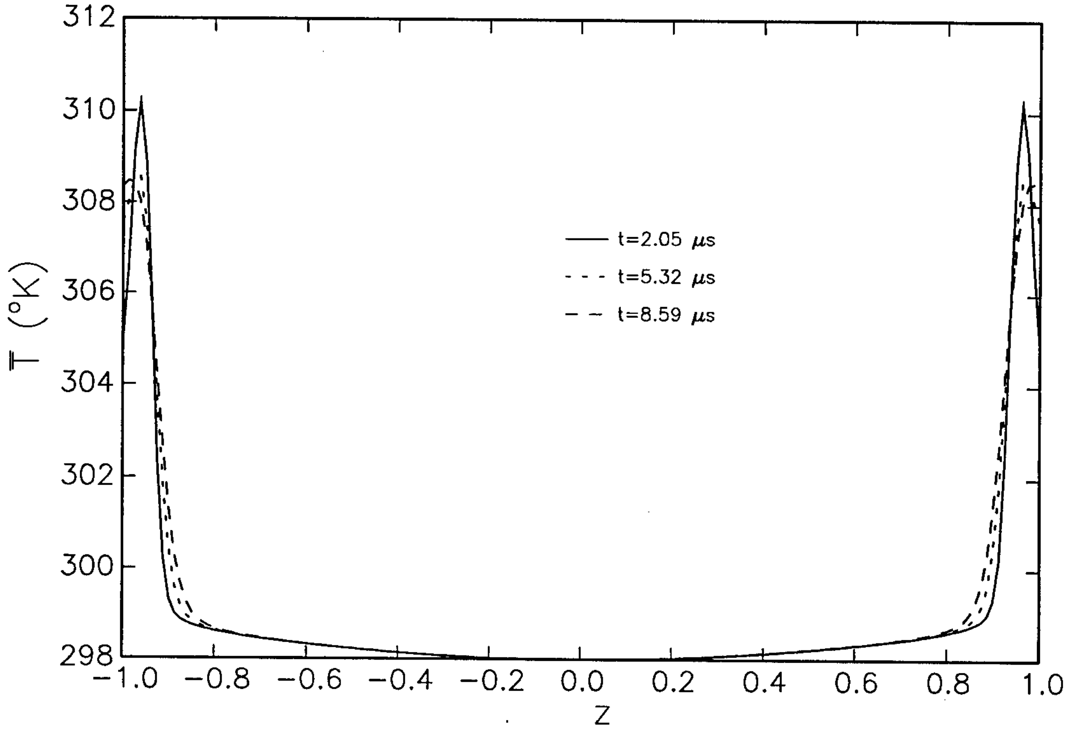

Figure 9.5: The mean temperature evolution.

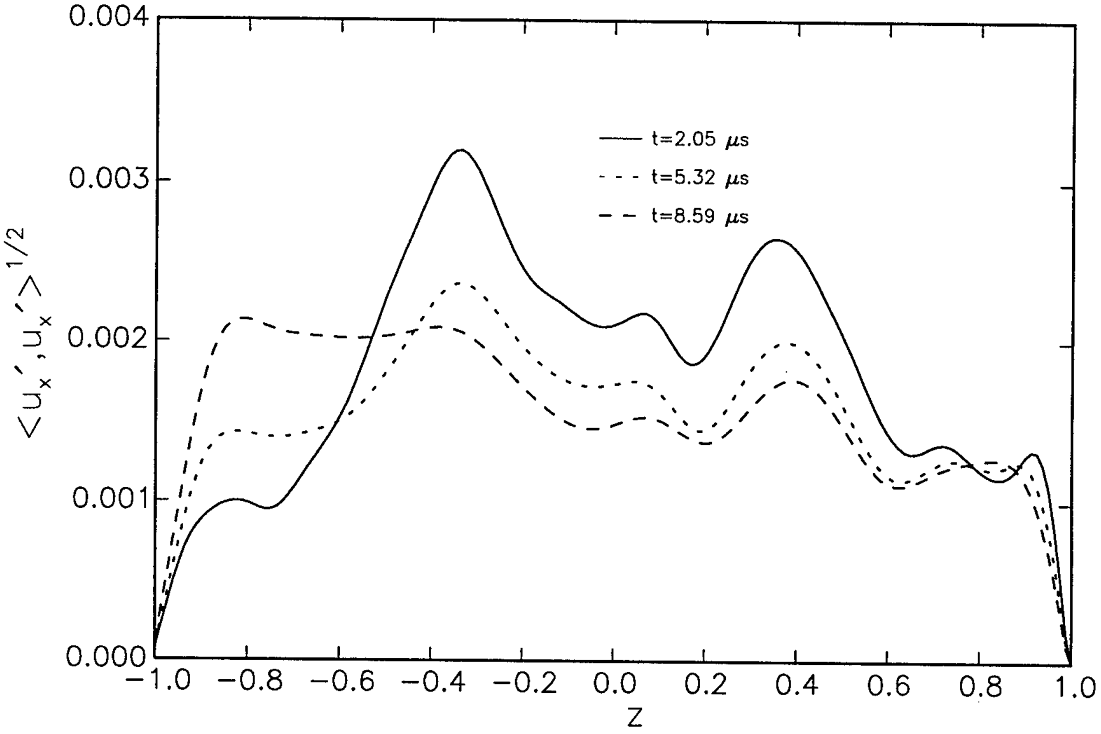

Figure 9.6: The evolution of root mean-square streamwise velocity.

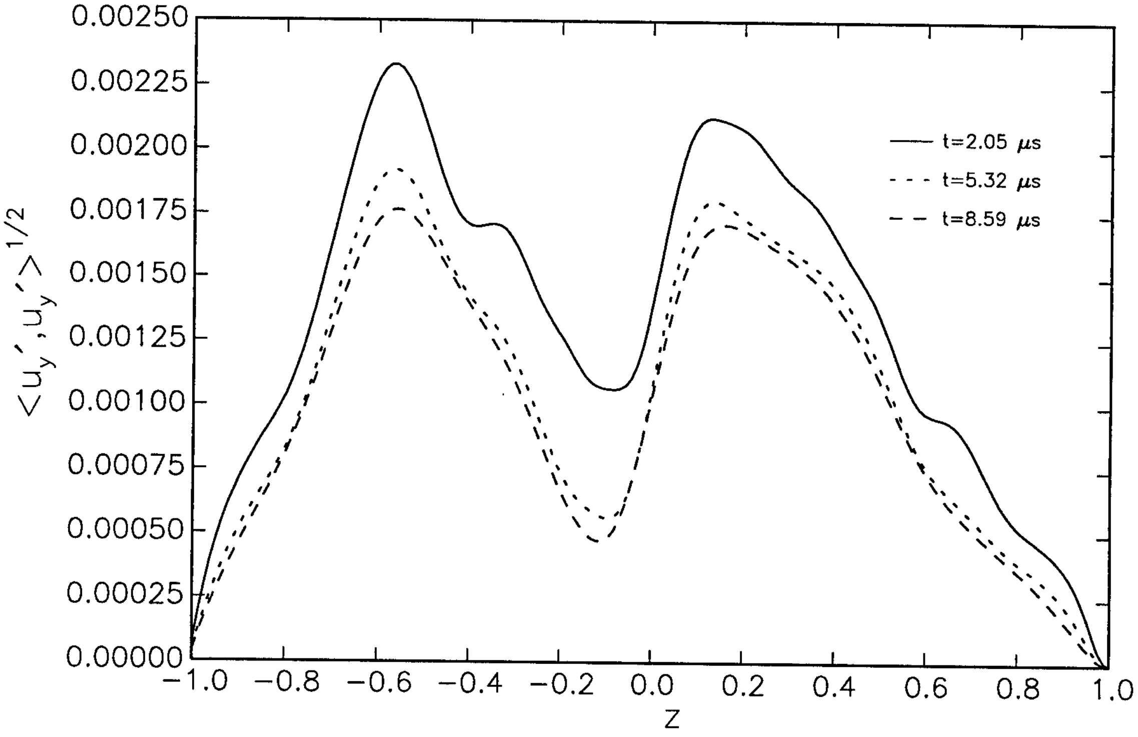

Figure 9.7: The evolution of root mean-square spanwise velocity.

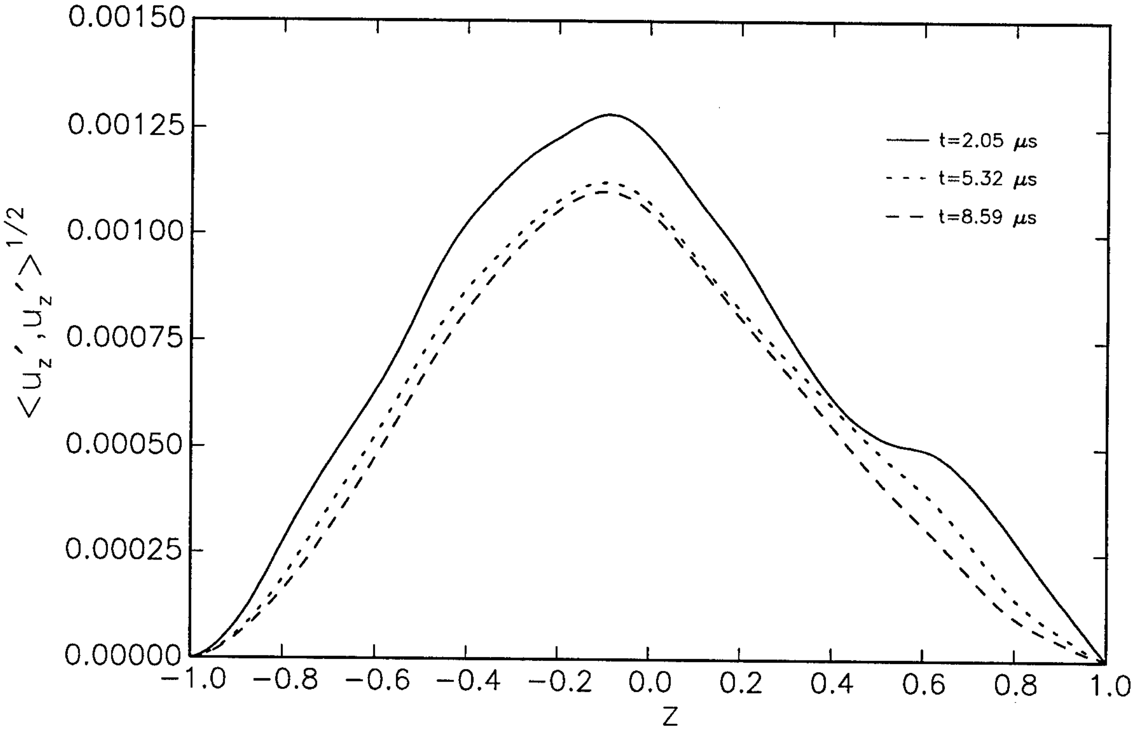

Figure 9.8: The evolution of root mean-square cross-stream velocity.

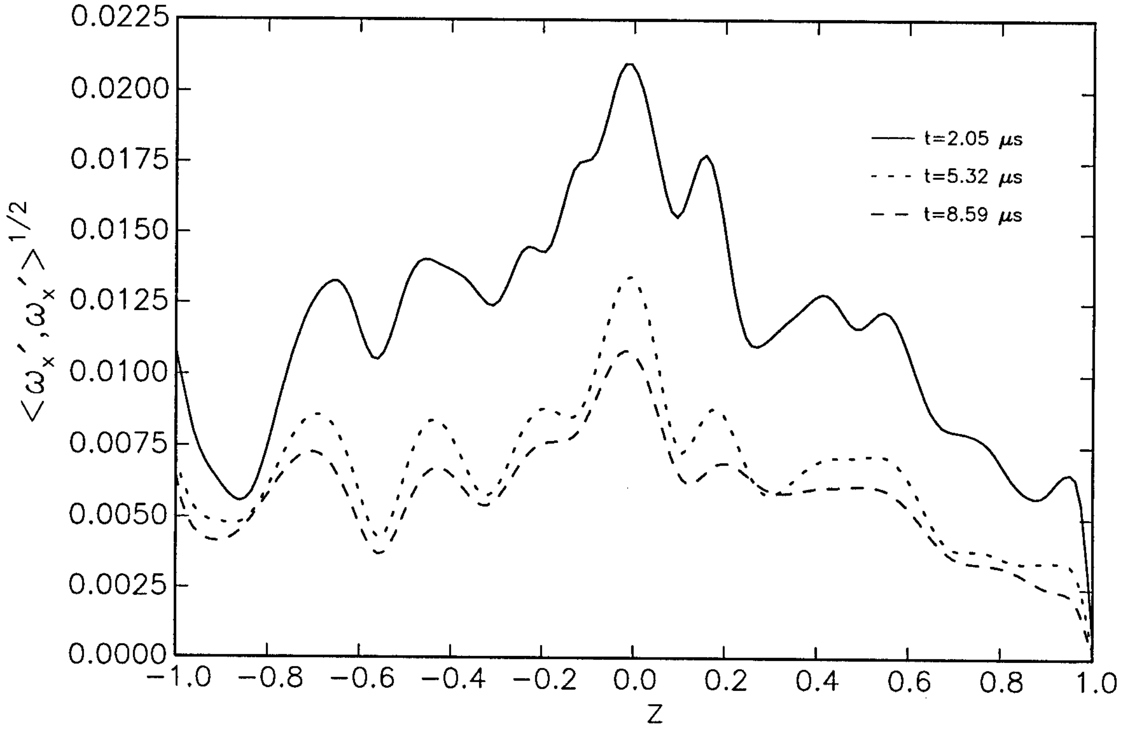

Figure 9.9: The evolution of root-mean-square streamwise vorticity.

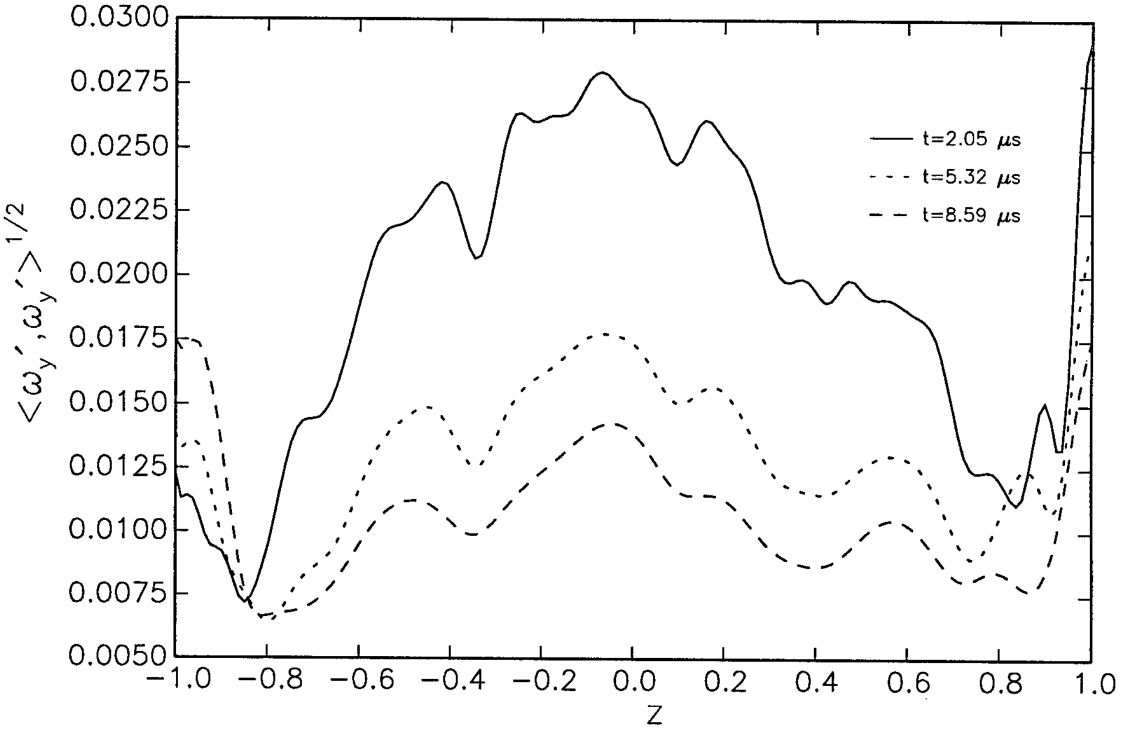

Figure 9.10: The evolution of root-mean-square spanwise vorticity.

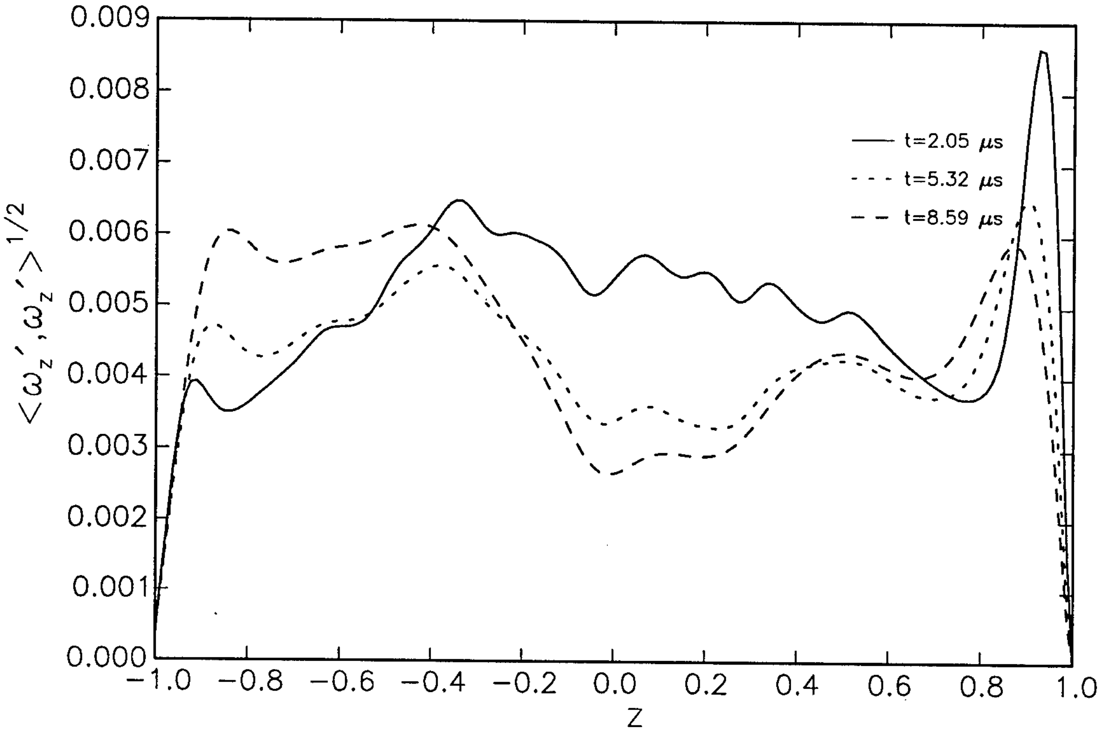

Figure 9.11: The evolution of root-mean-square cross-stream vorticity.

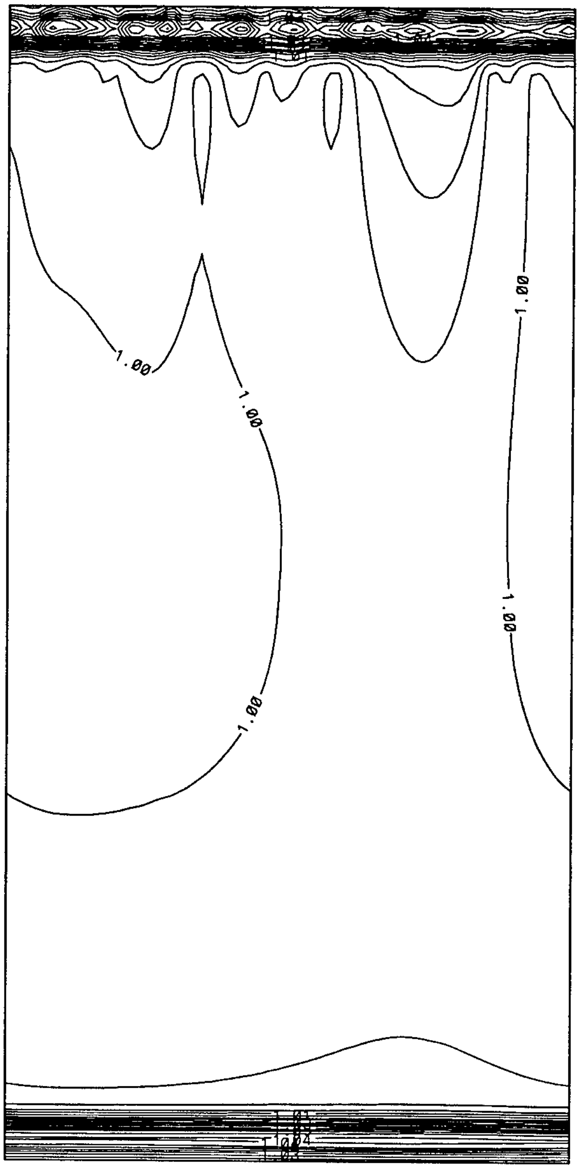

Figure 9.12: The contour plot of temperature distribution in y-z plane($x = 2\pi d$) at $t = 2.05\mu s$.

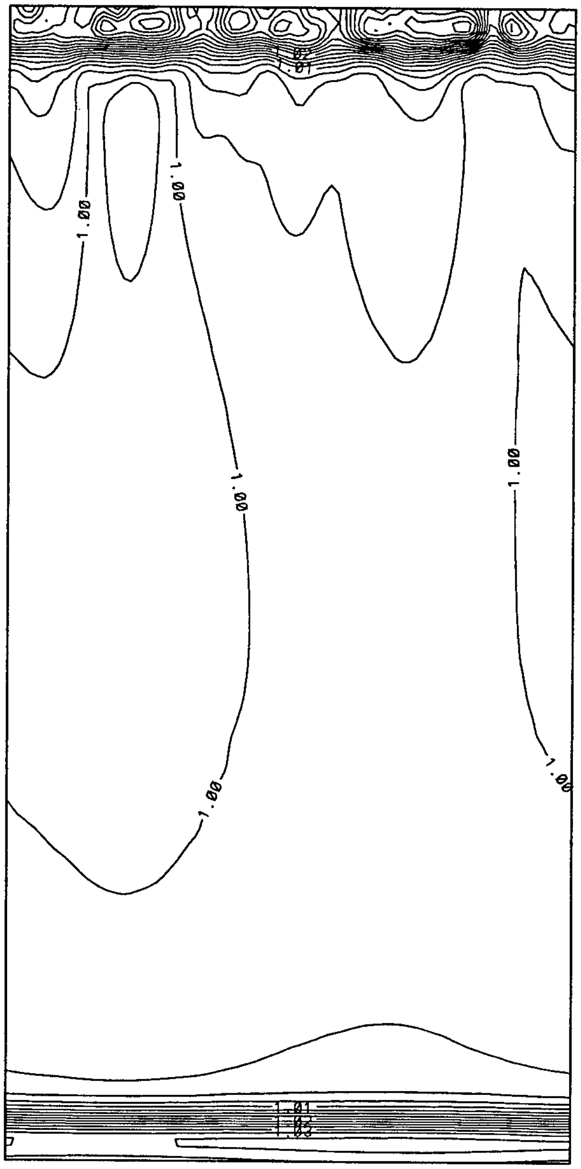

Figure 9.13: The contour plot of temperature distribution in y-z plane($x = 2\pi d$) at $t = 5.32\mu s$.

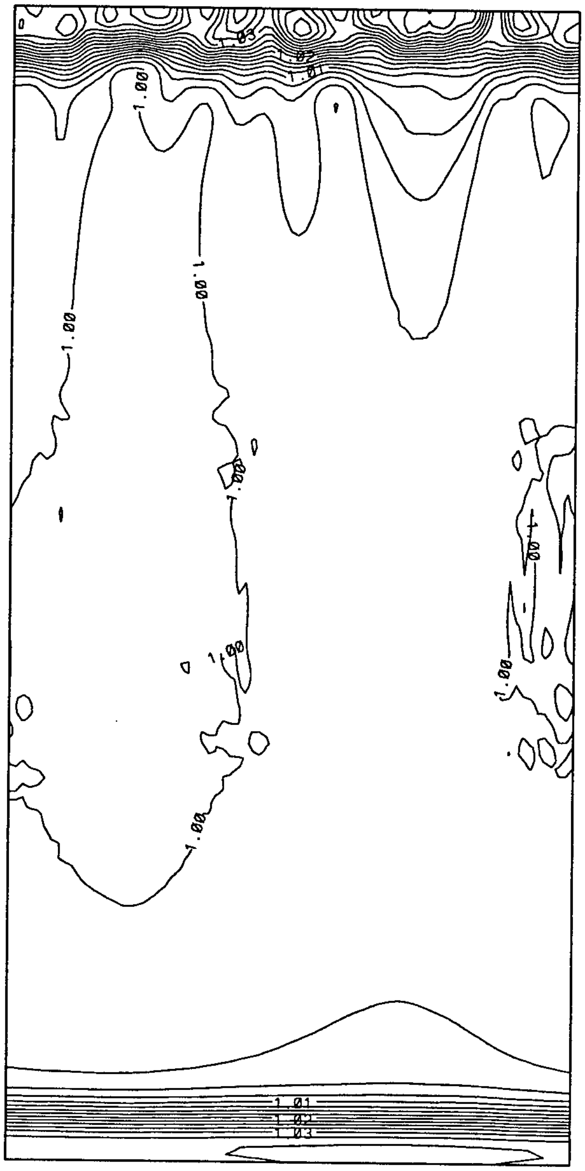

Figure 9.14: The contour plot of temperature distribution in y-z plane($x = 2\pi d$) at $t = 8.59\mu s$.

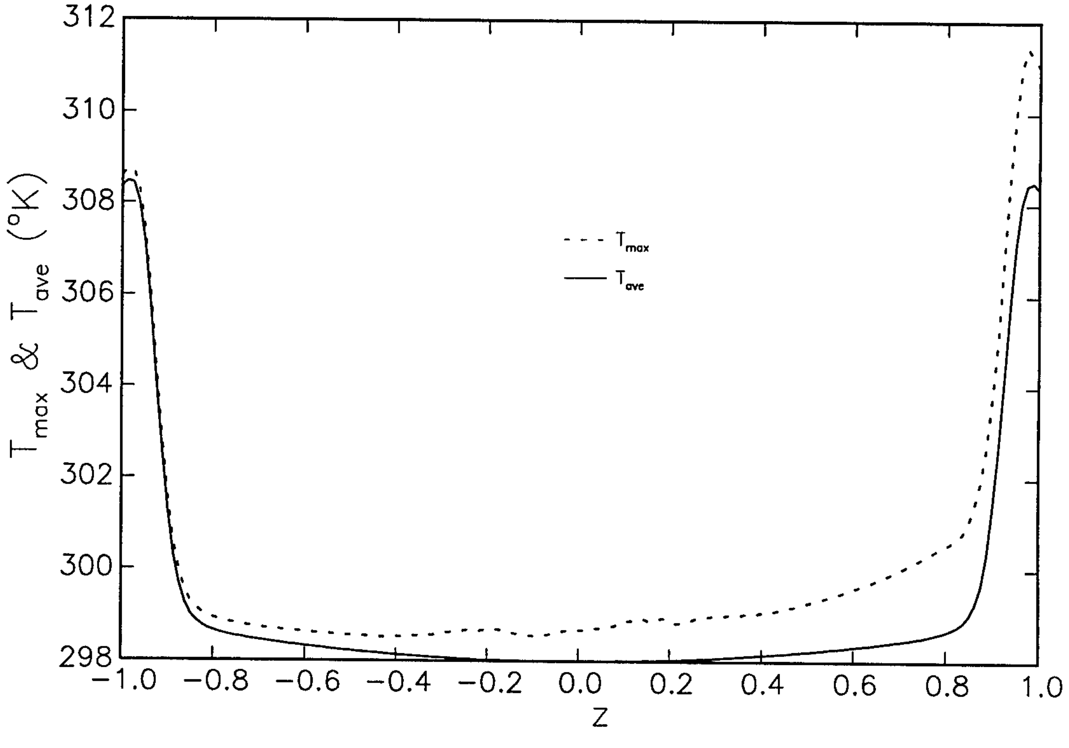

Figure 9.15: The comparison between the peak and average temperatures within the each x-y plane at time $t = 8.59\mu s$.

Appendix A

This appendix discusses the numerical simulation of the parabolized equations of motion for a constant property mixture. Section A1 summarizes teh governing equations in cylindrical (r, z) coordinates, while Section A.2 provides the same system after transformation (4.23) is applied. Numerical simulation of the unsteady (steady) equations is discussed in Section A.3(A.4).

A.1 Parabolized Approximation for a Constant Property Mixture

As mentioned in Section 4.3, the parabolized approximation of the equations of motion is based on ignoring the appropriate streamwise gradients. Implementation of the approximation reduces the system of governing equations to:

$$\frac{\partial \omega}{\partial t} + \frac{\partial}{\partial r}(\omega v_r) + \frac{\partial}{\partial z}(\omega v_z) = \frac{1}{R_e}(\frac{\partial^2 \omega}{\partial r^2} + \frac{\partial}{\partial r}(\frac{\omega}{r})) \qquad (A.1)$$

$$\frac{\partial}{\partial r}(\frac{1}{r}\frac{\Psi}{\partial r}) \approx -\omega \tag{A.2}$$

$$\frac{\partial T}{\partial t} + v_r\frac{\partial T}{\partial r} + v_z\frac{\partial T}{\partial z} = \frac{1}{R_eP_r}(\frac{\partial^2 T}{\partial r^2} + \frac{1}{r}\frac{\partial T}{\partial r} + \frac{E_c}{R_e}\Phi \tag{A.3}$$

where

$$\begin{cases} v_r = -\frac{1}{r}\frac{\partial\Psi}{\partial z} \\ v_z = \frac{1}{r}\frac{\partial\Psi}{\partial r} \end{cases} \tag{A.4}$$

$$\Phi \approx (\frac{\partial v_z}{\partial r})^2 \tag{A.5}$$

A.2 Stretched Coordinates

When the cylindrical coordinate system is stretched using the transformation Eq. (4.23), the governing system of equations given above becomes:

$$\frac{\partial\omega}{\partial t} + \xi_r\frac{\partial}{\partial\xi}(\omega v_\xi) + \frac{\partial}{\partial z}(\omega v_z) = \frac{1}{R_e}(\xi_r^2\frac{\partial^2\omega}{\partial\xi^2} + \xi_{rr}\frac{\partial\omega}{\partial\xi} + \frac{\xi_r}{r}\frac{\partial\omega}{\partial\xi} - \frac{\omega}{r^2}) \tag{A.6}$$

$$\xi_r^2\frac{\partial^2\Psi}{\partial\xi^2} + \xi_{rr}\frac{\partial\Psi}{\partial\xi} - \frac{\xi_r}{r}\frac{\partial\Psi}{\partial\xi} = -\omega r \tag{A.7}$$

$$\frac{\partial T}{\partial t} + v_\xi\xi_r\frac{\partial T}{\partial\xi} + v_z\frac{\partial T}{\partial z} = \frac{1}{R_eP_r}(\xi_r^2\frac{\partial^2 T}{\partial\xi^2} + \xi_{rr}\frac{\partial T}{\partial\xi} + \frac{\xi_r}{r}\frac{\partial T}{\partial\xi}) + \frac{E_c}{R_e}\Phi \tag{A.8}$$

where,

$$\begin{cases} v_\xi = -\frac{1}{r}\frac{\partial\Psi}{\partial z} \\ v_z = \frac{\xi_r}{r}\frac{\partial\Psi}{\partial\xi} \end{cases} \tag{A.9}$$

$$\Phi \approx \xi_r^2(\frac{\partial v_z}{\partial\xi})^2 \tag{A.10}$$

where, ξ_r and ξ_{rr} respectively denote $\partial\xi/\partial r$ and $\partial^2\xi/\partial r^2$.

A.3 Unsteady Simulation

As in Section 4.2, a finite-difference approach to the simulation of the above system of equations is adopted. Here, the non-linear convection terms are treated using a 3rd-order Adams-bashforth scheme, while a 2nd-order Crank-Nicolson scheme is applied to the remaining terms.

To simplify the presentation, we shall employ the following abbreviations:

$$\left\{\begin{array}{l} f_i \equiv \frac{\partial \xi}{\partial r}(\xi_i) \\ g_i \equiv \frac{\partial^2 \xi}{\partial r^2}(\xi_i) \\ r_i \equiv r(\xi_i) \end{array}\right. \tag{A.11}$$

in conjunction with standard finite-difference notation. With these definitions, time-stepping is summarized as follows:

1. The vorticity in the domain interior is updated by inverting, at every streamwise location, the discrete elliptic equations:

   $$H\omega_{i,j}^{n+3} = RW_{i,j}^{n+2} \tag{A.12}$$

   with Dirichlet boundary conditions:

   $$\left\{\begin{array}{l} \omega_{1,j}^{n+3} = 0 \\ \omega_{N_r,j}^{n+3} = -2f_{N_r}^2 \frac{\Psi_{N_r,j}^{n+3} - \Psi_{N_r-1,j}^{n+3}}{\Delta\xi^2} \end{array}\right. \tag{A.13}$$

   Here, H denotes the one-dimensional Helmholtz operator,

   $$\begin{aligned} H\omega_{i,j} &= [\frac{1}{2R_e}(\frac{g_i}{2\Delta\xi} + \frac{f_i}{2r_i\Delta\xi} - \frac{f_i^2}{\Delta\xi^2})]\omega_{i-1,j} \\ &+[\frac{1}{R_e}\frac{f_i^2}{2\Delta\xi} + \frac{1}{2R_e r_i^2} + \frac{1}{\Delta t}]\omega_{i,j} \\ &-[\frac{1}{2R_e}(\frac{f_i^2}{\Delta\xi^2} + \frac{g_i}{2\Delta\xi} + \frac{f_i}{2r_i\Delta\xi})]\omega_{i+1,j} \end{aligned} \tag{A.14}$$

RW the corresponding source term,

$$\begin{aligned} RW_{i,j}^{n+2} &= -\frac{\omega_{i,j}^{n+2}}{\Delta t} + \frac{1}{12}[23S_{i,j}^{n+2} - 16S_{i,j}^{n+1} + 5S_{i,j}^{n}] \\ & -\frac{1}{2R_e}[f_i^2\frac{\omega_{i+1,j}^{n+2} - 2\omega_{i,j}^{n+2} + \omega_{i-1,j}^{n+2}}{\Delta\xi^2} \\ & +(g_i + \frac{f_i}{r_i})\frac{\omega_{i+1,j}^{n+2} - \omega_{i-1,j}^{n+2}}{2\Delta\xi} - \frac{\omega_{i,j}}{r_i^2}] \end{aligned} \tag{A.15}$$

and,

$$S_{ij} = f_i\frac{(\omega v_\xi)_{i+1,j} - (\omega v_\xi)_{i-1,j}}{2\Delta\xi} + \frac{(\omega v_z)_{i+1,j} - (\omega v_z)_{i-1,j}}{2\Delta z} \tag{A.16}$$

the vorticity convection term.

2. The new streamfunction distribution is computed by inverting, at every streamwise section, the discrete "Laplacian" opeartors:

$$L\psi_{i,j}^{n+3} = r_i\omega_{i,j}^{n+3} \tag{A.17}$$

with the Dirichlet boundary conditions given in Eqs. (4.6) amd (4.7). Here,

$$\begin{aligned} L\psi_{ij} &\equiv (\frac{g_i}{2\Delta\xi} - \frac{\xi_r^2(i)}{\Delta\xi^2} - \frac{f_i}{2r_i\Delta\xi})\psi_{i-1,j} + \frac{2f_i^2}{\Delta\xi^2}\psi_{i,j} \\ & +(\frac{f_i}{2r_i\Delta\xi} - \frac{g_i}{2\Delta\xi} - \frac{2f_i^2}{\Delta\xi^2})\psi_{i-1,j} \end{aligned} \tag{A.18}$$

is the discrete Laplacian associated with Eq. (A-7).

3. Determine the solid surface vorticity values using:

$$\omega_{N_r,j}^{n+3} = -2f_{N_r}^2\frac{\psi_{N_r,j}^{n+3} - \psi_{N_r-1,}^{n+3}}{\Delta\xi^2} \tag{A.19}$$

4. Update the velocity field using:

$$\left\{ \begin{array}{l} (v_\xi)_{i,j} = \frac{\psi_{i,j-1}-\psi_{i,j+1}}{2r_i\Delta z} \\ (v_z)_{i,j} = f_i\frac{\psi_{i+1,j}-\psi_{i-1,j}}{2r_i\Delta\xi} \end{array} \right. \tag{A.20}$$

5. Advance the temperature distribution by inverting, at every streamwise location, the discrete elliptic equations:

$$GT_{i,j}^{n+3} = RT_{i,j}^{n+2} \tag{A.21}$$

subject to the Neumann conditions given in Eqs. (4.6-4.7). Here, G denotes the one-dimensional Helmholtz opearator,

$$\begin{aligned} GT_{i,j} \;=\; & [\frac{1}{2R_eP_r}(\frac{g_i}{2\Delta\xi} + \frac{f_i}{2r_i\Delta\xi} - \frac{f_i^2}{\Delta\xi^2})]T_{i-1,j} \\ & +[\frac{1}{R_eP_r}\frac{f_i^2}{\Delta\xi^2} + \frac{1}{\Delta t}]T_{i,j} \\ & -[\frac{1}{2R_eP_r}(\frac{f_i^2}{\Delta\xi^2} + \frac{g_i}{2\Delta\xi} + \frac{f_i}{2r_i\Delta\xi})]T_{i+1,j} \end{aligned} \tag{A.22}$$

RT the corresponding source term,

$$\begin{aligned} RW_{i,j}^{n+2} \;=\; & -\frac{T_{i,j}^{n+2}}{\Delta t} + \frac{1}{12}[23P_{i,j}^{n+2} - 16P_{i,j}^{n+1} + P_{i,j}^{n}] \\ - \;& \frac{1}{2R_eP_r}[f_i^2\frac{T_{i+1,j}^{n+2} - 2T_{i,j}^{n+2} + T_{i-1,j}^{n+2}}{\Delta\xi^2} \\ + \;& (g_i + \frac{f_i}{r_i})\frac{T_{i+1,j}^{n+2} - T_{i-1,j}^{n+2}}{2\Delta\xi}] + \frac{E_c}{2R_e}[\Phi_{i,j}^{n+3} + \Phi_{i,j}^{n+2}] \end{aligned} \tag{A.23}$$

and,

$$P_{ij} = (v_\xi)_{i,j}f_i\frac{\omega_{i+1,j} - \omega_{i-1,j}}{2\Delta\xi} + (v_z)_{i,j}\frac{\omega_{i,j+1} - \omega_{i,j-1}}{2\Delta z} \tag{A.24}$$

the thermal convection term. Note that the viscous dissipation function is approximated through:

$$\Phi_{i,j} = \begin{cases} f_i^2(\frac{(v_z)_{i+1,j}-(v_z)_{i-1,j}}{2\Delta\xi})^2 & 1 \leq i \leq N_r - 1 \\ f_i^2(\frac{4(v_z)_{i+1,j}-(v_z)_{i-2,j}}{2\Delta\xi})^2 & i = N_r \end{cases} \tag{A.25}$$

while the grid stretching derivatives f_i and g_i are evaluated numerically, respectively using:

$$f_i = \frac{2\Delta\xi}{r_{i+1} - r_{i-1}} \tag{A.26}$$

$$g_i = -(\frac{r_{i+1} - 2r_i + r_{i-1}}{\Delta\xi^2})/(\frac{r_{i+1} - r_{i-1}}{2\Delta\xi})^3 \tag{A.27}$$

A.4 Steady Code

When considering the steady parabolized equations of motion, the streamwise coordinate z may be regarded as a time variable and the solution is marched fro mthe inlet of nozzle towards the exit in small Δz increments. Simulation of the steady parabolized equations, which also employs the stretched grid technique discussed above, on the following finite-difference discretizations of the vorticity transport, streamfunction and energy equations:

$$\begin{cases} H\omega_i^{n+1} = \omega_i^n (v_z)_i^n \\ L\psi_i^{n+1} = \omega_i^{n+1} r_i \\ MT_i^{n+1} = (v_z)_i^{n+1} T_i^n + \frac{E_c}{R_e}\Delta z \psi_i^{n+1} \end{cases} \tag{A.28}$$

where

$$\begin{aligned} H\omega_i^{n+1} \quad \equiv \quad & [-f_i \frac{(v_\xi)_{i-1}^n}{2}\frac{\Delta z}{\Delta\xi} - \frac{\Delta z}{R_e}(\frac{f_i^2}{\Delta\xi^2} - \frac{g_i}{2\Delta\xi} - \frac{f_i}{2r_i\Delta\xi})]\omega_{i-1}^{n+1} \\ & +[(v_z)_i^n + \frac{\Delta z}{R_e}(\frac{2f_i^2}{\Delta\xi^2} + \frac{1}{r_i^2})]\omega_i^{n+1} \end{aligned}$$

$$+[f_i\frac{(v_\xi)^n_{i+1}}{2}\frac{\Delta z}{\Delta\xi}-\frac{\Delta z}{R_e}(\frac{f_i^2}{\Delta\xi^2}+\frac{g_i}{2\Delta\xi}+\frac{f_i}{2r_i\Delta\xi})]\omega^{n+1}_{i+1} \tag{A.29}$$

$$\begin{aligned} L\psi_i &\equiv [\frac{g_i}{2\Delta\xi}-\frac{f_i^2}{\Delta\xi^2}-\frac{f_i}{2r_i\Delta\xi}]\psi_{i-1}+\frac{2f_i^2}{\Delta\xi^2}\psi_i \\ &+[\frac{f_i}{2r_i\Delta\xi}-\frac{g_i}{2\Delta\xi}-\frac{f_i^2}{\Delta\xi^2}]\psi_{i+1} \end{aligned} \tag{A.30}$$

$$\begin{aligned} MT_i^{n+1} &\equiv [-f_i\frac{(v_\xi)^{n+1}_i}{2}\frac{\Delta z}{\Delta\xi}-\frac{\Delta z}{R_eP_r}(\frac{f_i^2}{\Delta\xi^2}-\frac{g_i}{2\Delta\xi}-\frac{f_i}{2r_i\Delta\xi})]T^{n+1}_{i-1} \\ &+ [(v_z)^{n+1}_i+\frac{\Delta z}{R_eP_r}\frac{2f_i^2}{\Delta\xi^2}]T^{n+1}_i \\ &+ [f_i\frac{(v_\xi)^{n+1}_i}{2}\frac{\Delta z}{\Delta\xi}-\frac{\Delta z}{R_eP_r}(\frac{f_i^2}{\Delta\xi^2}+\frac{g_i}{2\Delta\xi}+\frac{f_i}{2r_i\Delta\xi})]T^{n+1}_{i+1} \end{aligned} \tag{A.31}$$

and the notation $\omega_i^n = \omega(\xi_i, z_n) = \omega(i\Delta\xi, n\Delta z)$ is used. Meanwhile, the velocity components v_ξ and v_z appearing in Eqs. (A29-31) are respectively approximated using:

$$(v_\xi)^{n+1}_i = \frac{\psi_i^n-\psi_i^{n+1}}{r_i\Delta z} \tag{A.32}$$

$$(v_z)^{n+1}_i = f_i\frac{\psi^{n+1}_{i+1}-\psi^{n+1}_{i-1}}{2r_i\Delta\xi} \tag{A.33}$$

As in the unsteady case, solution marching requires the inversion of three elliptic operators for the vorticity, streamfunction and temperature. However, in the present steady case, implicit vorticity boundary conditions are implemented, so that the equation systems for vorticity and streamfunction are coupled at the boundary. In order to reduce the computational cost associated with simultaneous inversion of the two systems, a boundary Green's function technique is incorporated into the computations. This technique exploits the linearity of the elliptic operators by first solving the auxiliary systems:

$$\begin{cases} H\tilde{\omega}_i^{n+1} = \tilde{\omega}_i^n (v_z)_i^{n-1} \\ \tilde{\omega}_1^{n+1} = \tilde{\omega}_{N_r}^{n+1} = 0 \end{cases} \tag{A.34}$$

$$\begin{cases} L\tilde{\psi}_i^{n+1} = \tilde{\omega}_1^{n+1} r_i \\ \tilde{\psi}_1^{n+1} = 0 \\ \tilde{\psi}_{N_r}^{n+1} = \int_0^1 r u_z(r) dr \end{cases} \tag{A.35}$$

and then expressing the solution to the full system as:

$$\begin{cases} \omega_i^{n+1} = \tilde{\omega}_i^{n+1} + \epsilon\kappa_i \\ \psi_i^{n+1} = \tilde{\psi}_i^{n+1} + \epsilon\lambda_i \end{cases} \tag{A.36}$$

where κ_i and λ_i are the solutions to the elementary problems:

$$\begin{cases} H\kappa_i = 0 \\ \kappa_1 = 0 \\ \kappa_{N_r} = 1 \end{cases} \tag{A.37}$$

$$\begin{cases} L\lambda_i = \kappa_i r_i \\ \kappa_1 = \kappa_{N_r} = 0 \end{cases} \tag{A.38}$$

and ϵ is an arbitrary constant. Choosing ϵ so that vorticity boundary conditions are satisfied, we find:

$$\epsilon = \frac{\frac{2f_{N_r}^2}{\Delta\xi^2}(\tilde{\psi}_{N_r}^{n+1} - \tilde{\psi}_{N_r-1}^{n+1})}{1 + \frac{2f_{N_r}^2}{\Delta\xi^2}\lambda_{N_r-1}} \tag{A.39}$$

No such difficulty is encountered in the marching of the energy equation, since homogeneous Neumann boundary conditions are imposed both at $r = 0$ and $r = 1$.

Appendix B

This appendix discusses the numerical simulation if the parabolized equations of motion for an incompressible variable property mixture. Two models are used in the computations: the first model accommodates a temperature-dependent viscosity, but assume that a constant thermal conductivity. In the second model, both the viscosity and thermal conductivity are taken to be temperature dependent.

Since the former model may be regarded as a special case of the second, only the more general case is discussed. Section B1 summarizes the governing equations for the parabolized approximation in cylindrical (r, z) coordinates, while Section B2 provides the same system after transformation (4.23) is applied. Numerical simulation of the unsteady (steady) equations is discussed in Section B3 (B4).

B.1 Parabolized Approximation for a Variable Property Mixture

When the appropriate streamwise gradients are ignored, the governing equations given in Section 5 reduce to:

$$\frac{\partial\omega}{\partial t}+\frac{\partial}{\partial r}(\omega v_r)+\frac{\partial}{\partial z}(\omega v_z)=\frac{1}{Re}[\nu^*(\frac{\partial^2\omega}{\partial r^2}+\frac{\partial}{\partial r}(\frac{\omega}{r}))$$

$$+\frac{\partial\nu^*}{\partial r}(2\frac{\partial\omega}{\partial r}+\frac{\omega}{r})+\omega\frac{\partial^2\nu^*}{\partial r^2}] \qquad \text{(B.1)}$$

$$\frac{\partial}{\partial r}(\frac{1}{r}\frac{\psi}{\partial r})\approx-\omega \qquad \text{(B.2)}$$

$$\frac{\partial T}{\partial t}+v_r\frac{\partial T}{\partial r}+v_z\frac{\partial T}{\partial z}=\frac{1}{RePr}[\frac{1}{r}\frac{\partial}{\partial r}(k^*r\frac{\partial T}{\partial r})]+\frac{Ec}{Re}\nu^*\Phi \qquad \text{(B.3)}$$

where

$$\nu^*\equiv\frac{\tilde{\nu}(\tilde{T})}{\tilde{\nu}(\tilde{T}_o)} \qquad \text{(B.4)}$$

$$k^*\equiv\frac{\tilde{k}(\tilde{T})}{\tilde{k}(\tilde{T}_o)} \qquad \text{(B.5)}$$

$$\begin{cases} v_r=-\frac{1}{r}\frac{\partial\psi}{\partial z} \\ v_z=\frac{1}{r}\frac{\partial\psi}{\partial r}\end{cases} \qquad \text{(B.6)}$$

$$\Phi\approx(\frac{\partial v_z}{\partial r})^2 \qquad \text{(B.7)}$$

and the $\sim$ is used to denote a dimensional quantity.

B.2 Stretched Coordinates

When the cylindrical coordinate system is stretched using the transformation Eq. (4.23), the governing system of equations given above becomes:

$$\begin{aligned}\frac{\partial \omega}{\partial t} + \xi_r \frac{\partial}{\partial \xi}(\omega v_\xi) + \frac{\partial}{\partial z}(\omega v_z) = \frac{1}{Re}[\nu^*(\xi_r^2 \frac{\partial^2 \omega}{\partial \xi^2} \\ + \xi_{rr}\frac{\partial \omega}{\partial \xi} + \frac{\xi_r}{r}\frac{\partial \omega}{\partial \xi} - \frac{\omega}{r^2}) + \xi_r \frac{\partial \nu^*}{\partial \xi}(2\xi_r \frac{\partial \omega}{\partial \xi} + \frac{\omega}{r}) \\ + \omega(\xi_r^2 \frac{\partial^2 \nu^*}{\partial \xi^2} + \xi_{rr}\frac{\partial \nu^*}{\partial \xi})] \qquad \text{(B.8)}\end{aligned}$$

$$\xi_r^2 \frac{\partial^2 \psi}{\partial \xi^2} + \xi_{rr}\frac{\partial \psi}{\partial \xi} - \frac{\xi_r}{r}\frac{\partial \psi}{\partial \xi} = -\omega r \qquad \text{(B.9)}$$

$$\frac{\partial T}{\partial t} + v_\xi \xi_r \frac{\partial T}{\partial \xi} + v_z \frac{\partial T}{\partial z} = \frac{1}{RePr}[\frac{\xi_r}{r}\frac{\partial}{\partial \xi}(k^* r \xi_r \frac{\partial T}{\partial \xi})] + \frac{Ec}{Re}\nu^* \Phi \qquad \text{(B.10)}$$

where

$$\begin{cases} v_\xi = -\frac{1}{r}\frac{\partial \psi}{\partial z} \\ {}_z = \frac{\xi_r}{r}\frac{\partial \psi}{\partial \xi} \end{cases} \qquad \text{(B.11)}$$

$$\Phi \approx \xi_r^2 (\frac{\partial v_z}{\partial \xi})^2 \qquad \text{(B.12)}$$

while ξ_r and ξ_{rr} respectively denote $\partial \xi / \partial r$ and $\partial^2 \xi / \partial r^2$.

B.3 Unsteady Simulation

As in Appendix A, a finite-difference methodology is adopted in the simulation of the above system of equations. Here, teh non-linear convection terms are treated using a 3rd-order Adams-Bashforth scheme, while a 2nd-order Crank-Nicolson scheme is applied to the remaining terms. Using the same notation of Appendix A, time-stepping is summarized as follows:

1. The vorticity in the domain interior is updated by inverting, at every streamwise location, the discrete elliptic equations:

$$H\omega_{i,j}^{n+3} = RW_{i,j}^{n+2} \tag{B.13}$$

with Dirichlet boundary conditions:

$$\begin{cases} \omega_{1,j}^{n+3} = 0 \\ \omega_{N_r,j}^{n+3} = -2f_{N_r}^2 \frac{\Psi_{N_r,j}^{n+3} - \psi_{N_r-1,j}^{n+3}}{\Delta\xi^2} \end{cases} \tag{B.14}$$

Here, H denotes the one-dimensional Helmholtz operator,

$$\begin{aligned} H\omega_{i,j}^{n+3} &= [\frac{1}{2Re}((v^*)_{i,j}^{n+3}(\frac{g_i}{2\Delta\xi} + \frac{f_i}{2r_i\Delta\xi} - \frac{f_i^2}{\Delta\xi^2})) \\ &+ f_i^2\frac{(v^*)_{i+1,j}^{n+3} - (v^*)_{i-1,j}^{n+3}}{2\Delta\xi^2}]\omega_{i-1,j}^{n+3} + [\frac{1}{2Re}((v^*)_{i,j}^{n+3}(\frac{f_i^2}{\Delta\xi^2} \\ &+ \frac{1}{r_i^2}) - (\frac{f_i}{r_i} + g_i)\frac{(v^*)_{i+1,j}^{n+3} - (v^*)_{i-1,j}^{n+3}}{2\Delta\xi} \\ &- f_i^2\frac{(v^*)_{i+1,j}^{n+3} - 2(v^*)_{i,j}^{n+3} + (v^*)_{i-1,j}^{n+3}}{\Delta\xi^2}) \\ &+ \frac{1}{\Delta t}]\omega_{i,j}^{n+3} - [\frac{1}{2Re}((v^*)_{i,j}^{n+3}(\frac{g_i}{2\Delta\xi} + \frac{f_i}{2r_i\Delta\xi} + \frac{f_i^2}{\Delta\xi^2})) \\ &+ f_i^2\frac{(v^*)_{i+1,j}^{n+3} - (v^*)_{i-1,j}^{n+3}}{2\Delta\xi^2}]\omega_{i+1,j}^{n+3} \end{aligned} \tag{B.15}$$

RW the corresponding source term,

$$RW_{i,j}^{n+2} = -\frac{\omega_{i,j}^{n+2}}{\Delta t} + \frac{1}{12}[23S_{i,j}^{n+2} - 16S_{i,j}^{n+1} + 5S_{i,j}^{n}]$$

$$
\begin{aligned}
- & \frac{1}{2Re}\{(v^*)^{n+2}_{i,j}[f_i^2\frac{\omega^{n+2}_{i+1,j} - 2\omega^{n+2}_{i,j} + \omega^{n+2}_{i-1,j}}{\Delta\xi^2} \\
+ & (g_i + \frac{f_i}{r_i})\frac{\omega^{n+2}_{i+1,j} - \omega^{n+2}_{i-1,j}}{2\Delta\xi} - \frac{\omega^{n+2}_{i,j}}{r_i^2}] + (2f_i^2\frac{\omega^{n+2}_{i+1,j} - \omega^{n+2}_{i-1,j}}{2\Delta\xi}) \\
+ & \omega^{n+2}_{i,j}[f_i^2\frac{(v^*)^{n+2}_{i+1,j} - 2(v^*)^{n+2}_{i,j} + (v^*)^{n+2}_{i-1,j}}{\Delta\xi^2} \\
+ & g_i\frac{(v^*)^{n+2}_{i+1,j} - (v^*)^{n+2}_{i-1,j}}{2\Delta\xi}]\}
\end{aligned}
\tag{B.16}
$$

and,

$$
S_{ij} = f_i\frac{(\omega v_\xi)_{i+1,j} - (\omega v_\xi)_{i-1,j}}{2\Delta\xi} + \frac{(\omega v_z)_{i,j+1} - (\omega v_z)_{i,j-1}}{2\Delta z} \tag{B.17}
$$

the vorticity convection term.

Note that the viscosity values at time level $n+3$, which appear in the definition of the Helmholtz operator (B.15), are not generally known before the energy equation is solved. In order to avoid a nonlinear coupling between the vorticity transport and energy equations, the following approximation is used in the computations:

$$
(v^*)^{n+3}_{i,j} = 2(v^*)^{n+2}_{i,j} - (v^*)^{n+1}_{i,j} \tag{B.18}
$$

2. The new streamfunction distribution is computed by inverting, at every streamwise section, the discrete "Laplacian" operator:

$$
L\psi^{n+3}_{i,j} = r_i\omega^{n+3}_{i,j} \tag{B.19}
$$

with the Dirichlet boundary conditions given in Eqs. (4.6) and (4.7). Here,

$$\begin{aligned} L\omega_{ij} \equiv\ & (\frac{g_i}{2\Delta\xi} - \frac{\xi_r^2(i)}{\Delta\xi^2} - \frac{f_i}{2r_i\Delta\xi})\psi_{i-1,j} + \frac{2f_i^2}{\Delta\xi^2}\psi_{i,j} \\ + \ & (\frac{f_i}{2r_i\Delta\xi} - \frac{g_i}{2\Delta\xi} - \frac{2f_i^2}{\Delta\xi^2})\psi_{i-1,j} \end{aligned} \tag{B.20}$$

is the discrete Laplacian associated with Eq. (B.9).

3. Determine the solid surface vorticity values using:

$$\omega_{N_r,j}^{n+3} = -2f_{N_r}^2\frac{\psi_{N_r,j}^{n+3} - \psi_{N_r-1,j}^{n+3}}{\Delta\xi^2} \tag{B.21}$$

4. Update the velocity field using:

$$\begin{cases} (v_\xi)_{i,j} = \frac{\psi_{i,j-1} - psi_{i,j+1}}{2r_i\Delta z} \\ (v_z)_{i,j} = f_i\frac{\psi_{i+1,j} - \psi_{i-1,j}}{2r_i\Delta\xi} \end{cases} \tag{B.22}$$

5. Advance the temperature distribution by inverting, at every streamwise location, the discrete elliptic equations:

$$GT_{i,j}^{n+3} = RT_{i,j}^{n+2} \tag{B.23}$$

subject to the Neumann conditions given in Eqs. (4.6-4.7). Here, G denotes the one-dimensional Helmholtz operator,

$$\begin{aligned} GT_{i,j}^{n+3} = & [\frac{1}{2RePr}\frac{f_i}{r_i}\frac{(k^*)_{i,j}^{n+3}r_{i-1}f_{i-1}}{\Delta\xi^2}]T_{i-1,j}^{n+3} \\ & +[\frac{1}{2RePr}\frac{f_i}{r_i}\frac{(k^*)_{i,j}^{n+3}r_if_i + (k^*)_{i-1,j}^{n+3}r_{i-1}f_{i-1}}{\Delta\xi^2} \\ & +\frac{1}{\Delta t}]T_{i,j}^{n+3} - [\frac{1}{2RePr}\frac{f_i}{r_i}\frac{(k^*)_{i,j}^{n+3}r_if_i}{\Delta\xi^2}]T_{i+1,j}^{n+3} \end{aligned} \tag{B.24}$$

RT the corresponding source term,

$$\begin{aligned} RT_{i,j}^{n+2} &= -\frac{T_{i,j}^{n+2}}{\Delta t} + \frac{1}{12}[23P_{i,j}^{n+2} - 16P_{i,j}^{n+1} + P_{i,j}^{n}] \\ &- \frac{1}{2RePr}\frac{f_i}{r_i}(\frac{(k^*)_{i,j}^{n+2} r_i f_i (T_{i+1,j}^{n+2} - T_{i,j}^{n+2})}{\Delta\xi^2} \\ &- \frac{(k^*)_{i-1,j}^{n+2} r_{i-1} f_{i-1} (T_{i,j}^{n+2} - T_{i-1,j}^{n+2})}{\Delta\xi^2}) \\ &+ \frac{Ec}{2Re}[(\nu^*)_{i,j}^{n+3}\Phi_{i,j}^{n+3} + (\nu^*)_{i,j}^{n+2}\Phi_{i,j}^{n+2}] \end{aligned} \tag{B.25}$$

and,

$$P_{ij} = f_i(v_\xi)_{i,j}\frac{\omega_{i+1,j} - \omega_{i-1,j}}{2\Delta\xi} + (v_z)_{i,j}\frac{\omega_{i,j+1} - \omega_{i,j-1}}{2\Delta z} \tag{B.26}$$

the thermal convection term.

Note that the viscosity and thermal conductivity values at time level $n+3$, which appear in the definition of the Helmholtz opeator (B.24) and the cource term (B.25), are not known before the new temperature distribution is determined. In order to avoid nonlinear iterations, the following approximations is used in the computations:

$$(\nu^*)_{i,j}^{n+3} = (\nu^*)_{i,j}^{n+2} - (\nu^*)_{i,j}^{n+1} \tag{B.27}$$

$$(k^*)_{i,j}^{n+3} = 2(k^*)_{i,j}^{n+2} - (k^*)_{i,j}^{n+1} \tag{B.28}$$

As in Appendix A, the viscous dissipation function is approximated through:

$$\Phi_{i,j} = \begin{cases} f_i^2(\frac{(v_z)_{i+1,j} - (v_z)_{i-1,j}}{2\Delta\xi})^2 & 1 \le i \le N_r - 1 \\ f_i^2(\frac{4(v_z)_{i-1,j} - (v_z)_{i-2,j}}{2\Delta\xi})^2 & i = N_r \end{cases} \tag{B.29}$$

while the grid stretching derivatives f_i and g_i are evaluated numerically, respectively using:

$$f_i = \frac{2\Delta\xi}{r_{i+1} - r_{i-1}} \tag{B.30}$$

$$g_i = \frac{(r_{i+1} - 2r_i + r_{i-1})/\Delta\xi^2}{[(r_{i+1} - r_{i-1})/2\Delta\xi]^3} \tag{B.31}$$

B.4 Steady Code

Simulation of the steady parabolized equations of motion follows a similar approach to that used for constant property flow. Specifically, the simulation is based on the following stretched grid finite difference approximations of the vorticity transport, streamfunction and energy equations:

$$\left\{ \begin{array}{l} H\omega_i^{n+1} = \omega_i^n (v_z)_i^{n-1} \\ L\psi_i^{n+1} = \omega_i^{n+1} r_i \\ MT_i^{n+1} = (v_z)_i^{n+1} T_i^n + \frac{Ec}{Re}\Delta z (\nu^*)_i^{n+1} \Phi_i^{n+1} \end{array} \right. \tag{B.32}$$

where

$$\begin{aligned} H\omega_i^{n+1} &= [-f_i \frac{(v_\xi)_{i-1}^n}{2} \frac{\Delta z}{\Delta\xi} - \frac{\Delta z}{Re}((\nu^*)_i^{n+1}(\frac{f_i^2}{\Delta\xi^2} - \frac{g_i}{2\Delta\xi} - \frac{f_i}{2r_i\Delta\xi}) \\ &- 2f_i^2 \frac{(\nu^*)_{i+1}^{n+1} - (\nu^*)_{i-1}^{n+1}}{4\Delta\xi^2})]\omega_{i-1}^{n+1} + [(v_z)_i^n + \frac{\Delta z}{Re}(\frac{2(\nu^*)_i^{n+1} f_i^2}{\Delta\xi^2} \\ &+ \frac{(\nu^*)_i^{n+1}}{r_i^2} - f_i \frac{(\nu^*)_{i+1}^{n+1} - (\nu^*)_{i-1}^{n+1}}{2r_i\Delta\xi} - g_i \frac{(\nu^*)_{i+1}^{n+1} - (\nu^*)_{i-1}^{n+1}}{2\Delta\xi} \\ &- f_i^2 \frac{(\nu^*)_{i+1}^{n+1} - 2(\nu^*)_i^{n+1} + (\nu^*)_{i-1}^{n+1}}{\Delta\xi^2})]\omega_i^{n+1} + [f_i \frac{(v_\xi)_{i+1}^n}{2} \frac{\Delta z}{\Delta\xi} \end{aligned}$$

$$\begin{aligned}
&- \frac{\Delta z}{Re}((\nu^*)_i^{n+1}(\frac{f_i^2}{\Delta\xi^2} + \frac{g_i}{2\Delta\xi} + \frac{f_i}{2r_i\Delta\xi}) \\
&+ 2f_i^2\frac{(\nu^*)_{i+1}^{n+1} - (\nu^*)_{i-1}^{n+1}}{4\Delta\xi^2})]\omega_{i+1}^{n+1} \qquad \text{(B.33)} \\
L\psi_i &= (\frac{g_i}{2\Delta\xi} - \frac{f_i^2}{\Delta\xi^2} - \frac{f_i}{2r_i\Delta\xi})\psi_{i-1} + \frac{2f_i^2}{\Delta\xi^2}\psi_i \\
&+ (\frac{f_i}{2r_i\Delta\xi} - \frac{g_i}{2\Delta\xi} - \frac{f_i^2}{\Delta\xi^2})\psi_{i+1} \qquad \text{(B.34)} \\
MT_i^{n+1} &= [-f_i\frac{(v_\xi)_i^{n+1}}{2}\frac{\Delta z}{Re} - \frac{\Delta z}{RePr}\frac{f_i}{r_i}\frac{(k^*)_{i-1}^{n+1}r_{i-1}f_{i-1}}{\Delta\xi^2}]T_{i-1}^{n+1} \\
&+ [(v_z)_i^{n+1} + \frac{\Delta z}{RePr}\frac{f_i}{r_i}\frac{(k^*)_i^{n+1}r_if_i + (k^*)_{i-1}^{n+1}r_{i-1}f_{i-1}}{\Delta\xi^2}]T_i^{n+1} \\
&+ [f_i\frac{(v_\xi)_i^{n+1}}{2}\frac{\Delta z}{Re} - \frac{\Delta z}{RePr}\frac{f_i^2(k^*)_i^{n+1}}{\Delta\xi^2}]T_{i+1}^{n+1} \qquad \text{(B.35)}
\end{aligned}$$

and the notation $\omega_i^n = \omega(\xi_i, z_n) = \omega(i\Delta\xi, n\Delta z)$ is used. The velocity components v_ξ and v_z appearing in Eqs. (B.33-35) are respectively calculated using:

$$(v_\xi)_i^{n+1} = \frac{\psi_i^n - \psi_i^{n+1}}{r_i\Delta z} \qquad \text{(B.36)}$$

$$(v_z)_i^{n+1} = \frac{\psi_{i+1}^{n+1} - \psi_{i-1}^{n+1}}{2r_i\Delta\xi} \qquad \text{(B.37)}$$

while the unknown values $(\nu^*)^{n+1}$ and $(k^*)^{n+1}$ appearing in the definitions (B.33) and (B.35) are respectively approximated through:

$$(\nu^*)_i^{n+1} = 2(\nu^*)_i^n - (\nu^*)_i^{n-1} \qquad \text{(B.38)}$$

$$(k^*)_i^{n+1} = 2(k^*)_i^n - (k^*)_i^{n-1} \qquad \text{(B.39)}$$

The numerical solution of Eqs. (B.33-35) uses the same LU-decomposition in conjunction with Boundary Green's function technique summarized in Appendix A4.

Bibliography

[1] ARPACI, V. *Conduction Heat transfer* (Addison-Wiley; MA, 1966).

[2] AVALLONE, E.A. & BAUMEISTER, T. *Mark's Standard Handbook for Mechanical Engineers*, 8th Edition (McGraw-Hill, NY; 1978).

[3] BATCHELOR, G. K. *Introduction to Fluid Dynamics* (Cambridge University Press; Cambridge, 1967).

[4] BOURNE, N.K. & FIELD, J.E. Bubble collapse and the initiation of explosion. *Proc. R. Soc. London,* **A435** 423-435, 1991.

[5] BATCHELOR, G. K. *The Theory of Homogeneous Turbulence.* Cambridge University Press; Cambridge, 1959.

[6] BURMEISTER, L.C. *Convective Heat Transfer* (Wiley; New York, 1993).

[7] CANUTO, C., HUSSANI, M. Y., QUARTERONI, A., & ZANG, T. A. *Spectral Methods in Fluid Dynamics.* Springer-Verlag, 1988.

[8] CARSLAW, H.S. & JAEGER, J.C. *Conduction of Heat in Solids* (Oxford University Press; Oxford, 1959).

[9] CEBECI, T. & BRADSHAW, P. *Physical and Computational Aspects of Convective Heat Transfer.* Springer-Verlag, 1984.

[10] DAUBE, O. Resolution of the 2D Navier-Stokesequations in velocity-vorticity Form by means of an influence matrix technique. *J. Comput. Phys.* **103**, 402, (1992).

[11] ECKELMANN, H. The structrues of the viscous sublayer and the adjacent wall region in a turbulent channel flow. *J. Fluid Mech.* **65**, 439, (1974).

[12] FIELD, J. E. Hot spot ignition mechanisms for explosives. *Accnts. Chem. Res.* **25** 489-496, 1992.

[13] FLECTCH, C. A. J. *Computational Techniques for Fluid Dynamics* (Springer-Verlag; NewYork, 1988).

[14] FREEDMAN, E. "A Skeleton Outline of the Physical Chemistry of HAN-Based Liquid Properties", ARL Document (1986).

[15] FUNG, J. C. H., HUNT, J. C. R., MALIK, N. A., & PERKINS, R. J. Kinematic simulation of homogeneous turbulence by unsteady random Fourier modes. *J. Fluid Mech.* **236**, 281, (1992).

[16] GRESHO, P.M. Incompressible fluid dynamics: Some fundamental formulation issues. *Ann. Rev. Fluid Mech.* **23**, 413-453, 1991.

[17] GUEVREMONT, G., HABASHI, W. G., & HAFEZ, M. M. *Int. J. Num. Methods* **10**, 461 (1990).

[18] Hirsch, C. *Numerical Computation of Internal and External Flows* (Wiely; New York, 1990).

[19] Incropera, F. C. & DeWitt, D. P. *Fundamentals of Heat and Mass Transfer* (Wiley; New York, 1990).

[20] Kays, W. M. & Crawford, M. E. *Convective Heat and Mass Transfer.* McGraw-Hill; 1980.

[21] Katz, J., Shi, X., & O. M. Knio Numerical study of shear-induced heating in high-speed nozzle flow if liquid monopropellant. *31th JANNAF Combustion Subcommittee Meeting,* Chemical Propulsion Information Agency, Nov., 1994.

[22] Kim, J., Moin, P., & Moser, R. Turbulence statisticas in fully developed flow at low Reynolds number. *J. Fluid Mech.* **177**, 133, (1985).

[23] Kleiser, L., & Zang, T. A. Numerical simulation of transition in wall-boundedshear flows. *Annu. Rev. Fluid Mech.* **23**, 495, (1991).

[24] Knapton, J. D., Messina, N. A. & Tarczynski, M. Some unsolved problems on ignition mechanisms in hydroxylammonium nitrate based liquid propellants. In *29th JANNAF combustion Subcommittee Meeting,* Chemical Propulsion Information Agency, October 1992.

[25] Liu, S., Meneveau, C., & Katz, J. On the properties of simularity subgrid-scale modelsas deduced from measurements in a turbulent jet. *J. Fluid Mech.* **275**, 83, (1994).

[26] McQuaid, M. *Private Communication* (1994).

[27] Meneveau, C., Lund, T. S., & Cabot, W. H. A Lagrangian dynamics subgrid-scale model of turbulence. *J. Fluid Mech.* (in process).

[28] Nigmatulin, R.I. & Khabeev, N.S. Heat exchange between a gas bubble and a liquid, 1974.

[29] Panton, R. *Incompressible Flow* (Wiley; New York, 1984).

[30] Rai, M. M. & Moin, P. Direct simulations of turbulent flow using finite difference schemes. *J. Comput. Phys.* **96**, 15, (1991).

[31] Schlichting, H. *Boundary Layer Theory* (McGraw-Hill; New York, 1979).

[32] Smith, C. R. & Metzler, S. P. The characteristics of low-speed streaks in the near-wall region of a turbulent boundary layer. *J. Fluid Mech.* **129**, 27, (1983).

[33] Tennekes, H. & Lumley, J. L. *A First Course in Turbulence*, MIT press, 1990.

[34] Thomas, T. G., & Williams, J. J. R. Turbulent simulation of open channel flow at low Reynolds number. *Int. J. Heat Mass Transfer.* **38**, 259, (1995).

[35] Tritton, D. J. *Physical Fluid Dynamics*, Oxford, 1987.

[36] VINCENT, A. & MENEGUZZI, M. The spatial structrue and statistical-properties of homogeneous turbulence. *J. Fluid Mech.* **225**, 1, (1991).

[37] ZANG, T. A., GILBERT, N., & KLEISER, L. Direct numerical simulation of the transitional zone. In *Instability and Transition*, pp.283-299, Springer-Verlag, New York.